

UNIVERSITÁ DEGLI STUDI DI BOLOGNA
Alma Mater Studiorum

FACOLTÁ DI SCIENZE MATEMATICHE FISICHE E NATURALI
Dottorato di ricerca in Fisica
XX Ciclo

**Measurement of the charm
production cross section
in DIS events at HERA**

Candidato:

Marcello Bindi

Advisor:

Prof. Maurizio Basile

Coordinatore:

Prof. Fabio Ortolani

Settore scientifico-disciplinare

FIS/04

Fisica Nucleare e Subnucleare

Contents

Introduction	v
1 Deep inelastic scattering and heavy quark production	1
1.1 Kinematics of Deep Inelastic Scattering	1
1.2 Neutral Current DIS cross section	6
1.3 Heavy quark production in DIS	11
1.3.1 BGF cross sections	12
1.3.2 The NLO program HVQDIS	13
1.4 Measurements of heavy quark production in ep collisions . . .	14
1.4.1 Inclusive $D^{*\pm}$ cross sections at ZEUS	15
1.4.2 Charm cross section from other mesons in DIS	19
1.4.3 Charm cross section using Impact Parameter	21
1.4.4 Beauty production in DIS at HERA	26
2 HERA and the ZEUS detector	31
2.1 The HERA collider	31
2.1.1 The HERA injection system	34
2.2 The HERA luminosity	36
2.3 The ZEUS detector	37
2.4 The Central Tracking Detector (CTD)	42
2.5 The ZEUS Microvertex Detector (MVD)	45
2.5.1 Barrel and forward micro vertex detector	46
2.6 The Uranium-scintillator Calorimeter (UCAL)	49

2.7	The muon detectors	51
2.7.1	The Forward MUON detector (FMUON)	51
2.7.2	The Barrel and Rear MUON detector (B/RMUON)	54
2.7.3	The Backing Calorimeter (BAC)	55
2.8	The luminosity measurement	56
2.9	Background	58
2.10	The ZEUS trigger system	59
3	Events reconstruction	63
3.1	Reconstructon of the kinematic variables	64
3.1.1	Electron Method	64
3.1.2	Jacquet-Blondel method	67
3.1.3	Double angle method	67
3.1.4	The \sum method	69
3.2	Electron identification and reconstruction	72
3.2.1	Electron identification	72
3.2.2	Reconstruction of the electron scattering angle	76
3.3	Reconstruction of the hadronic system	77
3.3.1	Reconstruction of the hadronic system using Energy Flow Objects(ZUFOS)	78
3.3.2	Energy correction to ZUFOS	81
3.3.3	ZUFOS associated to muons	82
3.4	Tracks and vertices reconstruction	84
3.4.1	MVD information	85
3.4.2	Beam spot and MVD alignment	86
3.5	Jet reconstruction	90
3.5.1	The longitudinally invariant k_T clustering algorithm	92
3.5.2	Recombination schemes	93
3.6	Muon reconstruction	93
3.6.1	The BREMAT package	94
3.6.2	MPMATCH	96

4	Event selection	99
4.1	Data and MC samples	99
4.1.1	DATA	99
4.1.2	Monte Carlo	100
4.2	Pre-selection	101
4.3	DIS selection	102
4.3.1	Data selection at trigger level	102
4.3.2	Kinematics cuts	102
4.4	Background sources	106
4.4.1	Heavy Vector Meson Decays	106
4.4.2	Cosmic Muons	106
4.4.3	Background from mis-identified hadrons	107
4.5	Muon selection	108
4.5.1	Anti-isolation cut	111
4.6	Jet Selection	112
4.7	Final selection and control plots.	113
4.7.1	DIS selection	113
4.7.2	Muon selection	114
4.7.3	Jet-Muon association	115
4.7.4	Additional cuts	115
4.7.5	Control plots	115
4.8	Discriminating observables	124
4.8.1	P_T^{rel}	124
4.8.2	Impact parameter	129
4.8.3	The " $p_T^{\nu \mu}$ " method	136
5	Charm and beauty cross sections	139
6.1	Definition of cross section	139
6.2	Measured cross section	140
6.3	Fraction determination	140

6.4	Acceptances	143
6.5	Fake muon contribution	143
6.6	Cross section corrections	145
6.6.1	Muon efficiency corrections	145
6.6.2	Tracking efficiency corrections	145
6.6.3	F_T^{rel} corrections	146
6.7	Charm and beauty differential cross sections	147
6.8	Systematic uncertainties	150
6.9	Discussion of results	153
	Conclusions	157
	Bibliography	158

Introduction

The measurement of heavy quark production is an important test of perturbative quantum chromodynamics (QCD). Heavy quark production in deep inelastic (i.e. at high virtualities of the exchanged photon) electron-proton scattering is calculable in QCD and provides information on the gluonic content of the proton which is complementary to that obtained from other measurements (as from the measurements of the scaling violation of the proton structure function). In addition, the scale of the hard scattering provided by the exchanged photon virtuality, Q^2 , may be large relative to the mass of the heavy quark, thus allowing allowing to study whether and when the heavy quark mass can be neglected.

In the last years the studies of charm quark production were based mainly on the reconstruction of charmed hadrons. The D^{*+} meson decay chain $D^{*+} \rightarrow D^0 \pi^+ \rightarrow k^- + \pi^+ + \pi^+ (+c.c.)$ was the decay channel providing the most precise measurements. However, the net probability for a c quark to fragment into a D^{*+} which undergoes in the above decay chain is only 0.6% while the probability for a c quark to decay semileptonically is 10% per lepton, making the measurement of c production from s.l. decays a competitive channel.

The purpose of this dissertation is to present the measurement of c-quark production in deep inelastic electron-proton collision at HERA, from s.l. decays into muons. The corresponding reaction is

$$e p \rightarrow e c \bar{c} X \tag{1}$$

where at least one of the c -quark decays semipetotonically into a muon. The measurement is performed in a phase space region where the virtuality Q^2 of the photon exchanged is greater than 20GeV^2 . The measurement is based on the data collected by ZEUS experiment during 2005, corresponding to an integrated luminosity of 125.055pb^{-1} . Single differential cross sections have been measured as a function of the main kinematic variables and of the transverse momentum and pseudorapidity of the muon. This is the first measurement of this kind performed at ZEUS experiment.

To achieve this result some discriminating variables have been used to distinguish the background due to the light flavours from the c and b quarks. The experimental results are compared to the next-to-leading order QCD predictions and Monte Carlo programmes.

This dissertation is organized as follows.

In **Chapter 1** we give an introduction to the theory of heavy quark production in deep inelastic electron-proton (ep) collisions. The main steps of the calculation are shown at the lowest order of perturbative QCD. At the end of the chapter we present the recent measurements of charm and beauty quarks performed at HERA.

In **Chapter 2** the HERA collider and the ZEUS detector are presented. The detector components used in our analysis and the trigger system are described in details.

Chapter 3 covers the event reconstruction. The cross section measurement is based on the selection of events containing three ingredients: a scattered positron detected in the calorimeter, a hard jet of particles and a muon detected in the muon chambers close to the jet. In addition we describe the different methods used to reconstruct the event kinematics. **Chapter 4** is dedicated to the description of the event selection. Cuts are applied to select

a sample of events from inclusive deep inelastic scattering. Further selection cuts are applied on the reconstructed muon and jet. The motivation of the selection cuts are discussed in detail. In addition, the kinematic distributions of the final event sample are compared to the prediction of Monte Carlo programs. Once the final sample of events is selected we present the reconstruction of the discriminating observables used in the analysis.

In **Chapter 5** we calculate the fraction of events corresponding to decays of charm and beauty quarks and distinguish them from other particle decays appearing in the sample. The procedure used to extract this fraction is described in detail, starting from basic 1-dimensional fits to arrive to the complex final fit used in the analysis.

In **Chapter 6** we explain the way to calculate the corresponding cross section using the extracted fractions. We conclude the chapter presenting the results of the differential cross section measurements and describing the related uncertainties. The experimental results are compared to the NLO QCD predictions and to Monte Carlo programs.

Chapter 1

Deep inelastic scattering and heavy quark production

In this chapter a short description of the kinematic variables describing the NC DIS interactions is given. The proton structure functions for NC ep scattering together with proton parton densities will be presented. Later the heavy quark contribution to the proton structure functions will be described giving some details. The chapter ends with a review of the recent measurements of charm quark production in ep collisions.

1.1 Kinematics of Deep Inelastic Scattering

In the Standard Model the interaction between a lepton and a hadron is realized by the exchange of a vector boson. The boson exchanged can be a photon (γ) or a Z^0 for neutral current processes (Figure 1.1-a); otherwise we have a charged current event with an exchange of a charged boson W^{+-} with a neutrino in the final state (Figure 1.1-b).

Let k, k' and P be the four-momentum of the incoming electron, the scattered electron and proton respectively. The four-momenta q of the exchanged boson between the electron and the proton is given by:

$$q = k - k'. \tag{1.1}$$

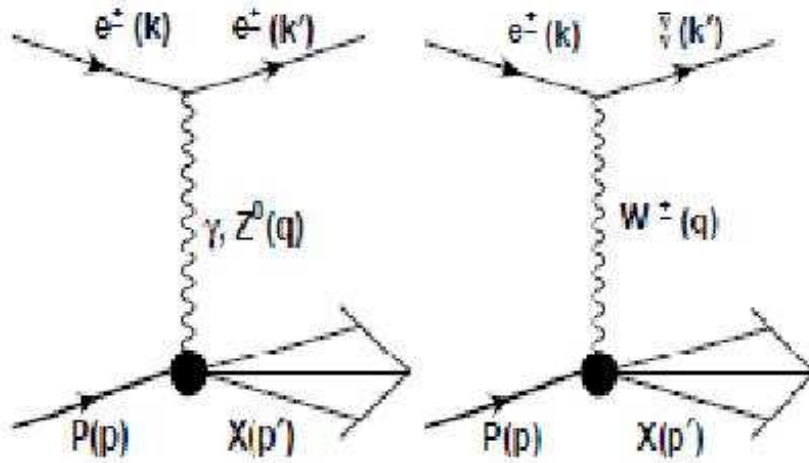


Figure 1.1: Diagrams of electron proton scattering. In a neutral current process a photon or a Z^0 is exchanged(a). In a charged current process the exchanged boson is a charged W^{+-} .

The scattering process is characterized by the following Lorentz scalars:

- the negative square of the four-momentum transfer, Q^2 , called *intermediate boson virtuality*,

$$Q^2 = -q^2 = -(k - k')^2; \quad (1.2)$$

- the square of the total center of mass energy, s ,

$$s = (k + P)^2 \simeq 2k \cdot P; \quad (1.3)$$

- the electron energy fraction transferred to the boson in the proton rest frame, y , called *inelasticity*,

$$y = \frac{P \cdot q}{P \cdot k}; \quad (1.4)$$

- the Bjorken scaling variable, that represents, in the proton infinite momentum frame, the fraction of the proton momentum carried by the parton (quark or gluon) involved in the interaction, x ,

$$x = \frac{Q^2}{2P \cdot q} \quad (1.5)$$

- the center-of-mass energy W of the $\gamma(Z^0, W^\pm) - p$ system:

$$W^2 = (q + P)^2 \simeq sy - Q^2 \quad (1.6)$$

However, the above kinematic variables are not independent; for example, neglecting the masses of the electron and proton, three of them are related to each other by:

$$Q^2 = sxy \quad (1.7)$$

At a given center of mass energy \sqrt{s} the kinematics of inclusive DIS scattering is completely described by two of the Lorenz-invariant quantities defined above. Usually the x, Q^2 or the y, Q^2 couple is chosen.

These couples can be experimentally determined by measuring the energy and the angle of the outgoing lepton. In Figure 1.2 we can see the (x, Q^2) coverage at HERA.

The virtuality Q^2 gives the scale of the interaction: the wavelength λ of the photon gives the smallest distance scale the probe can resolve:

$$\lambda = \frac{h}{|q|} \quad (1.8)$$

The Q^2 range at HERA up to about $40000 GeV^2$ is equivalent to a resolution of 1/1000 of the proton radius, i.e. 10^{-18} m. The kinematic variables described above, have a limited range of allowed values:

$$\begin{aligned} 0 < Q^2 < s \\ 0 < x < 1 \\ 0 < y < 1 \\ m_p < W < \sqrt{s} \end{aligned}$$

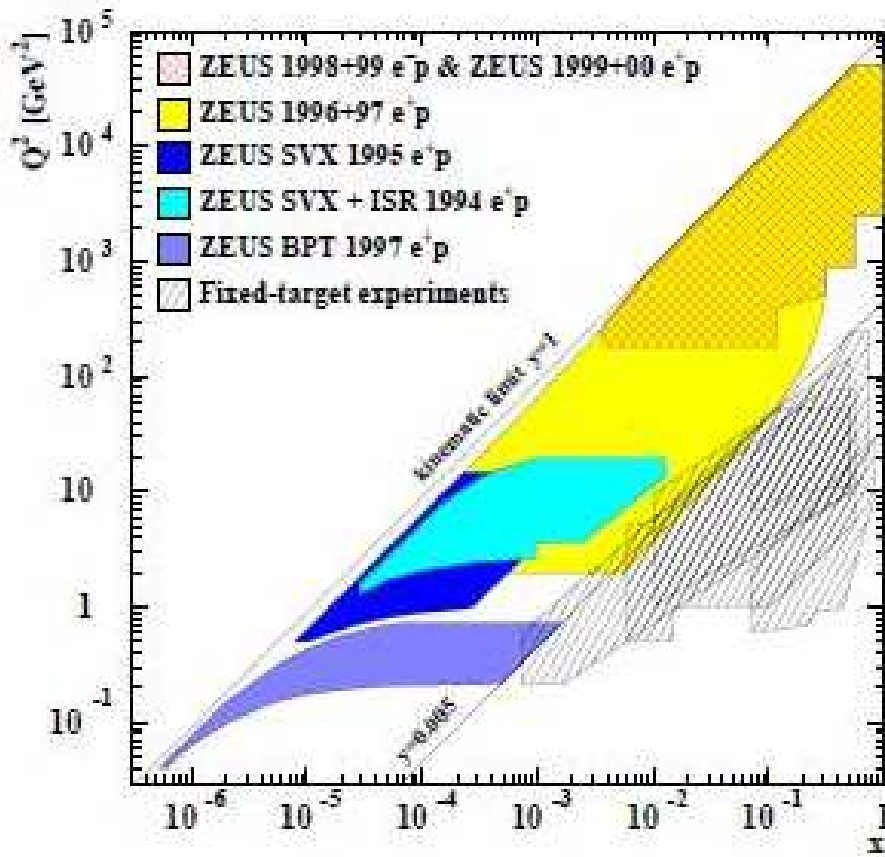


Figure 1.2: (x, Q^2) plane covered by HERA is compared with fixed target experiments. The coverage of x and Q^2 is extended by about two orders of magnitude

At low Q^2 the photon exchange dominates over the weak bosons, since the cross section falls rapidly as Q^{-4} (the photon propagator is given by $-ig_{\mu\nu}/q^2$). Only when Q^2 is sufficiently large the contributions from the Z^0 and the W^\pm are significant.

Indeed, when $Q^2 \geq M_{Z,W}^2$ (where $M_{Z^0} = 91.2 \text{ GeV}$ and $M_{W^\pm} = 80.2 \text{ GeV}$) the neutral and charged current cross-section are found to be of comparable size. This feature can be seen in figure 1.3. The converging of the two cross sections is an illustration of the electroweak unification theory.

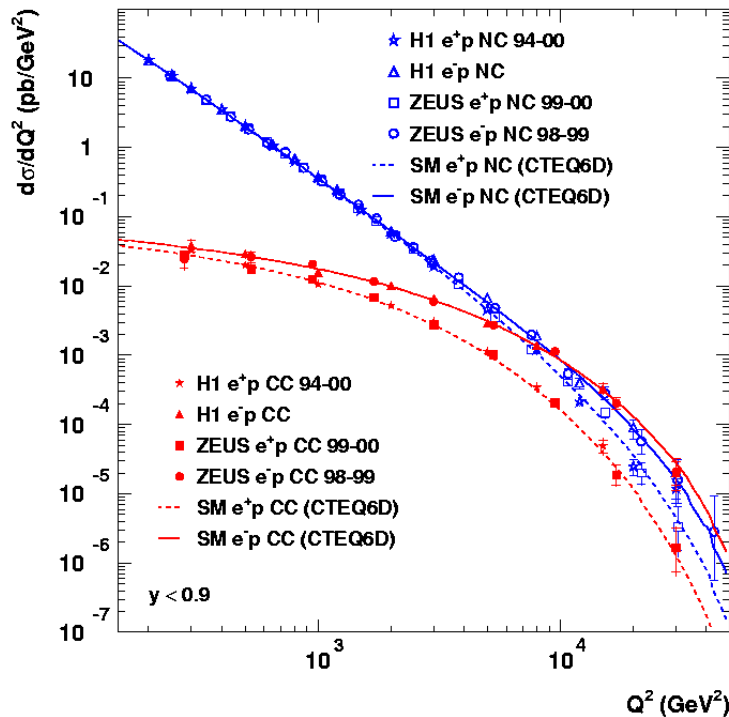


Figure 1.3: Neutral Current (blue) and Charged Current (red) cross sections as a function of Q^2

For large Q^2 , the scale is provided by this variable and allows perturbative calculations to be performed. For $Q^2 \gg 1 \text{ GeV}^2$, the events are referred to as *Deep Inelastic Scattering* (DIS); in this case the incoming lepton is significantly deflected. Experimentally we can define DIS events if the scattered electron is found in the detector.

For $Q^2 \ll 1 \text{ GeV}^2$, an almost real photon is exchanged and the process is referred to as *Photoproduction*: in this case the electron–proton interacting process can be seen as a collision of a real photon and a proton ($\gamma - p$). It is obvious that here Q^2 is not a hard scale, however the transverse momentum of jets may define a scale in the event. This hard scale allows the possibility of comparing experimental results with perturbative QCD calculations. We will not deal with this in detail since we want to concentrate on DIS physics.

Now we will go directly to the description of the partonic processes which are involved in this kind of events.

1.2 Neutral Current DIS cross section

We now concentrate on the case in which the electron–proton scattering is realized through the exchange of a photon. The words deep and inelastic refer to the conditions $Q^2 \gg M_P^2$ and $W^2 \gg M_P^2$, respectively, where M_P is the mass of the proton. These conditions ensure that perturbative QCD is applicable for the cross section calculation and that we are above the region of nucleon resonance production. In fact, for low values of Q^2 one expects just to excite the proton into a Δ – state, e.g. as in the reaction $ep \rightarrow e\Delta^+ \rightarrow ep\pi_0$. In these processes, the invariant mass of the photon–proton system is $W^2 \simeq M_P^2$. In a deep inelastic scattering (DIS) process the double differential cross section for the reaction $ep \rightarrow eX$ is given by

$$\frac{d\sigma}{dx dQ^2} = \frac{1}{k \cdot P} \frac{\pi\alpha^2}{Q^4} L_{\mu\nu} W^{\mu\nu} \quad (1.9)$$

where $\alpha = e^2/4\pi\hbar c \sim 1/137$ is the electromagnetic coupling constant and $L_{\mu\nu}$ and $W^{\mu\nu}$ are the leptonic and hadronic tensors respectively.

Substituting the expressions of the leptonic and hadronic tensors in Eq. 1.9 we obtain the relation [1]

$$\frac{d^2\sigma^{e^\pm p, NC}}{dx dQ^2} = \frac{4\pi\alpha^2}{xQ^4} \left[\frac{y^2}{2} 2xF_1(x, Q^2) + (1-y)F_2(x, Q^2) \mp \left(y - \frac{y^2}{2}\right)x F_3 \right]. \quad (1.10)$$

In the latter, $F_{1,2,3}$ are arbitrary functions of the kinematic variables x and Q^2 describing the $\gamma p \rightarrow X$ vertex. These functions, called *structure functions*, have to be obtained from the experiment and parameterize the structure of the proton. The structure function F_1 is proportional to the transverse component of the cross section, whereas the relation $F_L = F_2 - 2xF_1$, gives the longitudinal part of the cross section. Rewriting Eq. 1.10 yields:

$$\frac{d^2\sigma^{e^\pm p, NC}}{dx dQ^2} = \frac{2\pi\alpha_{em}^2}{xQ^4} \left[(1+(1-y)^2)F_2(x, Q^2) \mp (1-(1-y)^2)x F_3 - y^2 F_L \right]. \quad (1.11)$$

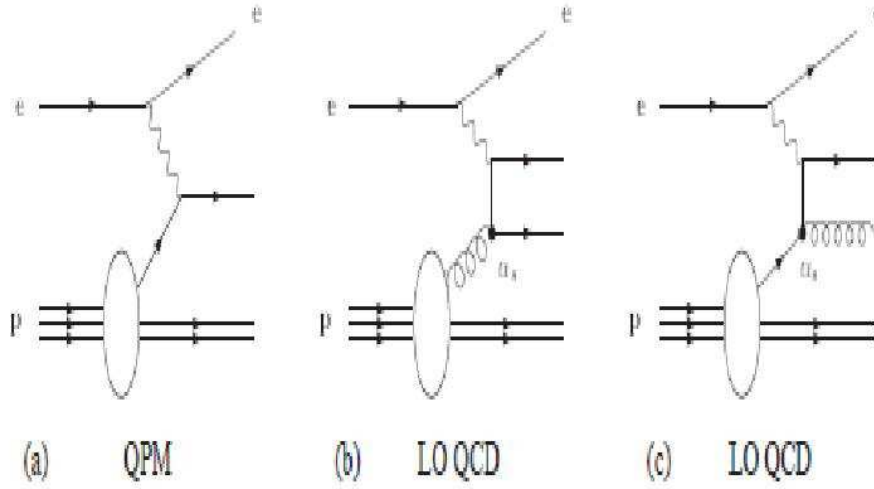


Figure 1.4: (a) A schematic picture of the DIS process in the quark-parton model is shown. (b-c) The extension to QCD is illustrated by the two leading-order (LO) QCD processes

where F_3 contains the parity violating part of the cross section. Since the electro-magnetic coupling conserves parity, this term can be neglected at low Q^2 , where photon exchange dominates the cross section (see Fig.1.3). This can be estimated from the following relation between the γ and the Z_0 contribution to the cross section

$$\frac{\sigma(Z^0)}{\sigma(\gamma)} \sim \left(\frac{Q^2}{Q^2 + M_{Z^0}^2} \right)^2. \quad (1.12)$$

Neglecting the small contribution of longitudinal polarized photons ($O(y^2)$), included in the term $y^2 F_L$, the cross section becomes:

$$\frac{d^2 \sigma^{ep \rightarrow eX}}{dx dQ^2} = \frac{2\pi\alpha^2}{xQ^4} [(1 + (1 - y)^2) F_2(x, Q^2)] \quad (1.13)$$

The computation of the e-proton cross section is performed by assuming the proton to be composed of point-like partons, where point-like means a structure-less Dirac particle. In order to obtain the exact kinematics, we

also have to assume the proton to move with infinite momentum, $|p| \gg M_P$, so that all masses can be neglected. In this frame, the relativistic time dilation slows down the rate at which the partons interact with each others. Therefore, the parton is essentially a free particle when interacting with the virtual photon. An important consequence is that we can imagine the e–proton cross section as a superimposition of probabilities of scattering from single free particles. These probabilities are given by e–parton cross sections, convoluted with the probability $f_i(\xi)$ to pick up that parton from the proton in a certain range of momentum. Indeed, the differential cross section of the process $eq \rightarrow eq$, exchanging a virtual photon γ^* , for a parton with momentum $p = \xi P$ is given by :

$$\frac{d\sigma}{d\Omega} = \frac{\alpha^2}{2s} e_q^2 \frac{4 + (1 + \cos \theta)^2}{(1 - \cos \theta)^2} \quad (1.14)$$

where θ is the scattering angle of the electron in the eq centre-of-mass frame and $d\Omega = d \cos \theta d\phi$. Using $Q^2 = 2E_e^2(1 + \cos \theta)$ and $y = \sin^2 \theta/2$ the differential cross section can be rewritten as:

$$\frac{d^2\sigma^{eq \rightarrow eq}}{dQ^2} = \frac{2\pi\alpha^2}{Q^4} e_q^2 [1 + (1 - y)^2] \quad (1.15)$$

Considering this contribution for each parton, we get

$$\frac{d^2\sigma^{eP \rightarrow eq}}{dx dQ^2} = \frac{2\pi\alpha^2}{xQ^4} \sum_i e_i^2 [1 + (1 - y)^2] f_i(\xi) \quad (1.16)$$

where ξ is the proton momentum fraction carried by the incoming parton. This scheme is usually called *Quark Parton model* (QPM) [1][2], since it describes the inelastic photon–proton interaction as the sum of incoherent proton–parton (quark) elastic scattering. The quarks are assumed to be free (non–interacting) and represent the point–like constituents of the proton. The scale has to be large enough to resolve the constituent substructure. The model predicts the scaling of structure functions or, in other words, the fact that are functions of a single variable, the Bjorken scaling variable x

[3]. Since the structure functions do not depend on Q^2 , in the QPM model the proton looks the same for all values of the probe resolution. Indeed this prediction was confirmed at SLAC for $Q^2 \simeq 4\text{GeV}^2$ [4] and $x \simeq 0.1 \div 0.6$.

With the advent of QCD it became clear that the quarks cannot be considered completely freely moving in the proton when struck by the photon, but they can exchange *gluons*, the carriers of the strong force. The quark parton model is, therefore, only the zero-th order approximation in a perturbative expansion in the strong coupling constant α_s . In the quark parton model the proton was static, whereas in QCD the proton becomes a dynamic system.

The next terms appearing in the perturbative series of the NC cross section correspond to the process $\gamma^*g \rightarrow q\bar{q}$, in which the photon interacts with a gluon from the proton (Figure 1.4 b). The process is called *photon-gluon-fusion* or, more generically, *boson-gluon-fusion (BGF)*. An additional $O(\alpha_s)$ correction is given by the process in which a gluon is emitted from the quark line before or after the scattering with the photon ($\gamma^*q \rightarrow qg$). This process is called QCD Compton-scattering (QCDC). The inclusion of the QCD corrections to the QPM implies that the scaling of the structure functions $F_{1,2}$ is violated. Figure 1.5 shows the proton structure function F_2 as a function of Q^2 , for different values of the Bjorken variable x . For $x \sim 0.1$, the structure function is independent of Q^2 as predicted by the QPM. For $x > 0.1$ decreases with Q^2 , i.e. there is less probability to find a quark q due to gluon radiation. For $x \ll 0.1$ the structure function increases for increasing values of Q^2 , that is, the number of partons resolved by the photon which share the total proton's momentum increases with Q^2 . There is an increased probability of finding a quark at small x and a decreased probability of finding one at high x , because high-momentum quarks lose momentum by radiating gluons [5]. The dependence of the structure functions on Q^2 is described by the QCD evolution equations as DGLAP equations [6, 7, 8].

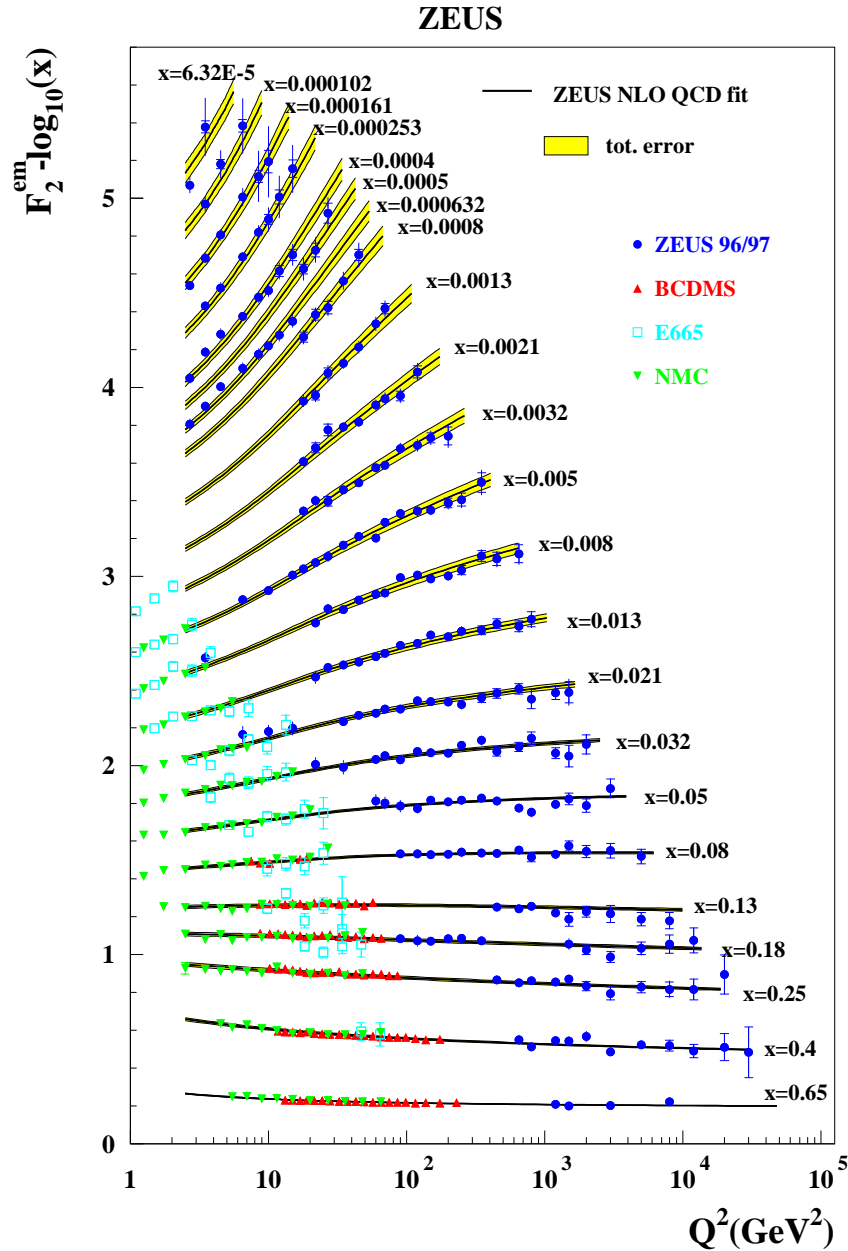


Figure 1.5: The proton structure function F_2 as function of the virtuality of the exchanged photon, for different values of the Bjorken scaling variable x . The experimental points are measured by the ZEUS collaboration and several fixed target experiments. They are compared with a fit performed using next-to-leading order QCD predictions. The error bands on the fit represent the total experimental uncertainty.

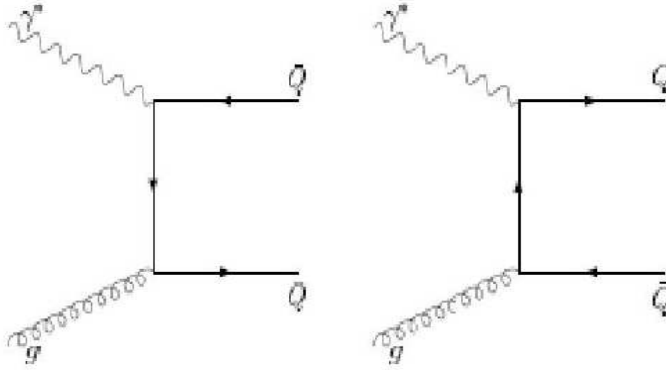


Figure 1.6: Extrinsic heavy quark production via Boson-Gluon-Fusion.

1.3 Heavy quark production in DIS

Two different production mechanisms have been proposed to describe the production of heavy quarks in neutral current DIS reactions.

According to the first mechanism, usually called *intrinsic heavy quark production* one assumes that, besides the light quarks u, d and s and the gluon g , the wave function of the proton also consists of the heavy quarks c, b, t [2, 3]. In the context of the QCD improved quark parton model this means that the heavy quark emerges directly from the proton and interacts with the virtual photon. The consequence is that the cross section depends on a valence-like heavy quark distribution $f_Q(z)$ in the proton. The lowest order process is $\gamma^* Q \rightarrow Q$, whereas including the QCD radiation we also have $\gamma^* + Q \rightarrow Q + g$, where Q is a heavy quark.

The second mechanism is called *extrinsic heavy quark production*. In this case the proton wave function does not contain the heavy quark components. In the lowest order perturbation theory the heavy quark and heavy anti-quark appear in pairs and are produced via BGF as shown in Figure 1.6. In a BGF process the quarks can be heavy if the squared center-of-mass energy of the $\gamma^* g$ system, $\hat{\sigma}$, is :

$$\hat{\sigma} = (\gamma^* + g)^2 = (q + \xi P)^2 > (2m_Q)^2, \quad (1.17)$$

where m_Q^2 is the mass of the heavy quark and the photon and gluon four-momenta are respectively γ^* and $g = \xi P$. In this context the process

$$\gamma^* + g \rightarrow Q + \bar{Q} \quad (1.18)$$

represents the lowest order diagram in which heavy quarks can be produced in deep inelastic ep scattering. The high quark mass sets a hard scale for the process and a reliable description by pQCD calculations should be possible, e.g. demonstrated by the low value of the running coupling α_S at a scale corresponding to the heavy quark mass. Thus the heavy quark production is an excellent test of pQCD. Furthermore heavy flavor measurements provide insights into the gluon contribution of the proton, due to the dominating photon-gluon production process. For high $Q^2 \gg (2m_Q)^2$ the splitting of a gluon into a virtual $Q - \bar{Q}$ pair can be reinterpreted to occur inside the proton and the QPM picture is applicable for the production mechanism. In Figure 1.4 ep-scattering processes up to order α_s are symbolized by Feynman diagrams. The leading order processes in ep-scattering are QPM-like events. In addition virtual corrections to this process have to be taken into account. The next process shown is BGF, the dominant process of heavy quark production at low to medium Q^2 .

1.3.1 BGF cross sections

The cross section of the production of a heavy $Q-\bar{Q}$ pair in BGF can be calculated [9]:

$$\hat{\sigma}_{BGF} = \frac{\pi e_Q^2 \alpha \alpha_S}{\hat{s}} \left[(2 + 2\omega - \omega^2) \ln \frac{1 + \chi}{1 - \chi} - 2\chi(1 + \chi) \right], \quad (1.19)$$

where e_Q denotes the electromagnetic charge of the quark, ω and χ are defined

$$\omega = \frac{4m_Q^2}{\hat{s}}, \quad \chi = \sqrt{1 - \omega} \quad (1.20)$$

The production of charm is favored with respect to beauty due to the different charge and mass of b and c quarks. At the energy of the HERA collider, the beauty quark is mainly produced near the mass threshold. In this kinematic region the cross section of charm quark production is about two orders of magnitude larger.

1.3.2 The NLO program HVQDIS

To allow the evaluation of the NLO QCD prediction for heavy flavour electro–production the virtual-photon-proton cross sections of [10, 11] have been recalculated by Harris and Smith in an exclusive fashion [12]. In other words, in the calculation one does not integrate over the kinematic phase space of the outgoing particles. This enables us to study the single and double differential distributions and correlations among all outgoing particles in the reaction

$$\gamma^* + P \rightarrow Q + \bar{Q} + X \quad (1.21)$$

where $X = 0$ or 1 light parton and to easily incorporate experimental cuts. The calculation was implemented in the Fortran program HVQDIS. The program gives as output the NLO cross sections for $c\bar{c}$ DIS at the parton level (e.g. relative to the produced heavy quark antiquark pair and eventually to the radiated gluon), without hadronization and decay of the produced particles. In the data, the charm cross sections using events in which the heavy quarks produce jets and decay into muons are measured. Therefore, in order to compare the measurements to the NLO predicted cross sections, the NLO prediction needs an implementation of fragmentation and hadronization, and in some cases the measurements have to be extrapolated.

The calculation of parton distributions cannot be achieved from first principles in perturbation theory. Attempts to use non-perturbative methods, for example numerical calculations based on lattice gauge theory, have been so far unable to achieve a level of precision necessary to make a meaningful comparison with the experimental measurements. However what can be calculated perturbatively is how they depend on the factorization scale.

The muon selection requires the hadronisation of the parton final state. The fragmentation of a c quark to a muon is performed using the Peterson function [14]. The decay spectrum of the charmed hadron to the muon is taken from JETSET. The following parameter set is used for the calculation:

- Proton PDF: CTEQ5F3
- charm quark mass: 1.5 GeV
- factorisation and renormalisation scales are set to:

$$\mu_R = \mu_F = (Q^2 + 4m_C^2) \quad (1.22)$$

- $\Lambda_{QCD} = 0.39$ GeV according to the value of fit used in the CTEQ5F3 PDF
- Peterson fragmentation with $\epsilon = 0.0035$
- C hadron branching ratio into muons: 0.096

The dominant systematic error on the NLO QCD dis to muon charm quark cross section prediction originates from the chosen factorisation and renormalisation scales and the charm quark mass. The influence from the proton PDF, fragmentation and Λ_{QCD} are negligible when added in quadrature. Anyway, no systematic error on the NLO QCD predictions will be used to compare to the measured cross sections of this thesis (see Chapter 5).

1.4 Measurements of heavy quark production in ep collisions

The large heavy-quark masses provide a hard scale, making perturbative Quantum Chromodynamics applicable. However, a hard scale can also be given by the transverse jet energy and by Q^2 . The presence of two or more scales can lead to large logarithms in the calculation which can spoil the convergence of the perturbative expansion. The agreement between fixed order calculations and the measured cross sections is not obvious. The previous measurements are based on D^* meson decays or the impact parameter of the long-lived particles.

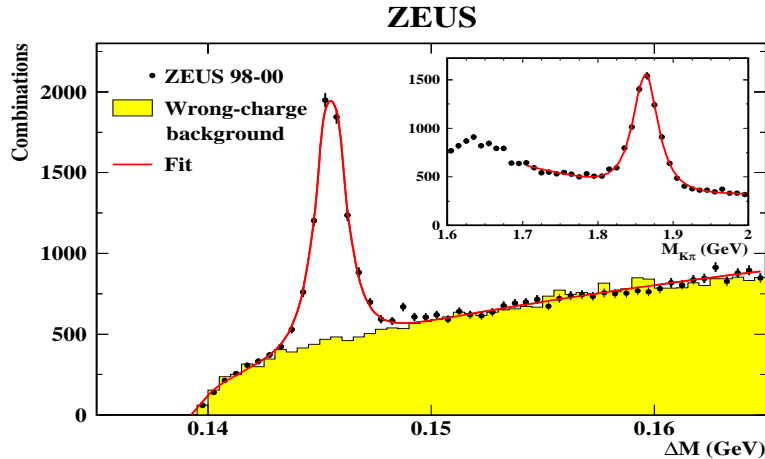


Figure 1.7: The distribution of the mass difference, $\Delta M = (M_{K\pi\pi_s} - M_{K\pi})$, for D^* candidates (solid dots). The ΔM distribution from wrong-charge combinations, normalised in the region $0.15 < \Delta M < 0.165$ GeV, is shown as the histogram. The solid line shows the result of the fit described in the text. The $M_{K\pi}$ distribution for the D^0 candidates in the range $0.143 < \Delta M < 0.148$ GeV is shown as an inset. The fit is the sum of a modified Gaussian to describe the signal and a second-order polynomial to describe the background.

1.4.1 Inclusive $D^{*\pm}$ cross sections at ZEUS

Differential cross sections of a $D^{*\pm}$ meson in the DIS regime have been measured by ZEUS at HERA I using an integrated luminosity of 81.9 pb^{-1} [15]. The measurement was performed in the kinematic range of $1.5 < Q^2 < 1000 \text{ GeV}^2$ and $0.02 < y < 0.7$ and compared to the "massive" fixed-order next-to-leading-log(FONLL) calculation.

The D^* mesons were identified using the decay channel $D^{*+} \rightarrow D^0\pi_S^+$ with the subsequent decay $D^0 \rightarrow K^-\pi^+$ and the corresponding antiparticle decay. The signal regions for the reconstructed masses, $M(D^0)$ and $\Delta M = (M_{K\pi\pi_s} - M_{K\pi})$, where $1.80 < M(D^0) < 1.92 \text{ GeV}$ and $0.143 < \Delta M < 0.148 \text{ GeV}$, respectively. To allow the background to be determined, D^0 candidates with wrong-sign combinations, in which both tracks forming the D^0 candidates have the same charge and the third track has the opposite charge, were also retained. The kinematic region for D^* candidates was

$1.5 < p_T(D^*) < 15$ GeV and $|\eta(D^*)| < 1.5$. Figure 1.7 shows the ΔM distribution for the D^* candidates together with the background from the wrong-charge combinations. The number of D^* candidates determined in the two signal regions after having subtracting the background estimated from the wrong-charge sample was 5545 ± 129 .

Measurements were made as a function of Q^2 , x , the pseudo-rapidity of the D^* , $\eta(D^*)$, and the transverse momentum of the D^* , $pt(D^*)$ (see figure 1.8). The predictions from NLO QCD are in reasonable agreement with the measured cross section; they show sensitivity to the choice of PDF and hence the gluon distribution in the proton. The double-differential cross section in y and Q^2 has been measured and used to extract the open-charm contribution to F_2 , by using the NLO QCD calculation to extrapolate outside the measured $pt(D^*)$ and $\eta(D^*)$ region. Since the uncertainties of the data at low Q^2 were comparable to those from PDF fit, the measured differential cross sections in y and Q^2 could also be used in fits to constrain the gluon density. Inclusive production of D^* mesons Charm in DIS has been measured at HERA II as well using the data taken during the 2003-05 running period. These new results [16] are comparable with previous ones and extend the kinematic region to larger pseudorapidity, $\eta(D^*)$. Good agreement is seen even in this case for the differential cross sections and the extension to the forward $\eta(D^*)$ region allows a smaller extrapolation factors when extracting the proton structure function $F_2^{c\bar{c}}$.

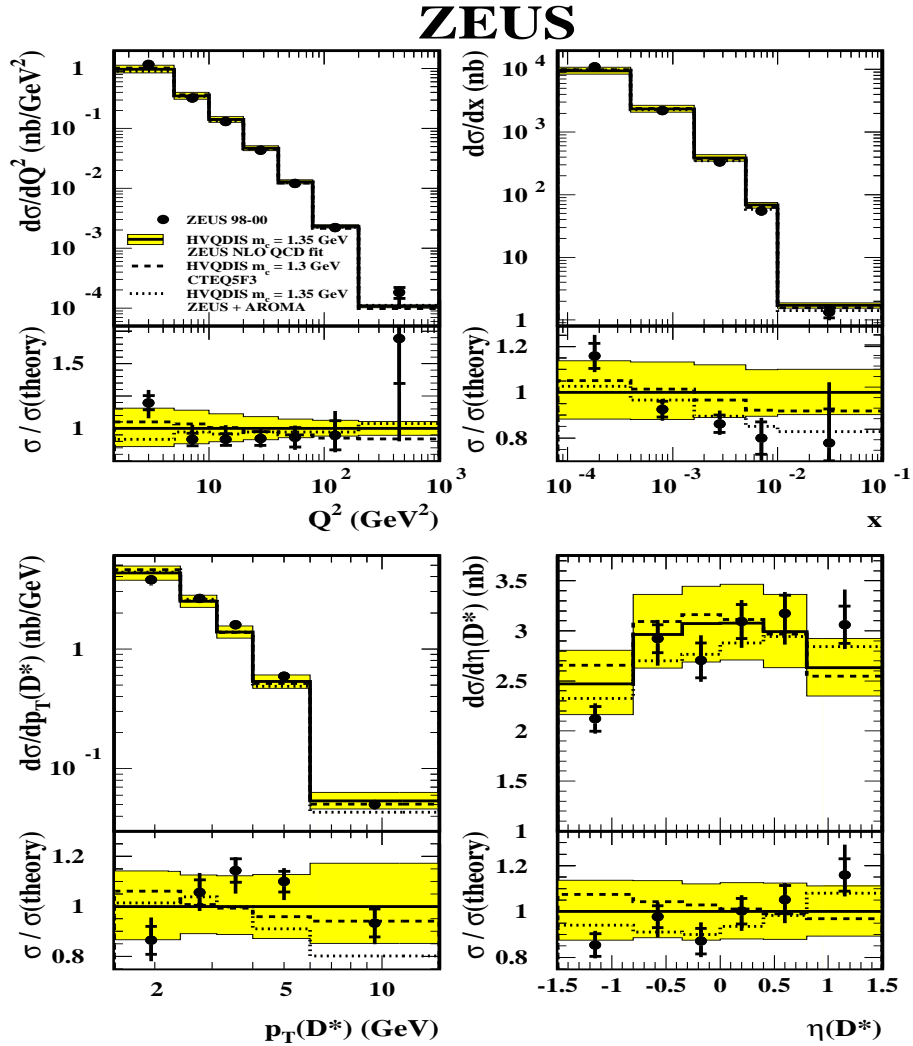


Figure 1.8: Differential D^* cross sections, for e^-p and e^+p data combined, as a function of (a) Q^2 , (b) x , (c) $p_T(D^*)$, (d) $\eta(D^*)$.

The values of the $F_2^{c\bar{c}}$ are presented as a function of Q^2 at fixed values of x and compared with the ZEUS NLO QCD fit in Fig. 1.9. The data rise with increasing Q^2 , with the rise becoming steeper at lower x , demonstrating the property of scaling violation in charm production. The data are well described by the predictions.

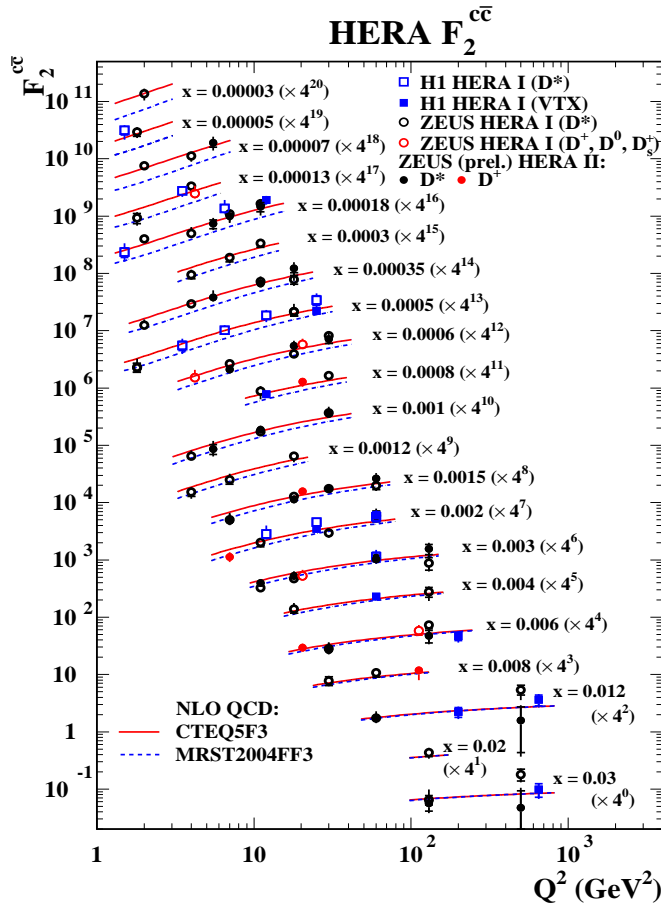


Figure 1.9: The measured $F_2^{c\bar{c}}$ at x values between 0.00003 and 0.03 as a function of Q^2 . The data are shown with statistical uncertainties (inner bars) and statistical and systematic uncertainties added in quadrature (outer bars). The lower and upper curves show the fit uncertainty propagated from the experimental uncertainties of the fitted data. The H1 data are also shown with the blue points.

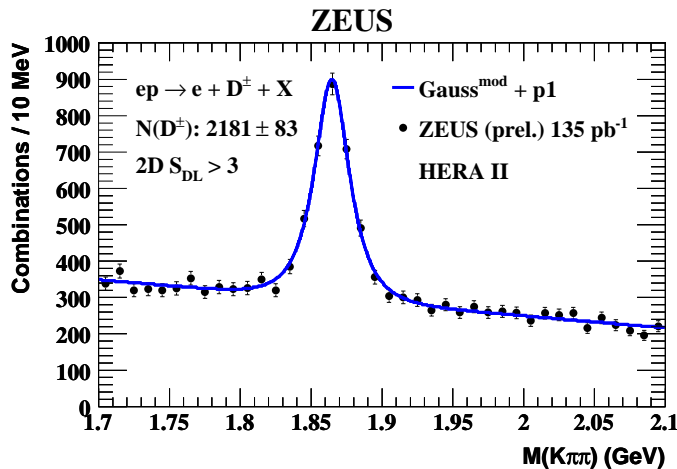


Figure 1.10: Mass distribution with significance cut for the D^\pm meson .

1.4.2 Charm cross section from other mesons in DIS

Very interesting preliminary results has been presented by ZEUS Collaboration at HERA II by measuring the secondary vertex from a D-meson (D^\pm or D^0) decay or from the impact parameter of the identified leptons [17]. The $D^\pm \rightarrow K^\mp + \pi^\pm + \pi^\pm$ decay channel has been used as well as $D^0 \rightarrow K^\mp + \pi^\pm$. The D^\pm mesons have a long lifetime of $c\tau \sim 315 \mu m$ [18] and D^0 mesons have a shorter lifetime of $c\tau \sim 123 \mu m$ [18].

To select D^\pm mesons, in each event all track pairs with equal charge and a third track with opposite charge have been combined to form the D^\pm candidates. The pion mass was assigned to the two tracks with equal charges and the kaon mass was assigned to the third track. The three tracks were refitted to a common vertex and subsequently, the D^\pm candidate invariant mass, $m(K\pi\pi)$ was calculated. The signed decay length, L , was also used, defined as: $L = |\vec{l}| \text{sign}(\vec{l} \cdot \vec{p}_D)$ with $\vec{l} = \vec{r}_2 - \vec{r}_1$ where the primary vertex coordinates are given by \vec{r}_1 and the secondary vertex coordinates by \vec{r}_2 . The quantity \vec{p}_D represented the refitted momentum vector of the D^\pm candidate. The uncertainties in the determination of the primary vertex and of D^\pm candidate vertex were also calculated and used to define the decay

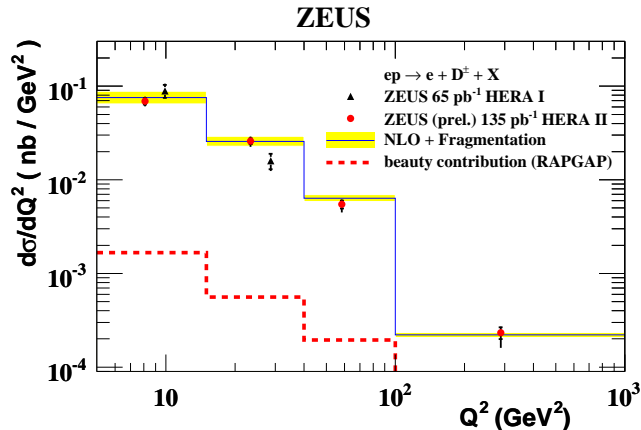


Figure 1.11: Differential D^\pm cross section as a function of Q^2 compared to NLO QCD calculation of HVQDIS [12]. The HERA II data (solid points) are shown compared to the most recently published ZEUS experiment (solid triangles). The inner error bars indicate the statistical uncertainties added in quadrature. The solid line gives the predictions from the ZEUS NLO QCD fit for $m_c = 1.35\text{GeV}$ with the shaded band indicating the uncertainty in the prediction.

length significance as $S_L = L/\sigma_L$. A cut on $S_L > 3$ was chosen for the D^\pm mesons to obtain the best signal to background ratio (see Fig.1.10). The D^0 mesons were reconstructed in an identical manner to the D^\pm , except that only oppositely-charged pairs of tracks were combined together to form the D^0 . Differential cross sections for D^\pm and D^0 mesons in Q^2 , $p_T(D)$ and $\eta(D)$ have been measured (see Fig. 1.11 and Fig. 1.12). The values of $F_2^{c\bar{c}}$ are presented as function of Q^2 at fixed values of x and compared with other results from HERA in fig.1.9). The data from the D^\pm analysis are shown as the solid red points and are compatible with other determinations of $F_2^{c\bar{c}}$ using different methods. The data are compared to two sets of NLOQCD parton density functions, CTEQ5F3 and MRST2004FF3, which were extracted from global fits to mainly DIS data. The data shown have some discriminating power at low Q^2 , where the theoretical predictions have different shapes.

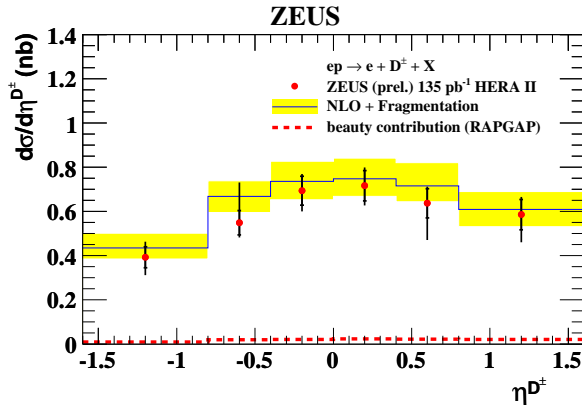


Figure 1.12: Differential D^\pm cross section as a function of $\eta(D^\pm)$ compared to NLO QCD calculation of HVQDIS. The solid points show the HERA II data with the inner error bars indicating the statistical uncertainties and the outer bars showing the statistical and systematic uncertainties added in quadrature. The solid line gives the predictions from the ZEUS NLO QCD fit for $m_c = 1.35\text{GeV}$ with the shaded band indicating the uncertainty in the prediction.

1.4.3 Charm cross section using Impact Parameter

Measurements of the open charm cross section in DIS at HERA have mainly been of exclusive D or D^* meson production. From these measurements the contribution of charm to the proton structure function is derived by correcting for the fragmentation function $f(c \rightarrow D)$. A measurement of charm and beauty inclusive cross section using impact parameter has been also published from H1 collaboration at HERA [19] (see Fig.1.13). The analysis presented regards ep scattering in the range $Q^2 > 150\text{GeV}^2$ and inelasticity $0.1 < y < 0.7$; the sample corresponds to an integrated luminosity of 57.4pb^{-1} , taken in the year 1999-2000. The charm and beauty fractions are determined using a method based on the impact parameter, i.e. the transverse distance of closest approach to the primary vertex point. We can distinguish heavy from light quark events by the long lifetimes of c and b flavoured hadrons, which lead to displacements of tracks from the primary vertex. The distance of a track to the primary vertex is reconstructed using

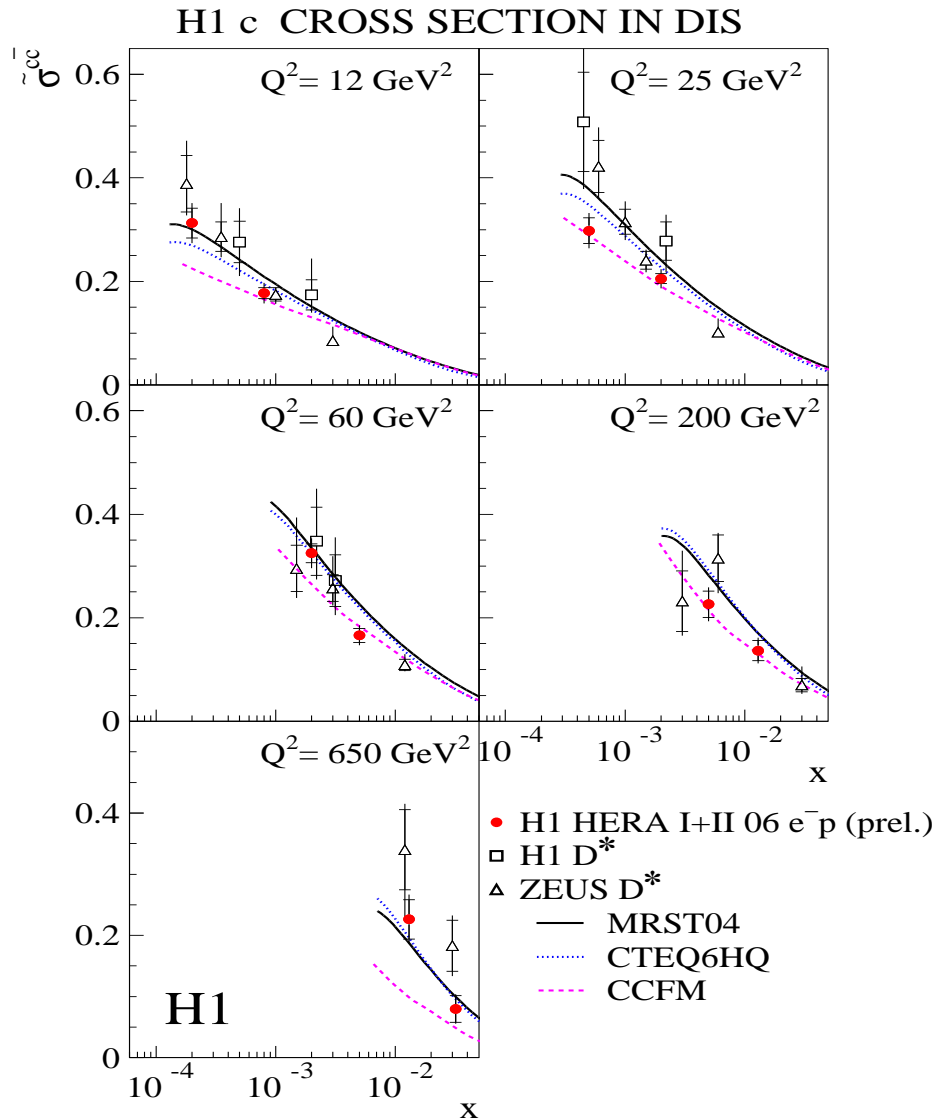


Figure 1.13: The measured HERA I and II average reduced cross section $\sigma^{c\bar{c}}$ shown as a function of x for 5 different Q^2 values. The inner error bars show statistical error, the outer error represent statistical and systematic uncertainties added in quadrature. The measurements obtained for D^* mesons from H1 and ZEUS and predictions of QCD are also shown.

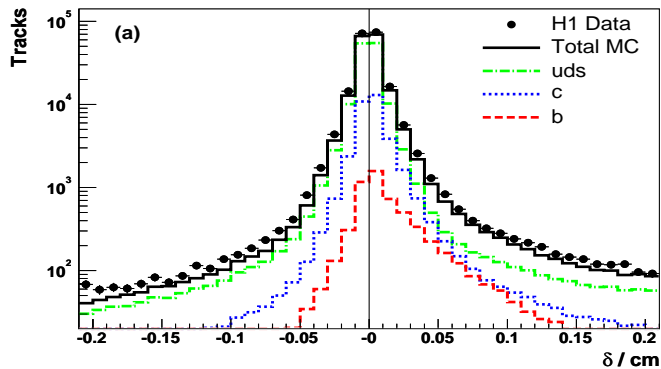


Figure 1.14: The signed impact parameter δ of a track to the primary vertex in the x - y plane.

precise spatial information from the H1 vertex detector. In order to calculate a signed impact parameter δ for each track, a 'jet axis' is defined. Jets with a minimum p_T of 5 GeV, in the angular range $10^\circ < \theta < 70^\circ$, are reconstructed using k_T algorithm in the laboratory frame. The jet axis is defined as the direction of the highest p_T jet or, if there is no jet reconstructed, the 'direction of the struck quark' in the quark parton model, given by the angle of the hadronic system. For tracks associated to the jet, δ is defined as positive if the angle between the jet axis and the line joining the primary vertex to the point of DCA (Distance of closest Approach) is less than 90° and is defined negative otherwise. Tracks from the decays of long lived particles will mainly have a positive δ . Tracks produced at the primary vertex result in a symmetric distribution around $\delta = 0$, i.e. negative δ tracks mainly result from detector resolution (see Fig.1.14). The data are seen to be asymmetric with positive values in excess of negative values indicating the presence of long lived particles. The component of the simulation that arises from light quarks is almost symmetric at low δ . The asymmetry at $\delta \gtrsim 0.1$ cm is mainly due to long lived strange particles such as K_S^0 . The c component exhibits a moderate asymmetry and the b component shows a marked asymmetry. The differences are due to the different lifetimes of the produced hadrons.

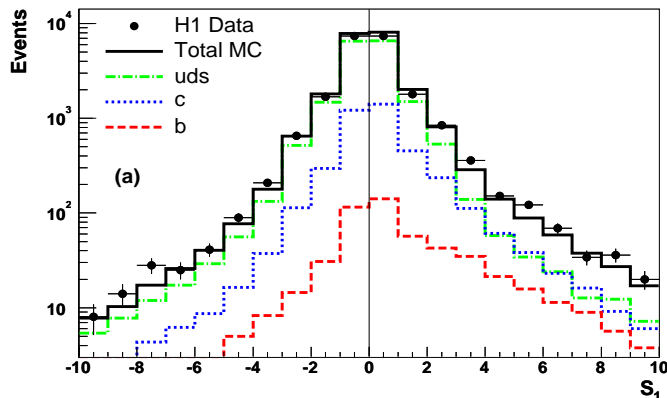


Figure 1.15: The significance $\delta/\sigma(\delta)$ where $\sigma(\delta)$ is the error on δ , for all tracks associated to the jet axis. Included in the figure is the expectation from the RAPGAP Monte Carlo simulation, showing the contribution from the various quark flavours after applying the scale factors obtained from the fit to the subtracted significance distributions of the data.

In order to optimise the separation of the quark flavours use is made of the significance, defined as the ratio of δ to its error.

A further optimisation is made by using different significance distributions for events with different multiplicities. The first significance distribution S_1 is defined for events where only one reconstructed track is linked to the jet, and is simply the significance of the track. The second significance distribution S_2 is defined for events with two or more tracks associated with the jet and is the significance of the track with the second highest absolute significance. Only events in which the tracks with the first and second highest absolute significance have the same sign are selected for the S_2 distribution. The second highest significance track is chosen because for heavy quarks ≥ 2 tracks are usually produced with high significance, whereas for light quarks the chances are small of two tracks being produced at large significance due to resolution effects. The S_1 distribution is shown in figure 1.15. The distribution of S_2 gives a better separation power of light to heavy quarks. Events with one track are retained to improve the statistical precision of the measurements.

In order to substantially reduce the uncertainty due to the resolution of δ and the light quark normalisation the negative bins in the S1 and S2 distributions are subtracted from the positive.

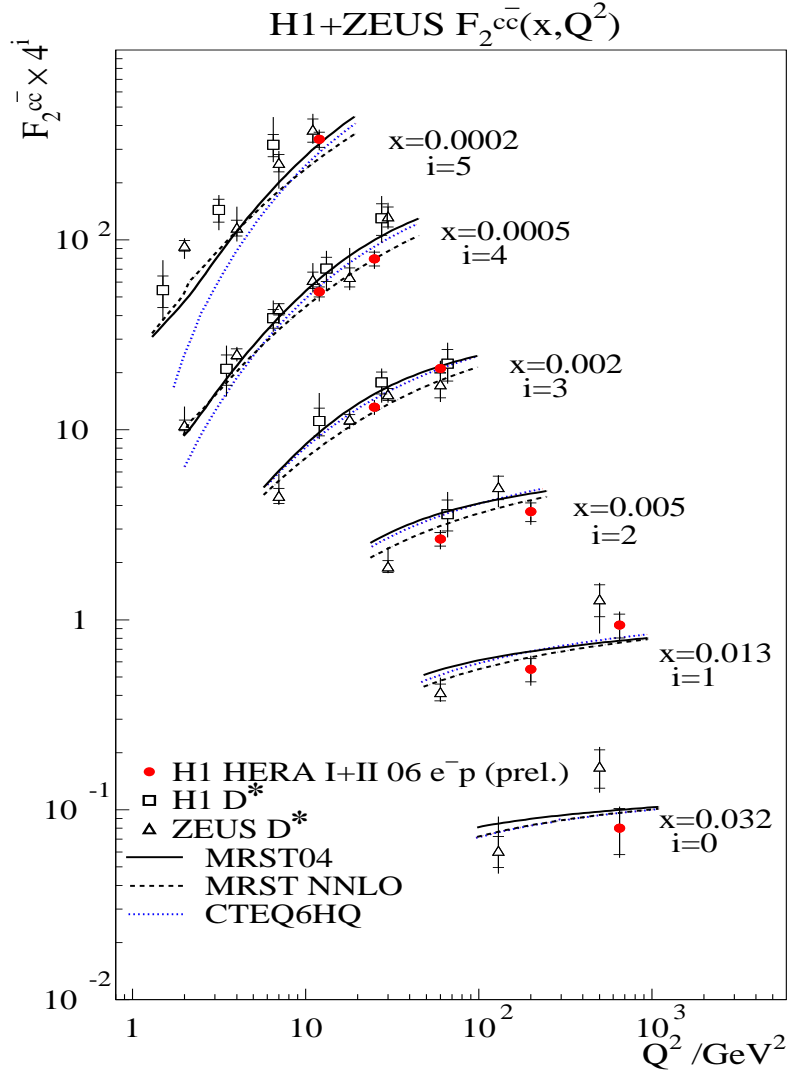


Figure 1.16: The measured HERA I and II averaged $F_2^{c\bar{c}}$ shown as a function of Q^2 for various x . The inner error bars show the statistical errors, the outer error bars represent statistical and systematic uncertainties added in quadrature. The measurements obtained for D^* mesons from H1 and ZEUS and predictions of QCD are also shown.

The resulting distributions are dominated by c quark events, with an increasing b fraction with increasing significance. The fractions of c , b and light quarks of the data are extracted in each $x - Q^2$ bin using a least squares simultaneous fit of the subtracted S_1 and S_2 distributions and the total number of inclusive events before track selection. The results of the fit in each $x - Q^2$ interval are converted to a measurement of the differential cross section. Similar results have been obtained from the combination of this analysis with a preliminary analysis that has been made by H1 collaboration [20] with 2006 data corresponding to an integrated luminosity of $54 pb^{-1}$ (see Fig. 1.13).

The kinematic region has been expanded to $12 \leq Q^2 \leq 650 GeV^2$ and to $0.000197 \leq x \leq 0.032 GeV^2$. The data are divided into five regions in Q^2 and six regions in Bjorken x , and values for the structure function $F_2^{c\bar{c}}$ are obtained. These new results are found to be compatible with the predictions of perturbative quantum chromodynamics (see fig. 1.13 and 1.16).

1.4.4 Beauty production in DIS at HERA

The beauty production cross section for deep inelastic scattering with the ZEUS detector has been measured using an integrated luminosity of $72 pb^{-1}$ for HERA I data. Due to the larger mass, the theoretical prediction is expected to be precise. However the measured cross sections have big uncertainties because of the low statistics. Events with at least one hard jet in the Breit frame, with $E_{Tjet}^{Breit} > 6 GeV$ and with a muon from a b decay and for photon virtualities $Q^2 > 2 GeV^2$ have been selected. A significant background to these processes was due to muons in-flight decays of pions and kaons. These background sources were partly rejected by the cuts $p^\mu > 2 GeV$ and $p_T^\mu > 2 GeV$. Background muons can also be originated from the semi-leptonic decay of charmed hadrons. At that time, without the Micro Vertex Detector that has been available only after the HERA upgrade, the only way to distinguish beauty from charm was to use the transverse momentum of the muon with respect to the axis of the closest jet, p_T^{rel} . For muons coming

from charm decays or in events induced by light quarks, the p_T^{rel} values are low. Therefore, the fraction of events from b decays, in the data sample could be extracted on a statistical basis by fitting the relative contributions of the simulated beauty, charm and light-quark decays to the measured p_T^{rel} distribution. The NLO QCD prediction for the visible cross sections obtained with HVQDIS lay about 2.5 standard deviations below the measured value. Also the prediction from the RAPGAP MC is ~ 2 times lower than data (see fig. 1.17).

Similar results with a different (HERA II) event sample have been delivered in a recent ZEUS analysis. In this case, a wider kinematic region has been selected, with cut on $Q^2 > 4 GeV^2$, $p^\mu > 1.5$ and $\eta_\mu > -1.6$. The measured total cross section is about 2σ higher than the NLO prediction. The figure 1.18 shows the reduced cross section extrapolated to the full phase space as a function of x for different bins of Q^2 ; even for this analysis ZEUS data lie above theoretical prediction. The figure shows also H1 data obtained from the inclusive impact parameter analysis [19]. The red points belong to H1 collaboration and are calculated using the impact parameter method already explained in the previous paragraph for charm production. The two experiments seem to be compatible within errors even if a large spread between theory predictions is visible.

ZEUS

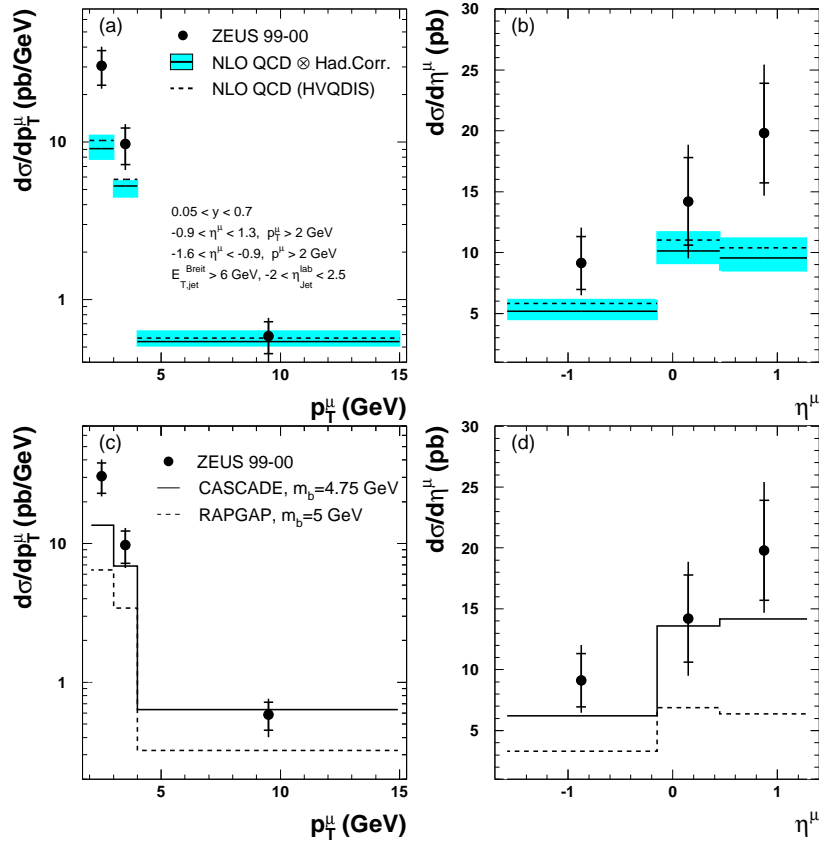


Figure 1.17: Differential b -quark cross section as a function of (a) the muon transverse momentum p_T^μ and (b) muon pseudo rapidity η^μ in the laboratory frame, compared to NLO QCD calculations. Differential b -quark cross section as a function of (c) p_T^μ and (d) η^μ , compared with NLO QCD MC programs CASCADE (solid line) and RAPGAP (dashed line)

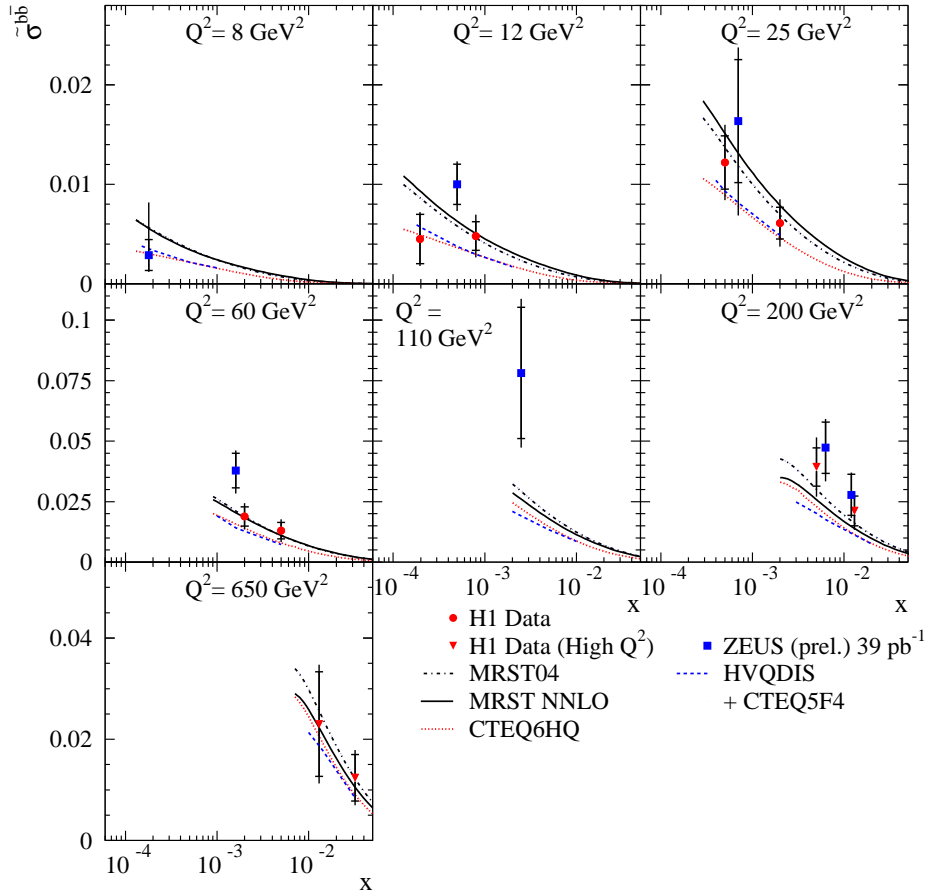


Figure 1.18: The measured HERA I and II averaged reduced cross section $\bar{\sigma}^{bb}$ shown as a function of different Q^2 values. The inner error bars show the statistical error, the outer error bars represent the statistical and systematic error added in quadrature. The preliminary data from ZEUS and the prediction of QCD are also shown.

Chapter 2

HERA and the ZEUS detector

In this chapter the HERA accelerator and the ZEUS detector are described briefly, giving particular emphasis on the parts of the detector used in the analysis described in this thesis. A detailed description of the ZEUS detector can be found in [21].

2.1 The HERA collider

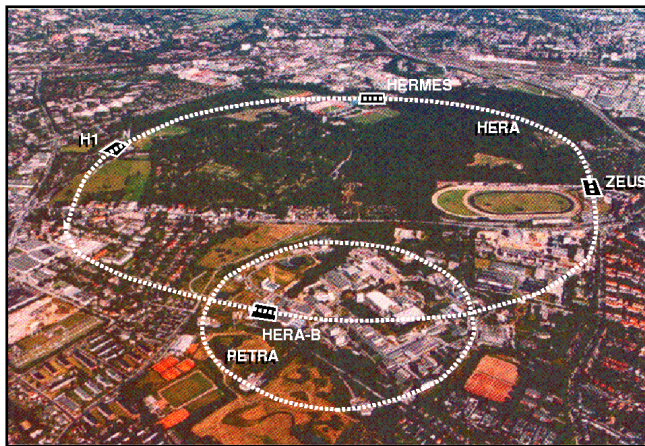


Figure 2.1: *The Hamburg Volkspark showing the DESY site. The location of the HERA and PETRA rings are shown. Also illustrated are the locations of the two colliding-beam experiments, ZEUS and H1, together with the single-beam experiments HERMES and HERA-B.*

The HERA (Hadron Elektron Ring Anlage) collider was a unique particle accelerator for the study of high-energy electron-proton (ep) collisions [22]. It was located at the DESY (Deutsches Elektronen SYNchrotron) laboratory in Hamburg, Germany, and has been in operation from 1992 to 2007. The HERA ring was located 15-30 m under ground level and had a circumference of 6.3 km. Fig 2.1 shows an aerial view of the tunnel area in Hamburg and the position of the different experiment halls; the ring had 4 linear sections linked at their extremities by 4 arcs of 779 m radius (see Fig 2.2). The HERA machine collided electrons and positrons, accelerated to an energy of 27.5 GeV, with 820 (920) GeV protons (the energy of the proton beam was changed at the beginning of 1998 from 820 to 920 GeV). The resulting centre-of-mass energy was 300 (318) GeV, more than an order of magnitude higher than previous fixed-target lepton-nucleon experiments.

Four experiments were located in four experimental halls placed along the HERA ring (Fig. 2.1 and 2.2). The two beams were brought into collision every 96 ns at zero crossing angle at two interaction points, one in the North Hall where the H1 experiment was located, the other in the South Hall where the ZEUS experiment was placed. In the East Hall the Hermes experiment studied the spin structure of the nucleon using the collisions of longitudinally polarized leptons on an internally polarized gas target (H, ^2D or ^3He). The HERA-B experiment, located in the West Hall was used until 2003 to collide the proton beam halo with a wire target to study B-meson production.

Built between 1984 and 1990, the HERA collider started operation in 1992 in its initial configuration with 820 GeV protons and 26.7 GeV electrons. In 1994 it was realized that the electron beam current was limited by positively ionized dust particles in the beam pipe through the pumps, reducing the lifetime of the beam. For this reason HERA switched to positrons in July 1994, achieving a more stable lepton beam and a significant increase in the integrated luminosity of the collected data. During the 1997-98 shutdown period, new pumps were installed in the lepton beam to improve the electron

beam lifetime, and during 1998 and part of 1999 HERA was run again with electrons. In 1998 the energy of the proton beam was raised from 820 to 920 GeV, switching back to positron-proton collisions in 1999. This phase is called HERA I and the total delivered luminosity up to 2000 was 193.2 pb⁻¹.

Although a lot of interesting measurements had already been performed at HERA I, the desire was expressed by the experiments for an increase in the luminosity. The motivations for this increase were studied in a one-year workshop held between 1995 and 1996, when it was concluded that having ~ 1 fb⁻¹ of integrated luminosity would open up the possibility of new interesting measurements [23].

During the shutdown 2000/2001, the HERA collider was upgraded to achieve a five times higher specific luminosity at the collision point [24]. In addition spin rotators were included to rotate the spin of the leptons such that the lepton beam was longitudinally polarized at all interaction regions. A further longer shutdown was necessary in the middle of 2003 to solve severe background problems [25]. Since October 2003, till the end of 2006, HERA provided stable beam operations and delivered a total luminosity of 556.3 pb⁻¹.

Before the end of data-taking (June 2007), special proton low energy runs have been delivered in order to measure the longitudinal structure function F_L . This measurement should allow to decompose the contributions of the F_L and F_2 structure functions to the DIS cross section at low Q^2 and provide an important cross check of the conventional QCD at low x ; furthermore it could allow to improve the knowledge of the gluon density. HERA agreed with ZEUS and H1 collaborations to run with two different proton energies (see Table 2.2): 460 GeV (Low Energy Run) and 575 GeV (Medium Energy Run). HERA delivered 15.7 pb⁻¹ during LER period (from January to April 2007) and 8.1 pb⁻¹ during MER (from April to June 2007) with very high efficiencies ($\sim 90\%$).

A summary of HERA I and HERA II parameters during the running periods 1993-2000 and 2003-2007 can be found in Table 2.1-2.2. Fig. 2.3 and 2.4 shows the HERA and ZEUS luminosity during HERA II data taking.

Running period	1993-1997		1998-2000	
Luminosity	$1.5 \cdot 10^{31} \text{ cm}^{-2} \text{ s}^{-1}$		$1.5 \cdot 10^{31} \text{ cm}^{-2} \text{ s}^{-1}$	
Center-of-mass energy	300 GeV		318 GeV	
	lepton	proton	lepton	proton
Energy (GeV)	30	820	27.5	920
Max number of bunches	210	210	210	210
Beam current(mA)	43	163	43	163
Particles per bunch	$3.65 \cdot 10^{10}$	10^{11}	$3.65 \cdot 10^{10}$	10^{11}
Beam width (σ_x)	0.286 mm	0.280 mm	0.286 mm	0.280 mm
Beam height (σ_y)	0.060 mm	0.058 mm	0.060 mm	0.058 mm

Table 2.1: *HERA I design parameters [26][27].*

Running period	2003-2006		2007 LER		2007 MER	
Luminosity	$7.0 \cdot 10^{31} \text{ cm}^{-2} \text{ s}^{-1}$		$1.47 \cdot 10^{31} \text{ cm}^{-2} \text{ s}^{-1}$		$1.47 \cdot 10^{31} \text{ cm}^{-2} \text{ s}^{-1}$	
Center-of-mass energy (GeV)	318		225		251	
	lepton	proton	lepton	proton	lepton	proton
Energy (GeV)	27.5	920	27.5	460	27.5	575
Max number of bunches	184	180	180	180	180	180
Beam current(mA)	58	140	38	140	58	140
Particles per bunch	$4.18 \cdot 10^{10}$	10^{11}	$4.18 \cdot 10^{10}$	10^{11}	$4.18 \cdot 10^{10}$	10^{11}
Beam width (σ_x)	0.118 mm	0.118 mm	0.118 mm	0.118 mm	0.118 mm	0.118 mm
Beam height (σ_y)	0.032 mm	0.032 mm	0.032 mm	0.032 mm	0.032 mm	0.032 mm

Table 2.2: *HERA II parameters [26][27].*

2.1.1 The HERA injection system

HERA provided two different injection systems for the beams, shown in Fig. 2.2.

The proton acceleration chain started with negative hydrogen ions (H^-) accelerated in a LINAC to 50 MeV. The electrons were then stripped off the H^- ions to obtain protons, which were injected into the proton synchrotron DESY III and accelerated up to 7.5 GeV in 11 bunches with a temporal gap of 96 ns, the same as the main HERA ring; these bunches were then transferred to PETRA, where they were accelerated to 40 GeV. Finally they were injected into the HERA proton storage ring, and the injection stopped when the ring contained 210 bunches. Through the radiofrequency generated in resonant cavities, the proton beam was then accelerated up to 920 GeV.

Pre-acceleration of the electrons (positrons) started in two cascaded linear accelerators, LINAC I and LINAC II, where the leptons were accelerated up to 250 and 450 MeV respectively. The leptons were then injected into DESY

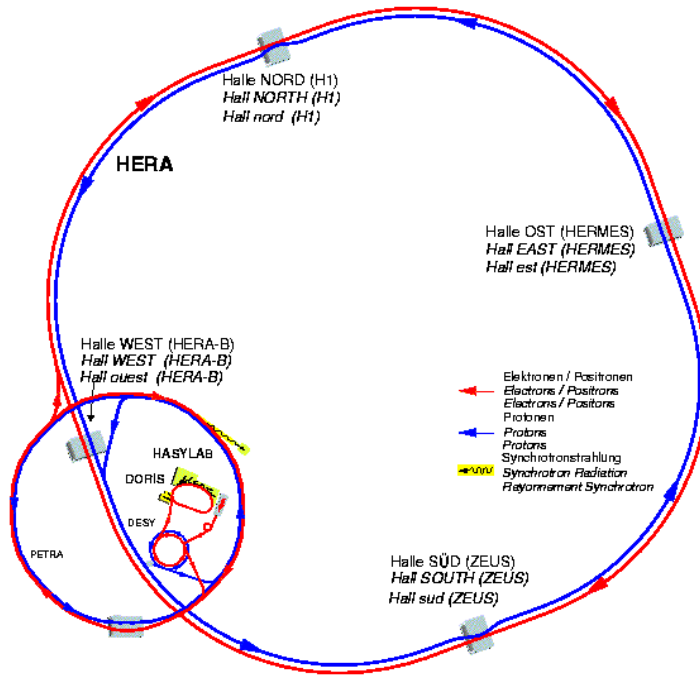


Figure 2.2: *HERA injection system.*

II, accelerated to 7.5 GeV and then transferred to PETRA II, where they reached an energy of 14 GeV in bunches separated by 96 ns gaps. They were then injected into HERA where they reached the nominal lepton beam energy of 27.5 GeV, again until the main ring was filled with 210 bunches. Some of these bunches were kept empty (pilot bunches) in order to study the background conditions. When either the lepton or the proton bunch was empty, the beam related background, originating from the interaction of the lepton or the proton beam with the residual gas in the beam pipe, could be studied, whereas when both the bunches were empty the non-beam-related background, such as cosmic ray rates, could be estimated.

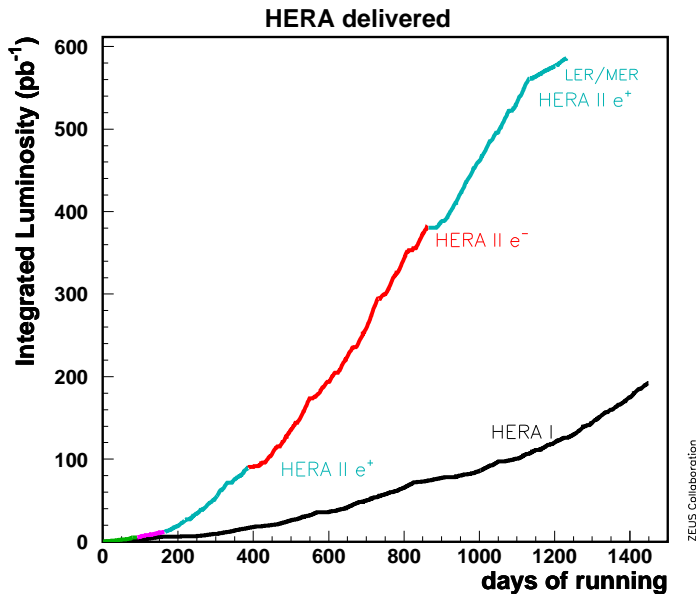


Figure 2.3: *HERA luminosity for the whole working period.*

2.2 The HERA luminosity

HERA started delivering data in June 1992. Since then the luminosity has continuously increased, as shown in Fig. 2.3.

At HERA the luminosity is effectively defined as:

$$L = \frac{f_r \sum_i N_p^i \cdot N_e^i}{2\pi\sigma_x\sigma_y\beta_{yp}^*} \quad (2.1)$$

where f_r represents the beam revolution frequency, N_p^i is the number of protons in the i -th bunch, N_e^i is the number of electron in the i -th bunch; σ_x, σ_y represent the interaction region sizes, where $\sigma_x = \sqrt{\sigma_{x_e}^2 + \sigma_{x_p}^2}$ and $\sigma_y = \sqrt{\sigma_{y_e}^2 + \sigma_{y_p}^2}$. These variables are connected to the corresponding beta function and emittances: $\sigma_\alpha = \sqrt{\beta_\alpha^* \epsilon_\alpha}$

Increasing the intensities of the beams to substantially improve the luminosity would have required a huge financial cost (the currents of the leptonic

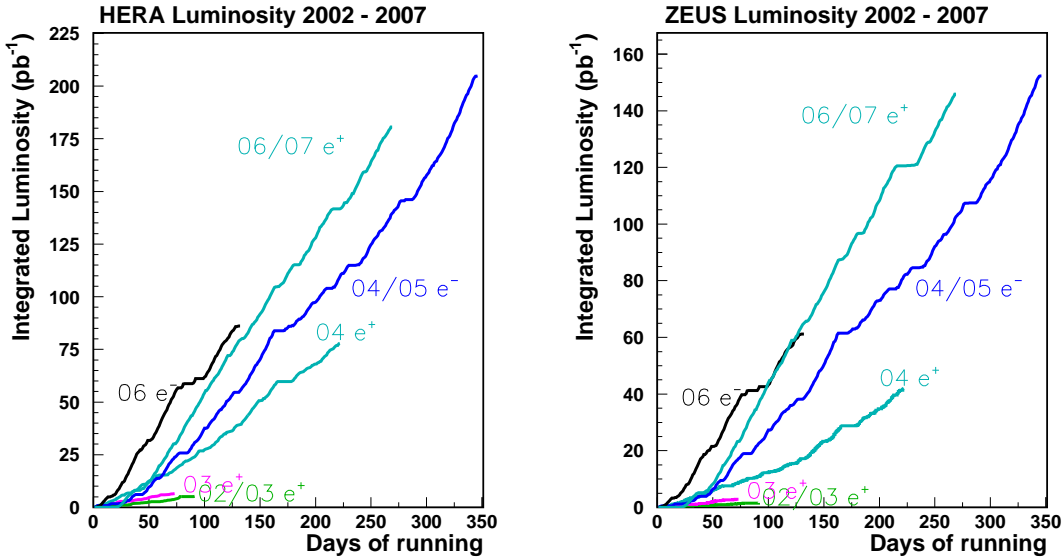


Figure 2.4: HERA integrated luminosity and ZEUS integrated luminosity available for analysis.

beam could only have been incremented increasing in an almost proportional way the power of the radiofrequency cavity). Rather the luminosity was increased by making the interaction cross-section smaller by reducing the beta functions at the interaction point. These functions are limited by chromatic effects and limitations on the “opening” of the low beta quadrupoles. In order to increase the luminosity up to $\sim 7.4 \cdot 10^{31} \text{ cm}^{-2} \text{ sec}^{-1}$ new superconducting magnets [28] close to the interaction point (inside the calorimeter volume), an absorption system for the synchrotron radiation and for the vacuum were installed in the interaction region.

During the break, planned in order to upgrade the accelerator, the Micro Vertex Detector (MVD) was positioned inside the cavity between the beam pipe and the inner wall of the Central Tracking Detector (CTD).

2.3 The ZEUS detector

ZEUS was a multi-purpose, magnetic detector designed to study electron/positron-proton collisions. It measured $12 \times 10 \times 19 \text{ m}^3$, weighted 3600 tonnes and it

was quasi-hermetic, covering most of the 4π solid angle, with the exception of the small regions around the beam pipe.

As a result of the asymmetric beam energies, most of the final state particles were boosted in the proton beam direction. Consequently, the sub-detectors of ZEUS were coaxial but asymmetric with respect to the interaction point. The detector could measure energies of $\sim 100 \text{ MeV}$ to hundreds of GeV in the forward region. For low momentum particles the tracking in the magnetic field was very precise, while high energy particles were well measured by the calorimetric system (see sections 2.4 and 2.6).

Particle identification was needed in a wide momentum range to achieve the physics goals. In Neutral Current (NC) DIS events the scattered lepton has to be identified and measured with high precision and the identification of electrons, positrons and muons is also needed in order to study the semi-leptonic decay of heavy quarks and exotic processes involving leptons.

In Charged Current (CC) DIS processes a hermetic detector is needed in order to reconstruct the missing transverse momentum carried by the outgoing neutrino. In these kinds of events, and also in untagged photoproduction events, the precise reconstruction of the final state was important in order to determine the event kinematics.

The ZEUS coordinate system is a right-handed, cartesian system with the origin defined as the nominal Interaction Point (IP) ¹. The positive z -axis points in the direction of the proton beam and is often referred to as the “forward” region. The x -axis points from the IP towards the centre of HERA ring and the y -axis lies at 90° to the other two axes and points approximately vertically upwards. Since the proton-beam axis has a slight tilt, the y -axis does not precisely coincide with the vertical. The actual IP varies from event to event, and the average proton tilt varies on a fill-by-fill basis (see section 3.4.2).

¹ $x = y = 0$, defined in ZEUS by the geometrical centre of the central tracking detector, and $z = 0$ defines the nominal IP

Polar angles are defined with respect to the proton-beam direction in the forward region ($\theta = 0$) and the leptonic-beam is therefore at $\theta = \pi$. The azimuthal angles ϕ are measured with respect to the x -axis. The pseudorapidity variable is often used in event analysis; this quantity is an approximation at high energies of the particle rapidity given by $y = \log \frac{E+P_z}{E-P_z}$, and is defined by $\eta = -\log(\tan \frac{\theta}{2})$, where θ is the polar angle. The ZEUS coordinate system is illustrated in Fig. 2.5.

A brief outline of the various detector components is given below and a

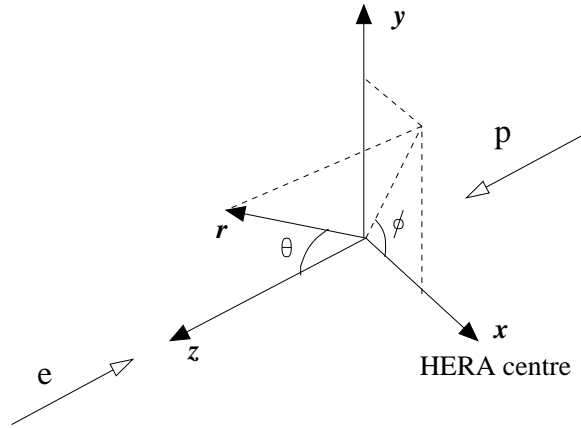


Figure 2.5: ZEUS coordinate system.

more detailed description of the sub-detectors relevant to the present analysis will be given later in this chapter. The two projection views of the detector in the $z - y$ and $x - y$ planes (Figs. 2.6 and 2.7) help to understand how the different components are placed in the different angular regions. At the centre of ZEUS, surrounding the beam pipe, lies the inner charged particle tracking detectors. The main tracking device is the CTD (Central Tracking Detector) placed in a solenoidal magnetic field ($B=1.43$ T) generated by a thin superconducting solenoid. In 2001, a silicon-strip Micro Vertex Detector (MVD) replaced the Vertex Detector (VXD) which was part of the initial configuration and removed during the 1995-1996 shutdown.

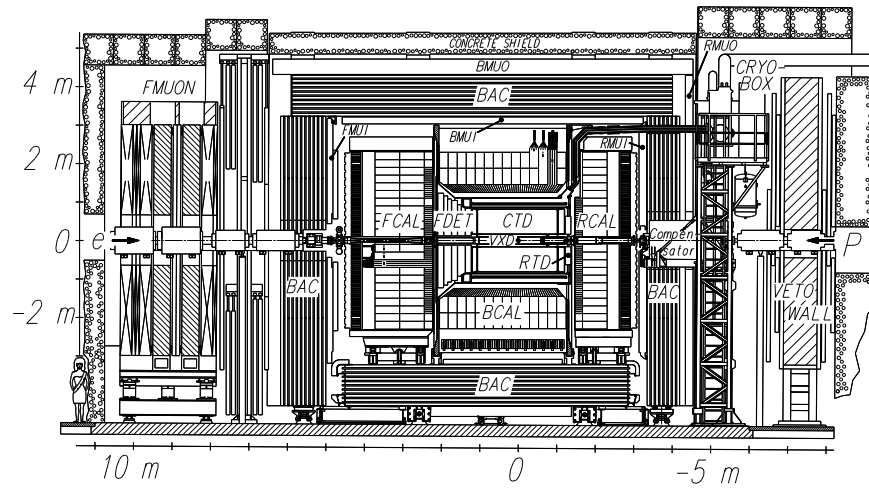


Figure 2.6: ZEUS longitudinal section ($z - y$).

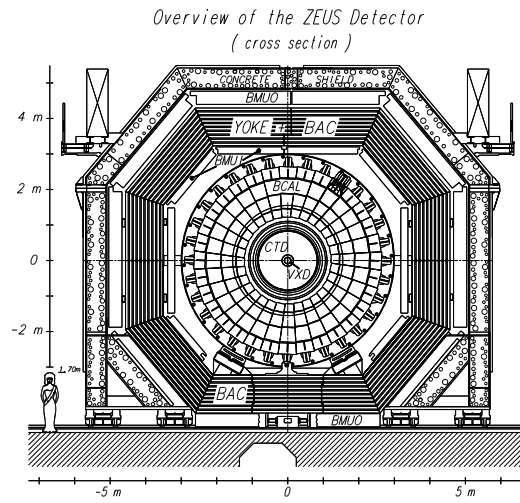


Figure 2.7: ZEUS transversal section ($x - y$).

The CTD was supplemented in the forward direction by three sets of planar drift chambers (FTD) with interleaved Transition Radiation Detectors (TRD) (labelled FDET in Fig. 2.8). In 2001 the TRD system was replaced

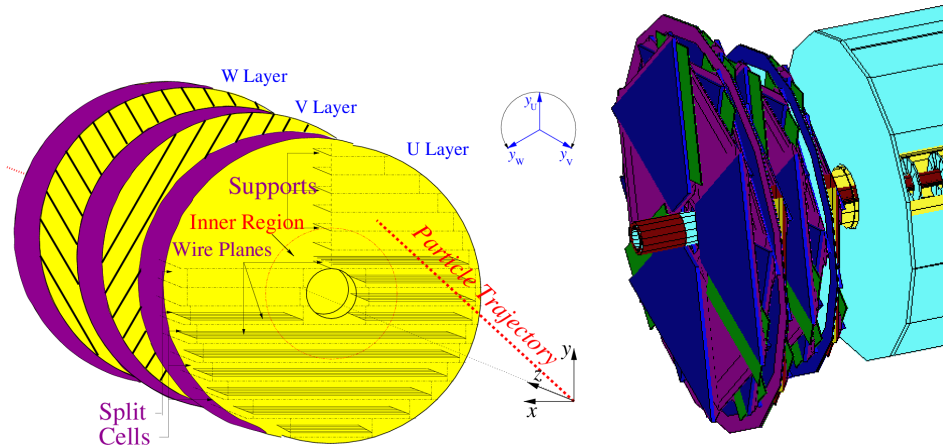


Figure 2.8: Planar drift chambers (left) and straw tubes (right) constituting the Forward Tracking Detector (FDET).

by a Straw Tube Tracker (STT) consisting of two modules built of straw tube layers filling the gaps between the three FTD chambers. The rear direction was supplemented by one planar drift chamber consisting of three layers (RTD). Although technically part of the calorimeter, the Small Rear Tracking Detector (SRTD) provided improved position resolution for particles and was particularly useful for the identification of the scattered lepton in the rear direction not intercepted by the rear part of the calorimeter. Together, the tracking detectors offered an angular acceptance of $10^\circ < \theta < 160^\circ$ for charged particles. The tracking system was surrounded by a compensating high-resolution uranium-scintillator sampling calorimeter (UCAL, see section 2.6) which was used as the main device for energy measurements; it was divided into three sections: the Forward (FCAL), Barrel (BCAL) and Rear (RCAL) CALorimeters. The iron yoke, which provided the return path for the solenoidal magnetic field flux, was equipped with a set of proportional

tubes and served as a calorimeter (BAC) for the detection of shower tails not completely “contained” by UCAL; this device acted also as a tracking device for muon detection.

Dedicated muon detectors (see section 2.7) were located inside (FMUI, BMUI and RMUI) and outside the iron yoke (FMUO, BMUO and RMUO); for the inner muon chambers the iron of the yoke is magnetized with a toroidal field (with strength $B \simeq 1.7$ T) in order to analyse the muon momentum.

Other detectors were located several metres away from the main detector along the beam pipe.

The VETO wall was located in the rear direction at about $z=-7.5$ m from the interaction point. It consisted of an iron wall supporting scintillator hodoscopes and was used to reject background from beam gas interactions.

The LUMI detector (see section 2.8) was made of two small lead-scintillators calorimeters at $z = -35$ m and $z = -(104 - 107)$ m and detected electrons and photons from bremsstrahlung events for the luminosity measurement. The 6m Tagger was a small scintillating fiber/tungsten calorimeter located close to the beamline at $z = -5.37$ m. Its prime purpose was to tag quasi-real electrons from photoproduction events and to assist the acceptance determination for the lumi system. During the last period, the tagger has received a lot of attention because of its role in the measurement of F_L and the total photoproduction cross section.

2.4 The Central Tracking Detector (CTD)

The Central Tracking Detector (CTD) [29] was a cylindrical wire drift chamber used to measure the direction and momentum of the charged particles and to estimate the energy loss dE/dx which provided information for particle identification 2.10. The inner radius of the chamber was 18.2 cm, the outer was 79.4 cm, and its active region covered the longitudinal interval from $z=-100$ cm and $z=104$ cm, resulting in a polar angle coverage of $15^\circ < \theta < 164^\circ$. The chamber was flushed, close to atmospheric pressure,

with a gas mixture of argon (Ar), carbon dioxide (CO_2) and ethane (C_2H_6) in the proportion 90:8:2. An alcohol/ H_2O mixture (77 /23 %) was injected into the gas.

The CTD consisted of 72 radial layers of sense wires, divided in groups of eight groups of nine *superlayers* (SL). A group of eight radial sense wires with associated field wires in one superlayer made up a *cell*. The sense wires were $30\ \mu\text{m}$ thick while the field wires had differing diameters. A total of 4608 sense wires and 19584 field wires were contained in the CTD.

The CTD was designed to operate in a magnetic field to allow the momentum measurement of charged particles. The field wires were tilted at 45° with respect to the radial direction in order to obtain a radial drift under the influence of the electric and magnetic fields. One octant of the CTD is shown in Fig. 2.9.

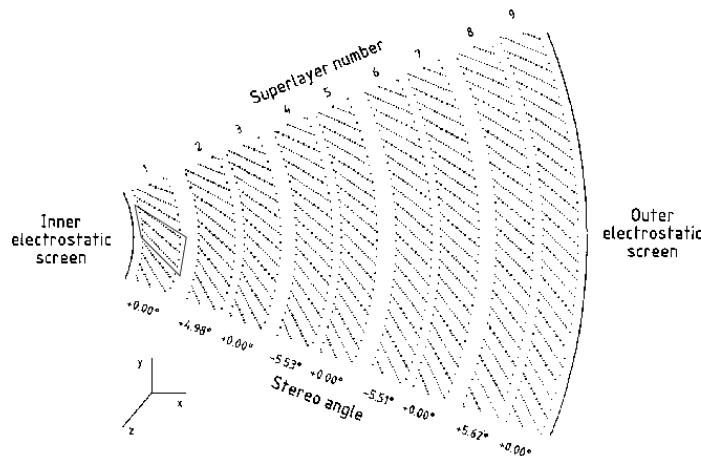


Figure 2.9: *Transverse cross section of one octant of the CTD. The sense wires are indicated with dots.*

A charged particle traversing the CTD produced ionization of the gas in the chamber. Electrons from the ionization drifted towards the positive sense wires, while the positive ions were repelled and drifted towards the negative

field wires. The drift velocity of the electrons was approximately constant and equal to $50 \mu\text{m}/\text{ns}$. An avalanche effect occurred close to the wire giving an amplification factor on the electrons of $\sim 10^4$ so that a measurable pulse was induced on the sense wires.

The superlayers were numbered 1 to 9 from the innermost to the outermost SL. Odd-numbered (axial) SLs had wires parallel to the z direction, while wires in even-numbered (stereo) SLs were at a small stereo angle of $\pm 5^\circ$ to measure the z coordinate. The achieved resolution is $\sim 100 - 120 \mu\text{m}$ in the $r - \phi$ plane and 1.4 mm in the z coordinate.

The three inner axial superlayers (SL1, SL3, SL5) were additionally instrumented with the z -by-timing system. This estimated the z -position of a hit by measuring the difference in arrival time of the pulses on the sense wires at each end of the detector. Although the resolution achieved ($\sim 3\text{cm}$) was much cruder than that obtained using the full axial and stereo wire information, it was a relatively fast method and used predominantly for trigger and track seed-finding.

As mentioned before, the CTD was contained within a superconducting solenoid which provided a magnetic field of 1.43 T. This field caused charged particles to travel in a circular path of radius, R , given by:

$$R = P_T/QB \quad (\text{S.I. units}) \quad (2.2)$$

where Q was the charge of the particle (Coulombs), B the strength of the magnetic field (Tesla) and P_T was the transverse momentum (kg m s^{-1}). This allowed an accurate determination of the P_T of the charged particle.

Since the installation of the MVD in 2001, the resolution has changed. It was expected that the influence from multiple scattering was larger (more material) but that the hit resolution was better compared to the resolution quoted above due to the inclusion of MVD hits. Latest results including the MVD in the global track reconstruction indicated the momentum resolution was [30]:

$$\sigma(P_T)/P_T = 0.0026P_T \oplus 0.0104 \oplus 0.0019/P_T. \quad (2.3)$$

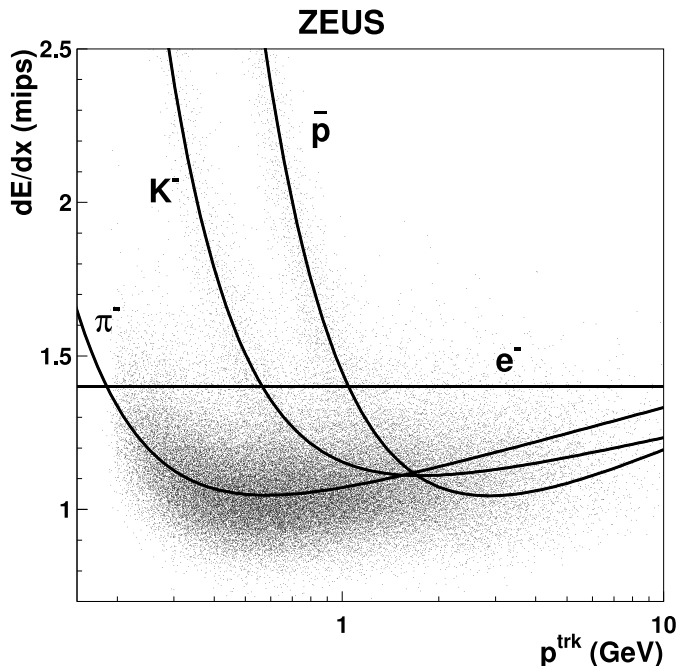


Figure 2.10: The energy loss for different particles, measured by the CTD, as a function of the particle momentum [?].

2.5 The ZEUS Microvertex Detector (MVD)

During the 2000-2001 shutdown, planned for the luminosity upgrade, a silicon microvertex detector (MVD) was installed in ZEUS. The MVD, placed between the beam pipe and the inner volume of the CTD, provides an improvement in the global precision of the tracking system and allows the identification of events with secondary vertices originating from the decay of particles with long lifetime ($c\tau \gtrsim 100\mu m$). This device helps the study of hadron decays containing heavy quarks such as charm and beauty, or tau leptons thanks to an improvement in the track resolution with the possibility to resolve secondary vertices. The technical requirements which were taken into account during the design of the MVD are:

- angular coverage around the interaction point between $10^\circ < \theta < 160^\circ$;

- measurement of three points for each track in two independent projections;
- $20 \mu m$ intrinsic hit resolution;
- separation of two tracks up to $200 \mu m$;

The main limitations are due to the small amount of space available between the CTD (radius=18.2 cm, see Section 2.4) and the beam pipe. The following description summarizes the main characteristics of the MVD, in its two components covering the central (BMVD) and forward (FMVD) region (see Fig. 2.11).

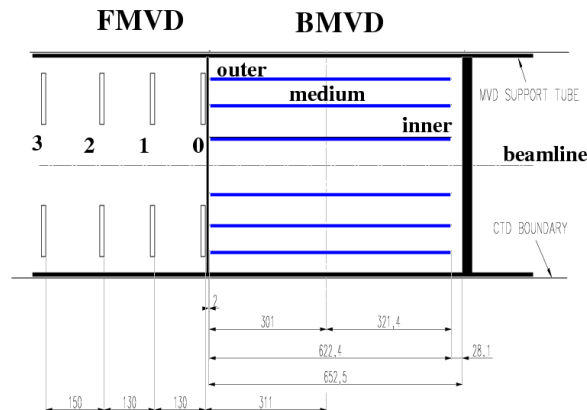


Figure 2.11: *Longitudinal MVD section. There are 3 layers in the barrel region and 4 wheels in the forward section.*

2.5.1 Barrel and forward micro vertex detector

The barrel section of the MVD is 64 cm long (see Fig. 2.11) and is sub-structured in three layers to allow high efficiency in the pattern recognition and to make an estimate of the track momentum in the trigger phase.

The first layer of silicon detectors follows the elliptical path around and along the beam pipe and it is placed at a variable radius between 3 and 5 cm from

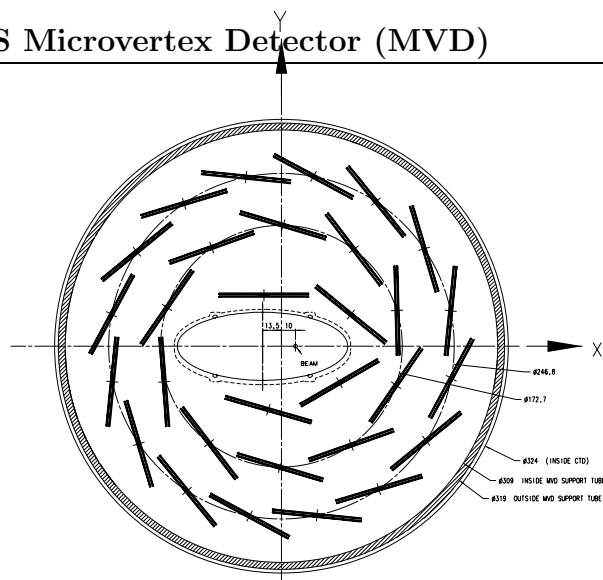


Figure 2.12: *BMVD section: 3 superlayers around beam pipe are shown.*

the CTD axis (see Fig. 2.12). The beam pipe is not centred with respect to the CTD axis and the nominal interaction point is shifted towards the centre of HERA (along the x axis) by about 4 mm in order to accommodate the primary synchrotron radiation spread inside the beam-pipe volume. The second and third layer are placed along a circular path at $r \sim 8.6$ cm and $r \sim 12.3$ cm. On average a track crosses 2.8 layers. The resolution on the impact parameter, based on Monte Carlo studies, is $\sim 100\mu\text{m}$. It is defined for tracks perpendicular to the beam pipe ($\eta = 0$) which cross all three layers and is a function of track momentum.

The BMVD is equipped with 600 silicon strips sensors mounted on 30 carbon fibre structures called *ladders* (Fig. 2.13); two layers of sensors are placed parallel and perpendicular to the beam line in order to measure $r - \phi$ and $r - z$ coordinates. Each layer is made of two single-sided silicon strip planes ($320\mu\text{m}$ thickness) with p^+ strips implanted in a n -type bulk. The strip pitch is $20\mu\text{m}$; every 6th strip has an AC coupling with a read out line made by an aluminium strip through a dielectric material ($\text{SiO}_2 - \text{SiN}_4$). Two sensors are glued together, electrically connected with a copper path excavated in a Upilex foil of $50\mu\text{m}$ of thickness (see fig. 2.13). From the figure it

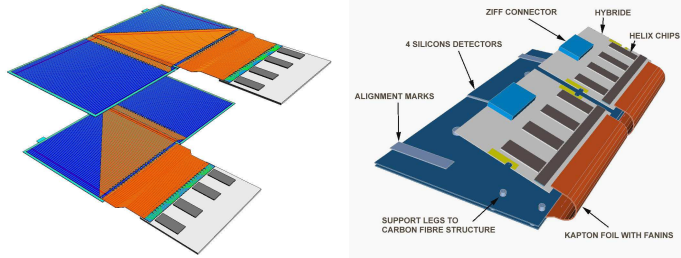


Figure 2.13: *Half modules and ladders mounted on the support.*

can be seen that the sensor is connected to the readout device; the resulting surface covered by the two sensors and by the readout system is called a “half-module” and is $6.15 \text{ cm} \times 6.15 \text{ cm}$.

The FMVD consists of 4 planes called *wheels*, each of them is made of two layers of 14 silicon sensors with the same technical characteristics of the barrel sensors but with a trapezoidal shape (Fig. 2.14). This device allows

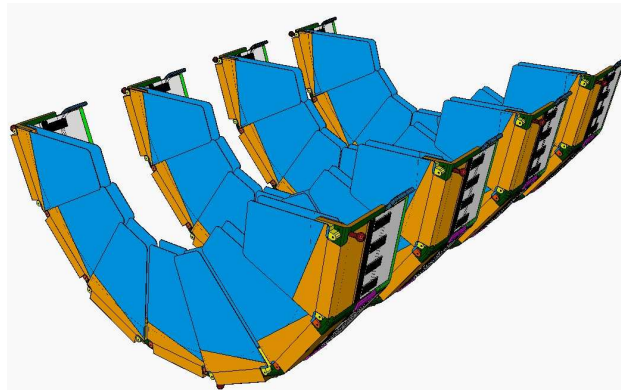


Figure 2.14: *FMVD 4 wheels.*

to extend the acceptance in pseudorapidity up to $\eta = 2.6$, a region where tracking information has yet to be used in ZEUS. Each wheel has inner and outer sensors. They are mounted back to back. An inner and outer wheel sensor form a sector. The crossing angle between the strips in the inner and outer sensor is $\sim 13^\circ$ ($180^\circ/14$). Inside a layer of sensors the adjacent

sensors are slightly overlapped in order to minimize the dead regions. The four wheels are positioned at $z=32, 45, 47$ and 75 cm; the first wheel is linked to the structure supporting the BMVD. A more detailed description can be found in [31].

2.6 The Uranium-scintillator Calorimeter (UCAL)

The ZEUS calorimeter (UCAL) [32] was a high-resolution compensating calorimeter. It completely surrounded the tracking devices and the solenoid, and covered 99.7% of the 4π solid angle. It consisted of 3.3 mm thick depleted uranium plates (98.1% U^{238} , 1.7 % Nb, 0.2 % U^{235}) as absorbers alternated with 2.6 mm thick organic scintillators (SCSN-38 polystyrene) as active material.

The hadronic showers contained both hadronic and electromagnetic components whose proportions could fluctuate enormously. In order to take into account this phenomenon and therefore optimize the energy detection of both shower components, the uranium calorimeter was designed to be *compensating*, so as to obtain the same mean detector response from hadronic and electromagnetic showers of the same energy ($e/h=1$). Therefore the UCAL had different layers of depleted uranium and scintillator with thickness of 3.3 mm and 2.6 mm . Under test beam conditions [33], the electromagnetic energy resolution achieved was:

$$\frac{\sigma_E}{E} = \frac{18\%}{\sqrt{E}} \oplus 2\% \quad (2.4)$$

whilst the hadronic resolution is:

$$\frac{\sigma_E}{E} = \frac{35\%}{\sqrt{E}} \oplus 1\% \quad (2.5)$$

where E is the particle energy measured in GeV.

The UCAL is divided into three regions: the forward (FCAL), barrel (BCAL) and rear (RCAL) calorimeter. Since most of the final state particles in a

lepton-proton interaction at HERA are boosted to the forward (proton) direction, the three parts are of different thickness, the thickest being the FCAL ($\sim 7\lambda$), then the BCAL ($\sim 5\lambda$) and finally the RCAL ($\sim 4\lambda$), where λ is the interaction length.

Each part of the calorimeter is divided into *modules*. The 23 FCAL modules and the 23 RCAL modules are rectangular, whereas the 32 BCAL modules which surround the cylindrical CTD are wedge-shaped covering 11.25° in azimuth. Each module consists of so called *towers* of 20×20 cm which are subdivided longitudinally into one electromagnetic (EMC) and two (one in RCAL) hadronic (HAC) sections. The EMC sections are further transversely divided into four cells (only two in RCAL).

The FCAL EMC section per tower consists of the first 25 uranium-scintillator layers and has a depth of $25 X_0$, where X_0 is the radiation length. Each of the two HAC sections per FCAL tower is 3.1λ deep and consists of 160 uranium-scintillator layers.

The BCAL EMC section is made of the first 21 uranium-scintillator layers, the two HAC sections of 98 layers. The resulting depth is $21 X_0$ for the electromagnetic section and 2.0λ for each hadronic section.

The RCAL towers consist of one EMC and only one HAC section. Therefore its depth is $26 X_0$ for the EMC part and 3.1λ for the HAC part.

Light produced in the scintillators is read out by 2 mm thick wavelength shifter (WLS) bars at both sides of the module, and brought to one of the 11386 photomultiplier tubes (PMT) where it is converted into an electrical signal. The summed information per cell is used for energy and time measurements. The UCAL provides accurate timing information, with a resolution of the order of 1 ns for particles with an energy deposit greater than 1 GeV. This information can be used to determine the timing of the particle with respect to the bunch-crossing time, and it is very useful for trigger purposes in order to reject background events, as will be illustrated later in the trigger section.

Calibration of the PMTs and the electronics is mainly performed using the natural radioactivity of the depleted uranium which produces a constant signal in the PMTs. The signal can be used to intercalibrate geometrically identical regions and to transport the absolute calibration scale determined in test beam measurement. In addition, laser, LED and test pulses are also used for the calibration. The achieved uniformity of calibration is better than 1%.

The Presampler [34] was a thin scintillator layer placed on the inner side of the forward and rear calorimeter (FCAL and RCAL) and was used to cover the forward and rear regions which could not be covered by the barrel section. It was used to estimate the shower dimensions and hence the energy loss in the passive material before entering the calorimeter.

2.7 The muon detectors

These detectors are specifically designed to measure penetrating tracks coming from the interaction region (*pointing tracks*) which can cross the whole calorimeter and the iron yoke. These tracks are identified mainly with muons which can traverse large amounts of material without being absorbed.

The momenta of muons can be very different, depending on their polar angle due to the boost in the forward direction. Muons with more than 10 GeV momentum are frequently produced in the forward region. In the barrel and rear regions, the average momentum of the muons is expected to be much lower. Therefore the muon detection system is split into two subdetectors, the Forward Muon Detector (FMUON) and the barrel and rear muon detectors (BMUON and RMUON respectively).

2.7.1 The Forward MUON detector (FMUON)

The muon detection in the forward region was important for HERA because important physical phenomena, like heavy quark or leptoquark production,

produced leptons with small decay angles. Since the resolution and the acceptance of tracking detectors placed inside the calorimeter decreased at low angles, the FMUON was used to measure momenta up to 100 GeV with a resolution of 25% in the forward region independently of the inner region detectors. This detector was equipped with a trigger system which applied a momentum cut and required a candidate track originating from the interaction point.

The FMUON consisted of:

- a system of four limited streamer tube trigger planes (LT1 - LT4) [35], with digital ρ ² and ϕ readout;
- two planes of limited streamer tubes with digital (ρ, ϕ) and analog ρ readout, in the large polar angle region (LW1 and LW2);
- four planes of drift chambers (DC1 - DC4) for the measurement of pseudo ρ [36];
- two large toroidal iron magnets providing a magnetic field of 1.7 T for the momentum separation and measurement in the angular region $5^\circ < \theta < 16^\circ$.

The first limited streamer tube plane and the first drift chamber make up the FMUI detector, while the FMUO detector consists of the rest of the system (Fig. 2.15).

The Limited Streamer Tubes (LST) Planes

The aim of the limited streamer tubes (LST) is to trigger on muon candidates and to reconstruct their position in terms of the azimuthal and radial coordinates of the track. A trigger plane is made of four LST chambers, grouped in pairs in two half-planes. A quadrant consists of two layers of LST positioned

²The ρ coordinate defines the direction perpendicular to the beam line.

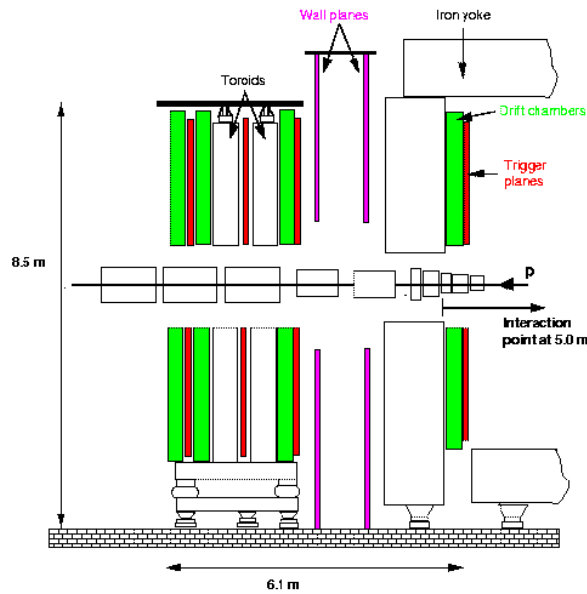


Figure 2.15: FMUON longitudinal section.

horizontally inside a plastic sheet. The tubes of the two planes are slightly displaced (0.5 cm) in order to achieve a complete geometrical acceptance. Each quadrant is contained in an aluminium air tight box. On the outer side, copper strips are glued in polar geometry. The LSTs induce a signal in the copper strips if a particle crosses the plane. There are 132 radial ρ strips each 1.9 cm wide. They are divided along the bisector of the quadrant so that the simplest unit of the trigger plane to be read out is the octant. The number of ϕ strips is 32 per octant and each strip covers an interval of 1.4° in the azimuthal angle.

The Drift Chambers (DC)

The drift chambers are needed in order to obtain a good momentum resolution. Each plane consists of 8 chambers, grouped in two half planes, fixed on a support panel. The basic constituent of the chamber is the *cell*, made of four sense wires and of the layers needed to generate the appropriate electric

field. The signals of the four sense wires are sent to a TDC, which convert them into a time distance, connected to the space distance by a known relation.

The Large Angle Coverage Planes (Limited Streamer Wall, LW)

The two large angle coverage planes (LW) are needed in order to achieve the desired geometrical acceptance also in the region left uncovered by the toroids ($16^\circ < \theta < 32^\circ$). Each plane consists of eight steel tight wrappings that contain a LST layer. The LST signal is induced on copper strips with a radial geometry, spaced at 0.7° in the ϕ coordinate and at 1.8 cm in the ρ coordinate. There are 64 ϕ strips per octant and 192 ρ strips per octant. The achieved resolution in the ρ coordinate, using a charge barycentre method, is ~ 1 mm.

2.7.2 The Barrel and Rear MUON detector (B/RMUON)

The barrel and rear muon detector [37] covers a very large area (~ 2000 m²) and consists of LST *chambers* as the basic structure. The chambers covering the inner barrel part between the CAL and the iron yoke are called BMUI while the chambers situated outside the yoke are denoted as BMUON. The rear region is divided into RMUI and RMUO chambers in a similar way (see Fig. 2.16).

The chambers have different shapes and dimensions depending on their location, but their nominal structure is the same. The supporting structure of each chamber is an aluminium honeycomb frame 20 cm thick in the rear chambers and 40 cm in the barrel. Two plates of LST are placed on both sides of the honeycomb. The two layers on the same side of the chamber are displaced by 8.3 mm in order to minimize dead areas for particles traversing at 90° with respect to the wire plane. Each LST is made of a plastic sheet with eight cells. Each cell contains a copper-beryllium wire of 100 μ m diameter, the distance between two sense wires being 1 cm.

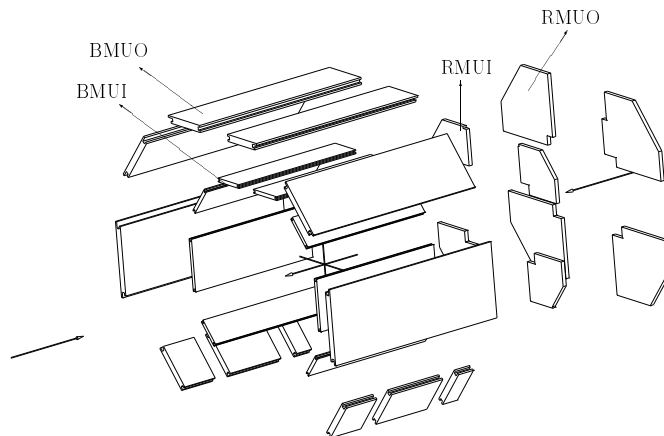


Figure 2.16: Layout of the barrel and rear muon detector.

Each LST plane is equipped on one side by 13 mm wide readout strips with 15 mm pitch that run orthogonal to the wires. In the BMUI and BMUO chambers the LSTs are parallel to the beam direction while in RMUI and RMUO they are horizontal (parallel to the x -axis). With the analog strip readout the achievable spatial resolution on the coordinate orthogonal to the wires is $200\ \mu\text{m}$ while it is $700\ \mu\text{m}$ for the coordinate parallel to the wires.

2.7.3 The Backing Calorimeter (BAC)

The Backing Calorimeter (BAC) [39] used the return iron yoke as an absorber to form an additional tracking calorimeter using aluminium proportional tubes operating in an $\text{Ar} - \text{CO}_2$ atmosphere. The BAC measured showers leaking out of the CAL allowing the selection of event samples with a resolution corresponding to the intrinsic resolution of the CAL. It could distinguish between hadron showers and muons and provided muon identification and trigger capabilities in the bottom yoke and other areas where no muon chambers were present.

The BAC was built from modules inserted into the yoke (see Fig. 2.6) consisting of 7-8 proportional tubes of a cross section of $11 \times 15\ \text{mm}$ and a length

between 1.8 and 7.3 m. Modules are equipped with 50 cm long aluminium cathode square pads in addition to the gold plated tungsten wires of 50 μm diameter. The wires are parallel to z in barrel (providing ϕ) and parallel to x in Forward/Rear zone (providing y). The wires were read out were on one side and provided both analogue and digital signals whereas the pads had only an analogue read-out.

Energy was measured by summing up the analogue signals in towers of a width of 25 -50 cm (2-4 modules) over the full depth of the BAC. The pads of 2-4 neighbouring modules were added up to pad towers with an area of $50 \times 50 \text{ cm}^2$ (4 modules) similar to the wire towers. They provided also patterns of hit positions in the BAC to reconstruct muon trajectories.

The spatial resolution of the BAC was ~ 1 mm perpendicular to the wires, whereas the resolution parallel to the wires was defined mainly by the pad size. The energy resolution determined by test beam measurements was:

$$\frac{\sigma_E}{E} = \frac{1.1}{\sqrt{E}} \quad (2.6)$$

where E was the particle energy in GeV.

2.8 The luminosity measurement

The luminosity measurement at ZEUS is done by studying the production rate of photons through the Bethe-Heitler process [?]:

$$e + p \rightarrow e' + p + \gamma, \quad (2.7)$$

where the photon is emitted from the electron at very small angles with respect to the ingoing lepton direction (negative z). The cross section for this process at the leading order (LO) is expressed as:

$$\frac{d\sigma}{dk} = 4\alpha_e r_e^2 \frac{E'}{kE} \left(\frac{E}{E'} + \frac{E'}{E} - \frac{2}{3} \right) \left(\ln \frac{4E_p E E'}{M m k} - \frac{1}{2} \right) \quad (2.8)$$

where E and E_p are the energies of the lepton and proton beams respectively, E' is the outgoing electron energy, k is the photon energy, M and m are the

proton and electron masses while r_e^2 represents the classical electron radius. Higher-order corrections in the above cross section calculation are less than 0.5%.

The luminosity monitor consists of a photon and a lepton calorimeter [?], located along the beam pipe at $z = -(104 - 107)$ m and $z = -35$ m, respectively (Fig. 2.17)

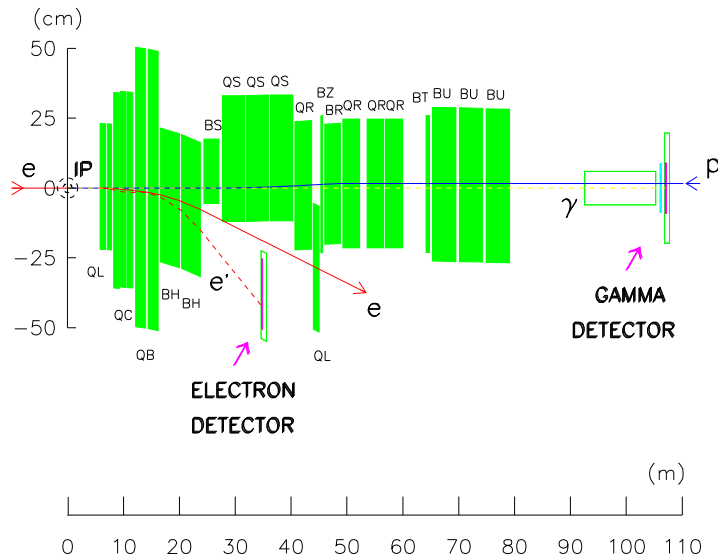


Figure 2.17: The layout of the ZEUS Luminosity Monitor. The nominal interaction point is located at $(0,0)$.

To protect the photon calorimeter against synchrotron radiation, it has been shielded by a carbon-lead filter. The resulting calorimeter resolution, (with E in GeV), is:

$$\frac{\sigma_E}{E} = \frac{0.25}{\sqrt{E}}. \quad (2.9)$$

The bremsstrahlung event rate is determined by counting the number of photons above a fixed energy threshold, and not by the simultaneous identification of the lepton and the photon, because of the dependence of the lepton

calorimeter acceptance on the beam position and angle. The luminosity is then extracted using:

$$L = \frac{R_{ep}(E_\gamma > E_\gamma^{th})}{\sigma_{ep}^{acc}(E_\gamma > E_\gamma^{th})}, \quad (2.10)$$

where $\sigma_{ep}^{acc}(E_\gamma > E_\gamma^{th})$ is the cross section corrected for the detector acceptance, $R_{ep}(E_\gamma > E_\gamma^{th})$ is the photon rate and E_γ^{th} is the photon threshold.

2.9 Background

The background event rate at ZEUS could be much higher than the ep interaction rate, depending on the beam-pipe vacuum conditions. The main background sources which had to be removed were:

- interactions inside the beam pipe: beam particles interact with the residual gas inside the beam pipe or off-momentum beam particles interact against the beam pipe walls. If this interaction happens near the detector, the interaction products can be detected by ZEUS.
- halo muons: the hadronic interactions of the beam protons can subsequently produce muons through pion or kaon decays; these muons go into the halo beam and are therefore called *halo muons*.
- cosmic muons: these are muons coming from the cosmic showers generated in the atmosphere which can be detected by ZEUS.

The background is dramatically reduced by the trigger, which is tuned to discriminate against it. The background coming from the interaction of the particles with the beam gas is limited through the VETOWALL device, an iron wall 87 cm thick and $800 \times 907 \text{ cm}^2$ placed at $z = -7.5 \text{ m}$ from the interaction point. It is instrumented with two scintillator hodoscopes, one for each side of the wall, which can identify the beam-gas-interaction events. A $95 \times 95 \text{ cm}^2$ gap window is left uncovered around the beam-pipe.

The trigger system, described in the next chapter, takes into account the

information coming from the calorimeter, SRTD (a hodoscopic scintillator placed around the beam pipe in front of the RCAL), C5 (a HERA collimator equipped with scintillator counters placed behind the RCAL at 1.2 m from the nominal interaction point in the electron beam direction), CTD and muon detectors.

The timing difference between the FCAL and RCAL measurements can be used to reject the beam gas events, since the products from the beam gas interactions hit the RCAL ~ 10 ns before hitting the FCAL. The calorimeter temporal resolution, for energy E greater than few GeV, is better than 1 ns. The same method is used to tag the cosmic muons, studying the temporal difference between the upper and lower side of BCAL.

2.10 The ZEUS trigger system

The bunch crossing frequency at ZEUS was ~ 10 MHz, corresponding to a time gap of 96 ns between two consecutive collisions. The rate was dominated by the interaction of the proton beam with the residual gas which contributed about 10-100 kHz, depending upon the vacuum levels in the beam-pipe up to 100 m upstream of ZEUS. This frequency had to be reduced to a level compatible with the offline data storage without losing interesting physics events (few Hz).

The approach adopted for the ZEUS data acquisition was a three level trigger system with increasing complexity of the decision making algorithm and decreasing throughput rate (Fig. 2.18).

- *first level trigger (FLT)*; was a hardware based trigger which used programmable logic to make a quick rejection of background events. The FLT reduced the input rate of 100 kHz to an output rate of ~ 300 Hz. As it was not possible to take a decision within the bunch crossing time, the data were pipelined until the trigger decision was taken.

Individual component decisions used a subset of the total data, and were made within 1.0-2.5 μs . The global first level trigger (GFLT) calculations took up to 20 bunch crossings and the FLT delivered the abort/accept decision after 4.4 μs .

Typical criteria used by the FLT in taking the trigger decision were the approximate “crude” event vertex position and track multiplicities from CTD, the transverse energy of the event and energy sums in sections of the calorimeter, the timing vetoes from CAL,SRTD,C5 and the presence of muons. The FLT had a good efficiency for ep physics ($\sim 100\%$), but still had a very low purity ($\sim 1\%$).

- *second level trigger (SLT)*; the SLT was a parallel processor utilising a network of transputers. It reduced the FLT output rate of ~ 300 Hz to an output rate of $\lesssim 100$ Hz. As in the FLT, the outputs of the component SLT decisions were passed to the global SLT (GSLT) where the event decision was made. The GSLT made its decision after 5.2-6.8 ms. The decision is based upon limited charged particle tracking, vertex determination, calorimeter timing and $E - P_z$ and scattered electron tagging.

Data from an event accepted by the SLT trigger are sent directly from the component to the event builder (EVB). The EVB stores the data from the components until the third level trigger (TLT) is ready to process it, and combines the data from different components into one consistent record: the event. One event is stored in a single record of the ADAMO [?] database tables.

- *third level trigger (TLT)*; is a software trigger which is sent asynchronously with the bunch crossing on a dedicated PC farm. At this stage an approximate version of the event reconstruction software is run, including tracks and interaction vertex reconstruction. The TLT has been designed to cope with an input rate of 100 Hz from the SLT

at design luminosity. The output rate is reduced to about 5 Hz. After accepting an event, the TLT sends the data via optical link to the DESY computer centre, where the events are written onto disk to be available for further offline reconstruction and data analysis.

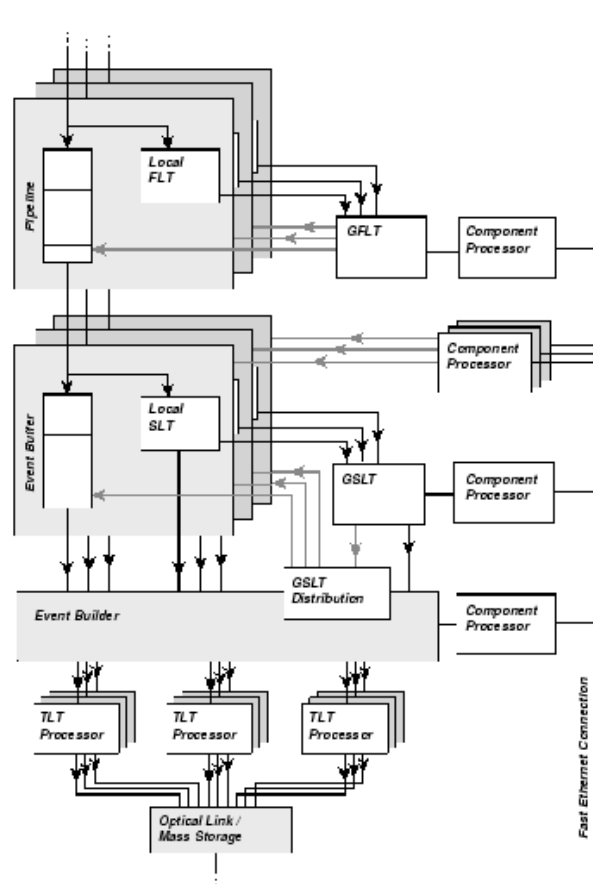


Figure 2.18: ZEUS trigger chain

Chapter 3

Events reconstruction

The aim of this analysis is the measurement of heavy flavor production in deep inelastic scattering using the semi-leptonic decay into muons. The reaction is

$$e p \rightarrow e Q \bar{Q} X \quad (3.1)$$

where at least one of the heavy quarks Q decays semi-leptonically by the reaction

$$Q(\bar{Q}) \rightarrow \mu^\pm \nu(\bar{\nu}) q \rightarrow \mu^\pm Jet. \quad (3.2)$$

Each event is therefore characterized by the presence of an electron scattered in the detector and of the decay products of the heavy quark, as well as the quark fragmentation products and proton remnant (see fig. 3.1). Semi-leptonic heavy flavour decays produce muons which are relatively close to the fragmented hadron. The muon identification requires dedicated algorithms which can cope with high track multiplicities around the muon track and can exploit the tracking capabilities of the muon detectors. The remaining products of the heavy quark fragmentation are reconstructed inclusively through the application of jet algorithms. We'll start the chapter describing first the reconstruction of the main variables for a DIS selection, kinematic variables, electron, hadronic system, jet, explaining meanwhile how the tracking and vertexing packages work; afterwards muon reconstruction will be described.

3.1 Reconstructon of the kinematic variables

The kinematic of a DIS event is defined by two independent variables once the energy of the incoming lepton E_e and proton E_p are known. The physical quantities measured in the detector are the energy and the polar angle of the scattered lepton (E'_e, θ_e) and the four-momentum of the particles belonging to the hadronic final state (E_h, px_h, py_h, pz_h). From the latter the hadronic system can be characterized by the scalar quantity δ_h , the total transverse momentum $p_{T,had}$ or the inclusive angle γ_{had}

$$\delta_{had} = \sum_{hadrons} (E_h - pz_h) \quad (3.3)$$

$$p_{T,had} = \sqrt{\left(\sum_{hadrons} px_h\right)^2 + \left(\sum_{hadrons} py_h\right)^2} \quad (3.4)$$

$$\gamma_{had} = 2 \arctan\left(\frac{\delta_{had}}{P_{T,had}}\right) \quad (3.5)$$

The quantity δ_{had} is by construction minimally affected by the losses of particles scattered outside the detector acceptance in the forward direction, which are produced by the fragmentation of the proton remnant. Those particles have generally high energies but small transverse momenta. On the contrary, $p_{T,had}$ is more sensitive to the losses in the forward direction. The inclusive angle γ_{had} is a function of $p_{T,had}$ in which these effects are reduced and the uncertainties on the energy scale are cancelled by the ratio. In conclusion, a sensible kinematic reconstruction can be obtained combining any pair of variables of the set $E_e, \theta_e, \delta_{had}, \gamma_{had}$.

3.1.1 Electron Method

This method was used in fixed target experiments and it is certainly the easiest one since it only requires the measurement of one particle. The kinematic variables are expressed in terms of the energy and polar angle of

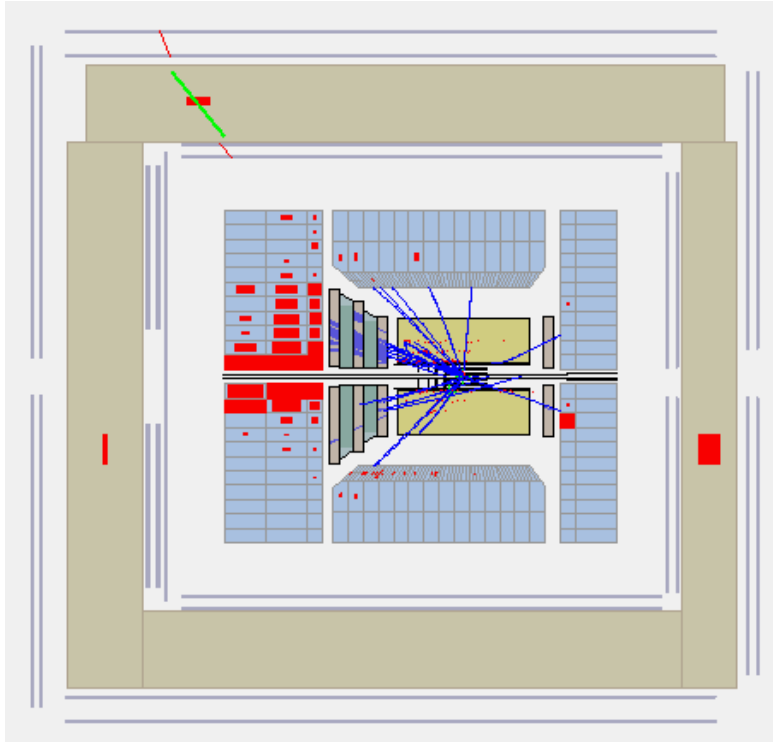


Figure 3.1: An event selected by this analysis. Cross section of the ZEUS detector across the zy plane showing the two jets, the scattered electron and the muon traversing the inner and outer muon chambers.

the scattered lepton measured in the calorimeter:

$$Q_e^2 = 2E_e E'_e (1 + \cos \theta_e) \quad (3.6)$$

$$y_e = 1 - \frac{E'_e}{2E_e} (1 - \cos \theta_e) \quad (3.7)$$

$$x_e = \frac{Q_e^2}{s y_e}. \quad (3.8)$$

where s is the squared center-of-mass energy (see Fig. 3.2). The method is precise at high y , but its resolution diverges towards $y_e \rightarrow 0$ due to the $1/y$

dependence in the error propagation formula of the relative error [42].

$$\frac{\delta y_e}{y_e} = \left(1 - \frac{1}{y_e}\right) \frac{\delta E'_e}{E'_e} \oplus \left(\frac{1}{y_e} - 1\right) \cot\left(\frac{\theta_e}{2}\right) \delta\theta_e \quad (3.9)$$

The electron angle can be measured with good precision taking advantage of the SRTD detector at low angles and of the tracking system at high angles, but the electron energy poses some problems due to the considerable amount of inactive material ($1 - 5X_0$) between the interaction region and parts of the calorimeter surface. This is illustrated in figure 3.2, where the reconstructed variables as a function of the generated one is illustrated for an inclusive DIS Ariadne MC sample.

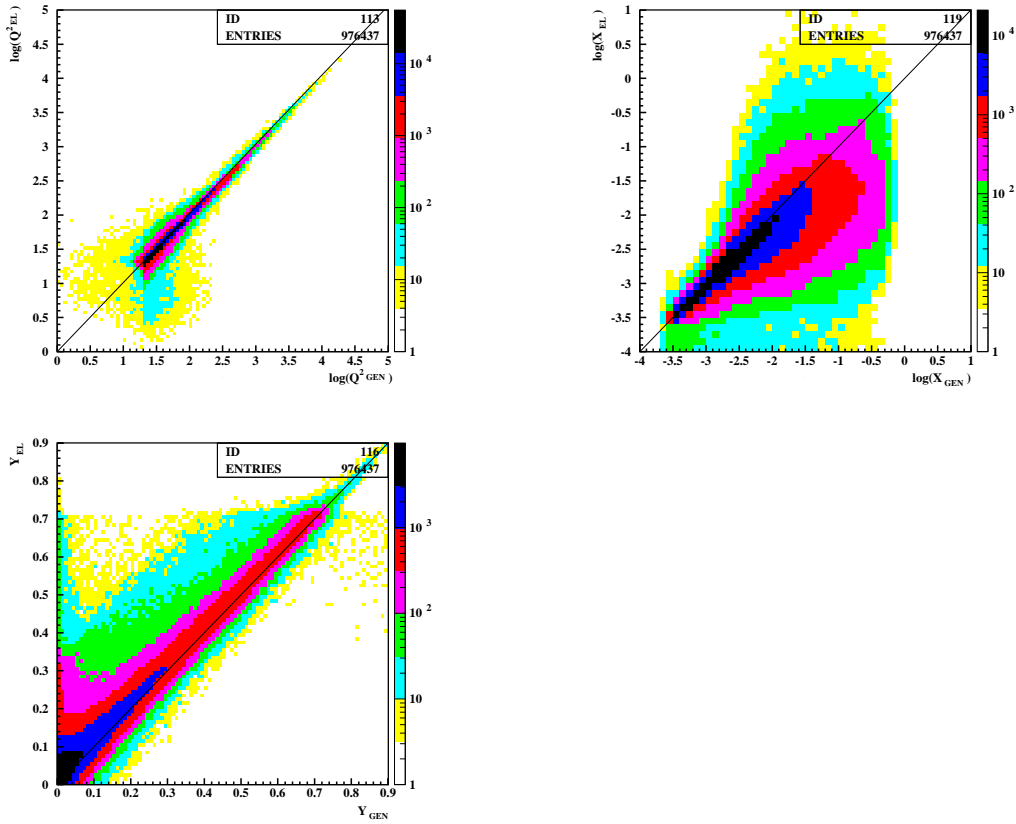


Figure 3.2: Two-dimensional plots of kinematic variables, Q^2 and x on the top, y below (reconstructed versus generated) for an inclusive MC sample using the Electron method.

3.1.2 Jacquet-Blondel method

The event kinematics can also be reconstructed using only the hadronic final state variables δ_{had} and $p_{T,had}$ [43]. It is applied in CC analysis and in photoproduction, when the interacting electron is absent or undetected being scattered at low angle down into the beam pipe (see Fig. 3.3).

$$y_{JB} = \frac{\delta_{had}}{2E_e} \quad (3.10)$$

$$Q_{JB}^2 = \frac{p_{T,had}^2}{1 - y_{JB}} \quad (3.11)$$

$$x_{JB} = \frac{Q^2}{s \cdot y_{JB}}. \quad (3.12)$$

This method can improve the y measurement based on the scattered lepton in the low y region since the relative error does not contain any term $\sim 1/y$

$$\frac{\delta y_{JB}}{y_{JB}} = \frac{\delta E_{JB}}{E_{JB}} \oplus \cot\left(\frac{\theta_{JB}}{2}\right) \delta\theta_{JB} \quad (3.13)$$

where

$$E_{JB} = \sum_{hadrons} E_h$$

and

$$\theta_{JB} = \gamma_{had}$$

3.1.3 Double angle method

This method relies on the electron polar angle θ_e and the angle γ_{had} of the hadronic system [44]

$$y_{\theta\gamma} = \frac{\sin\theta_e(1 - \cos\gamma_{had})}{\sin\gamma_{had} + \sin\theta_e - \sin(\theta_e + \gamma_{had})} \quad (3.14)$$

$$Q_{\theta\gamma}^2 = 4E_e^2 \frac{\sin\gamma_{had}(1 + \cos\theta_e)}{\sin\gamma_{had} + \sin\theta_e - \sin(\theta_e + \gamma_{had})} \quad (3.15)$$

$$x_{\theta\gamma} = \frac{E_e \sin\gamma_{had} + \sin\theta_e + \sin(\theta_e + \gamma_{had})}{E_p \sin\gamma_{had} + \sin\theta_e - \sin(\theta_e + \gamma_{had})} \quad (3.16)$$

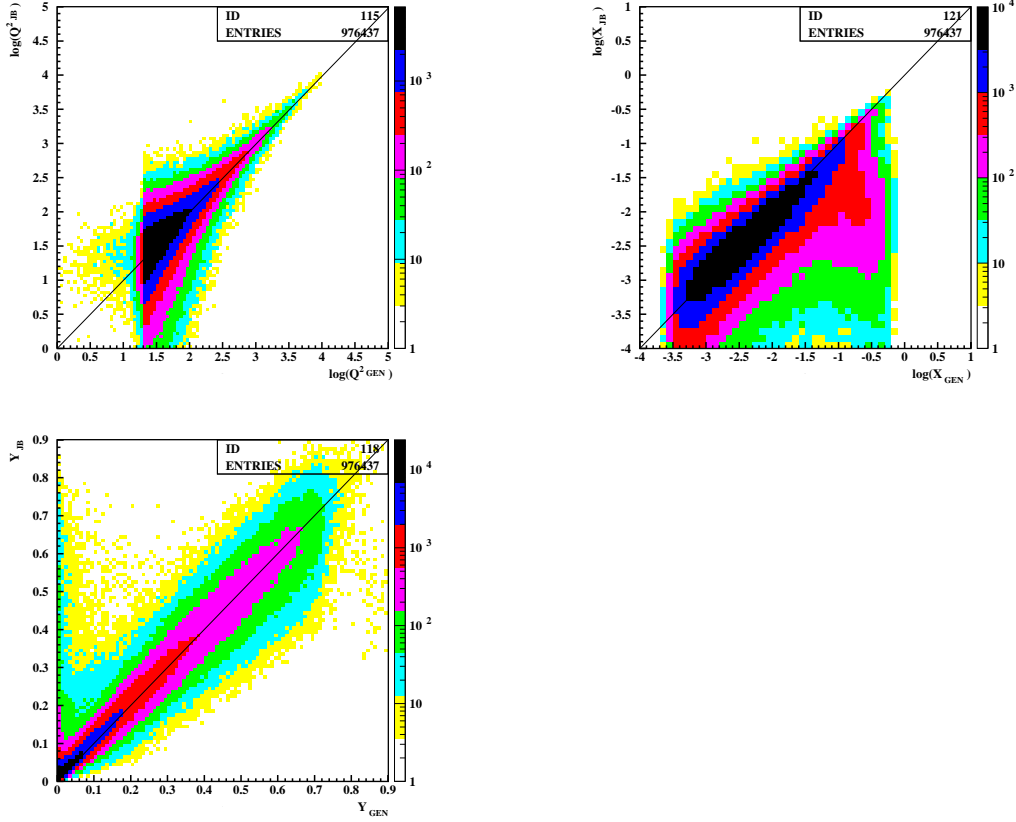


Figure 3.3: Two dimensional plots of kinematic variables, Q^2 and x on the top, y below (reconstructed versus generated) for an inclusive MC sample using Jacquet-Blondel method.

This reconstruction method does not require a precise knowledge of the energy scales and the corrections due to the photon radiation are small (see Fig.3.4). Nevertheless the resolution of all the variables depends strongly on the polar angle θ_e . Considering only the uncertainty due to the angular measurement we have:

$$\frac{\delta y_{\theta\gamma}}{y_{\theta\gamma}} \simeq -\frac{1 - y_{\theta\gamma}}{\sin \theta_e} \delta\theta_e ; \quad \frac{\delta Q^2_{\theta\gamma}}{Q^2_{\theta\gamma}} \simeq -\frac{2}{\sin \theta_e} \delta\theta_e ; \quad \frac{\delta x_{\theta\gamma}}{x_{\theta\gamma}} \simeq -\frac{1 + y_{\theta\gamma}}{\sin \theta_e} \delta\theta_e \quad (3.17)$$

Therefore, at low Q^2 , i.e. if θ_e is greater than about 175° the terms in Eqs. 3.17 dominate the total error and the electron or the Jacquet-Blondel methods give a more precise reconstruction [45].

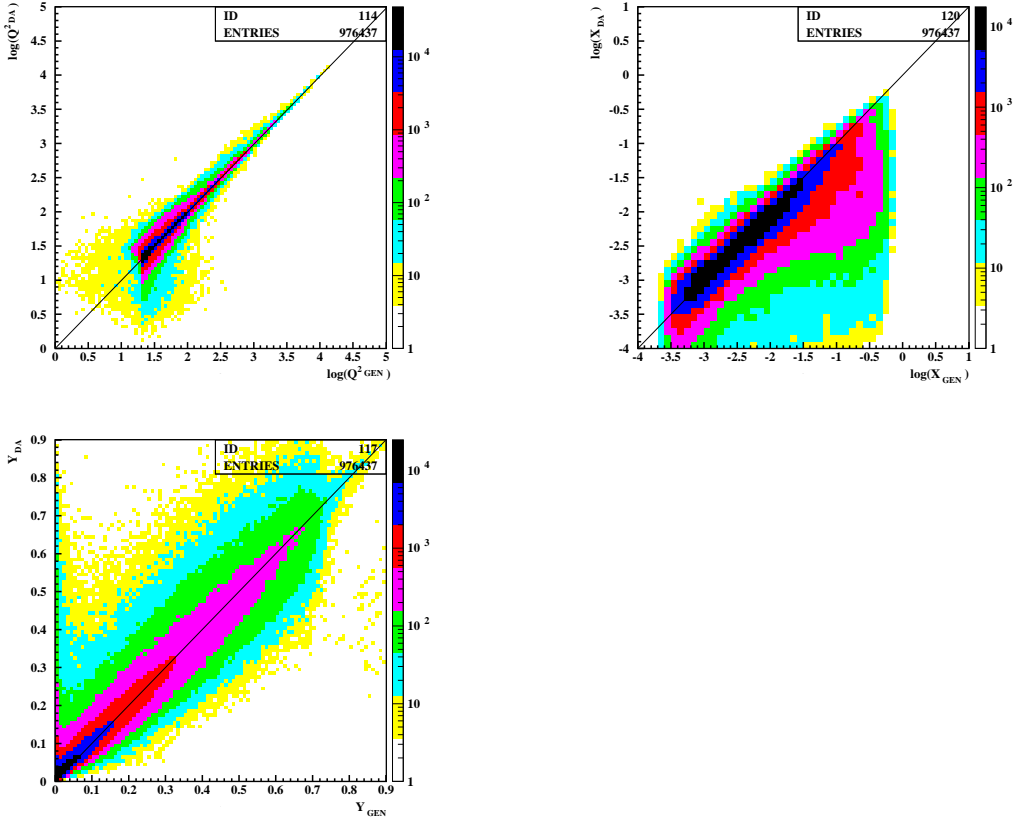


Figure 3.4: Scatter plots of kinematic variables, Q^2 and x on the top, y below (reconstructed versus generated) for an inclusive MC sample using Double Angle method.

3.1.4 The Σ method

The Σ method allows the determination of y and Q^2 independently of initial state photon radiation by using the y_e expression (eq. 3.7) but replacing the incident electron energy E_e with the reconstructed one [46] (see Fig. 3.5). The kinematic variables are given by the expressions

$$y_{\Sigma} = \frac{\delta_{had}}{\delta_{had} + E'_e(1 - \cos \theta_e)} \quad (3.18)$$

$$Q_{\Sigma}^2 = \frac{(E_e \sin \theta_e)^2}{1 - y_{\Sigma}} \quad (3.19)$$

$$x_{\Sigma} = \frac{Q_{\Sigma}^2}{s \cdot y_{\Sigma}}. \quad (3.20)$$

The error propagation on y_Σ gives:

$$\frac{\delta y_\Sigma}{y_\Sigma} = (1 - y) \left(\frac{\delta(\delta_{had})}{\delta_{had}} \oplus \frac{\delta E_e}{E_e} \oplus \frac{\delta \theta_e}{\tan \theta_e / 2} \right) \quad (3.21)$$

At low y there is no divergence whereas at high y the error depends on $(1 - y)$ but is still dominated by the error on δ_{had} . We decided to use this method after a check of the resolutions with different methods, simply looking at the percentage differences between reconstructed and "true" variables by an inclusive MC sample (see figures 3.6, 3.7, 3.8 and 3.9). The averages of the bins with the standar deviations are plotted for every reconstruction method.

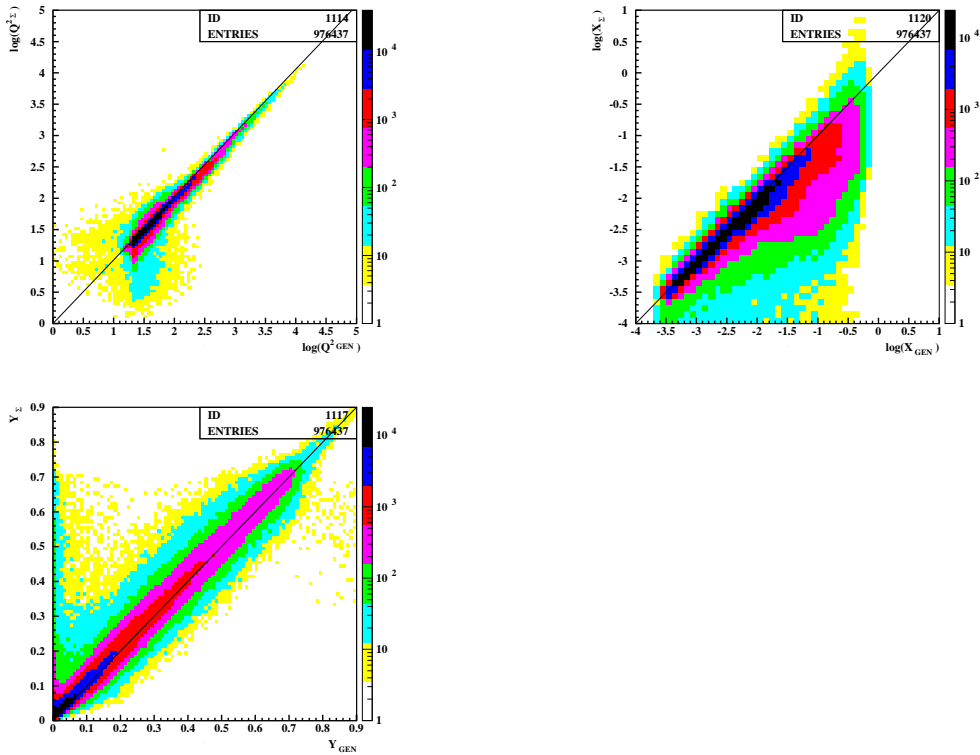


Figure 3.5: Scatter plots of Kinematic variables, Q^2 and x on the top, y below (reconstructed versus generated) for an inclusive MC sample using Σ method.

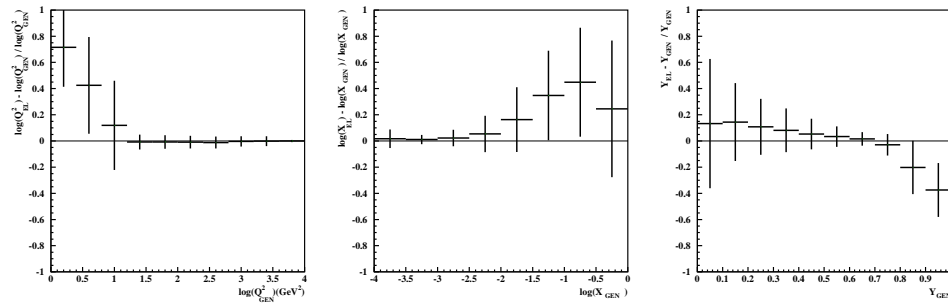


Figure 3.6: Plots of kinematic variables, Q^2 , x and y ((reconstructed-generated)/generated) versus the same variables at the generator level for an inclusive MC sample using Electron method.

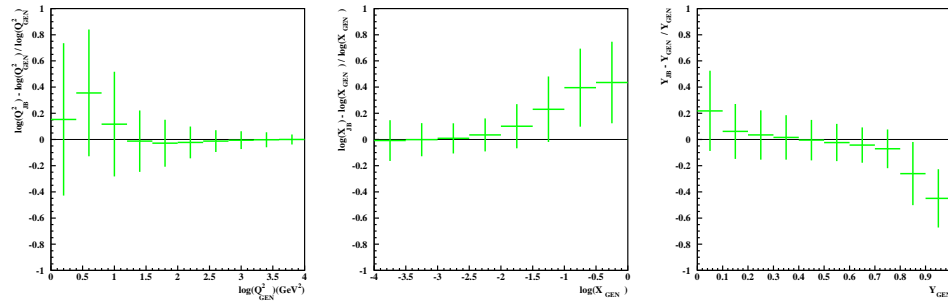


Figure 3.7: Plots of kinematic variables, Q^2 , x and y ((reconstructed - generated)/generated) versus the same variables at the generator level for an inclusive MC sample using Jacquet-Blondel method.

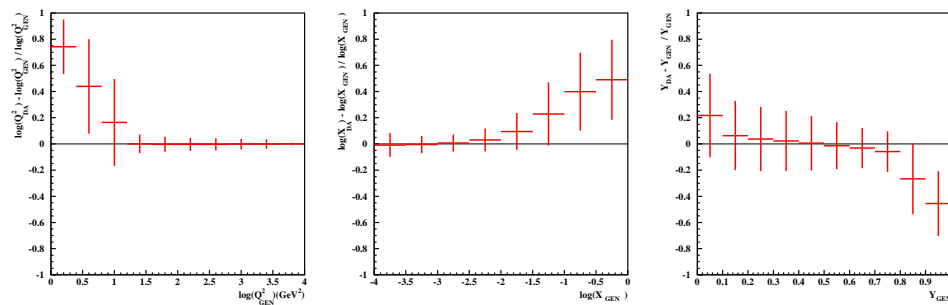


Figure 3.8: Plots of kinematic variables, Q^2 , x and y ((reconstructed - generated)/generated) versus the same variables at the generator level for an inclusive MC sample using Double Angle method.

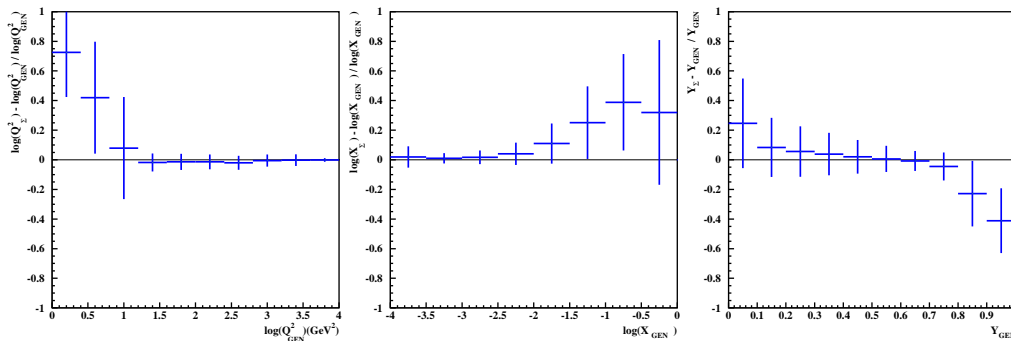


Figure 3.9: Plots of kinematic variables, Q^2 , x and y below ((reconstructed-generated)/generated) versus the same variables at the generator level for an inclusive MC sample using Σ method.

3.2 Electron identification and reconstruction

In the measurement of DIS processes the identification of the scattered lepton is of vital importance. The kinematics of the scattered electron in DIS events are summarized in Figure 3.10 where lines of constant electron energies and angles in the (x, Q^2) phase space are drawn. Due to the $1/Q^4$ dependence of the lepton-nucleon cross section most interactions involve small momentum transfer, i.e. the lepton is scattered at small angles and can eventually escape through the beam pipe, represented by the yellow region in Figure 3.10 (on the right side).

3.2.1 Electron identification

The identification of the electron with the detector is performed by so-called electron finders. Several of such programs exist within ZEUS. Each one was developed for a special purpose, e.g. finding electrons in the RCAL or finding electrons in events with high Q^2 . The main electron finder, that is used for the determination of all cross sections in this analysis, is called EM. It was specially developed to identify electrons in the high Q^2 regime and also has a superior background suppression in the corresponding detector region [52]. For the alignment studies in the RCAL, another electron

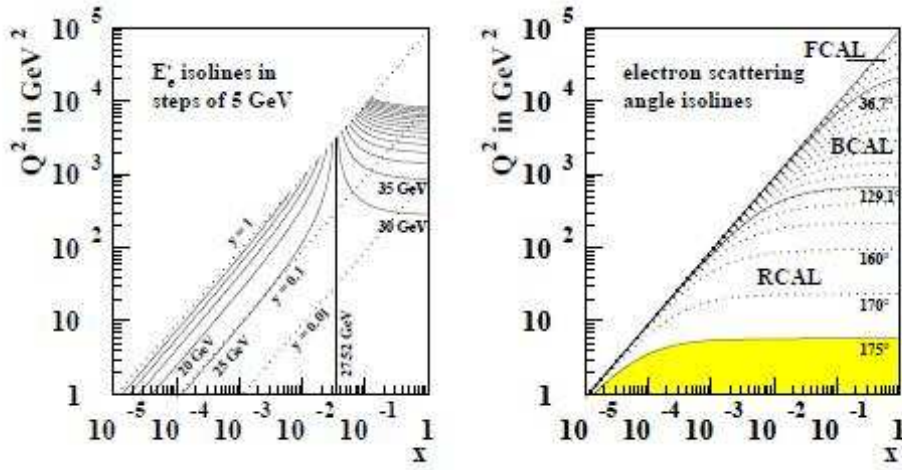


Figure 3.10: *Contour lines of fixed electron energy (left) and angle (right) in the HERA kinematic plane. On the left plot the isolines corresponding to $y = 0.01, 0.1$ and 1 are shown. On the right plot the regions covered by the different sections of the calorimeter are separated by solid lines. The yellow area corresponding to values of the polar angles $\theta_e > 175^\circ$, which are outside the acceptance of the rear calorimeter.*

finder called SINISTRA95 was used. It was conceived mainly for the electron identification in the RCAL and additionally provides HES information which is extensively used in these studies. Both finders select the scattered electron from a list of electron candidates. This list is sorted by probability as calculated by the electron finder. The electron candidate with the highest probability is selected if its probability lies above a certain threshold.

EM finder

To come to a decision, EM uses both calorimeter and track information and additionally takes geometrical properties of the detector into account. Overall, EM uses 7 variables to distinguish between electrons and hadrons, where 4 variables refer solely to calorimeter information, e.g. the energy spread of the electron candidate in the calorimeter or its isolation with respect to other energy deposits. The remaining 3 variables describe

the matching quality of calorimeter and track information like track momentum vs. calorimeter energy or the reconstructed scattering angle. The differences in the distributions for signal and background events are used to calculate a probability function for each variable [53]. The total probability of an electron candidate is then determined by multiplying the individual probabilities, obtained from the probability functions. An EM electron candidate consists of a cell cluster in the calorimeter and, if available, a track in the CTD pointing to that cell cluster. To form the cell clusters, the following cell island algorithm is applied:

- All cells with a non-zero energy deposit are considered. Neighboring cells are defined as those which touch the main cell with at least one edge. This is also valid for cells of different types (EMC, HAC1, HAC2). A cell is defined as a local maximum, if it is surrounded only by neighboring cells with lower energy.
- The calorimeter cells are sorted by energy in descending order.
- One starts with the top cell in the list which, having the highest energy, automatically forms a local maximum. For subsequent cells j one verifies for all other cells i with $i < j$, whether cell j is a neighbor of cell i according to the definition above. If this is true, cell j is assigned to cell i . Otherwise cell j itself becomes a local maximum and therefore a seed of a new cell island.

The island algorithm is implemented in EM and therefore accessible via this program. To be accepted as an electron candidate, the cell island must have a calorimeter energy of at least 4 GeV and the calorimeter probability (probability product of all 4 calorimeter variables) must be greater than 10^{-5} . In addition, only 30% (50%) of the total energy of the cell island is allowed to be deposited in the hadronic section of the FCAL (BCAL). As EM also uses track information, a track matching algorithm is applied:

- To be considered, a track has to fulfill the following requirements:
 - $p_T > 0.1 \text{ GeV}$.
 - The distance of closest approach (DCA) to the beam line must be less than 2 cm.
 - The angular distance between the shower center and the impact position of the track on the calorimeter surface must be less than 45° both for the azimuth and the polar angle.
 - The DCA of the track extrapolation into the calorimeter and the shower center must be less than 50 cm.
- If a track survives all these cuts, EM calculates the track probability (probability product of all 3 variables containing track information).
- The track with the highest track probability is assigned to the calorimeter cluster. If no track passes the cuts, the cluster is treated as a trackless electron candidate.

In addition, EM contains an algorithm which allows to merge the islands of the electron and the photon in case of FSR events. EM investigates all islands which are in an $\eta - \phi$ cone of radius 0.8 around an electron candidate, where η is the pseudo-rapidity defined as $\eta = -\ln(\tan \frac{\theta}{2})$. If the calorimeter probability of an island is greater than 0.002 and its energy exceeds 0.4 GeV but lies below the energy of the electron candidate, the electron candidate and the island are merged to a new candidate. This new candidate must have a probability greater than 0.001, otherwise it is deleted and the original electron candidates are used. If an electron candidate has more than 1 island in its $\eta - \phi$ cone of radius 0.8, then the merged candidate with the best total probability is taken. The electron–island in a merged candidate is the island with the highest track probability. If both islands have no track, the electron is the one with the highest energy. The position of the merged candidate and other quantities are set to those of the electron–island, whereas

the four-momentum is the sum of the four-momenta of the electron and the photon (calculated from the energy and position of the electron in the calorimeter and the event vertex).

If an electron candidate has been identified as the scattered electron, i.e. the candidate has the greatest probability of all candidates in an event and this probability lies above a certain threshold, its properties are calculated. The total energy is the sum over the energies of the cells belonging to the electron cluster. The final position of the electron in the calorimeter is calculated from the four-momentum and the event vertex in order to take potential FSR photons into account.

3.2.2 Reconstruction of the electron scattering angle

Once the electron has been identified in the calorimeter, the scattering angle θ_e can be measured combining the impact position at the calorimeter with the event vertex. The impact position is measured from the calorimeter cells associated to the electron candidate, but the CTD and SRTD detectors are used to improve the measurement whenever the electron trajectory lies within the respective acceptance region. For the reconstruction of the electromagnetic shower in the RCAL only those cells are used, which are connected by at least one corner to the cell of maximum energy [54]. The y -coordinate is calculated through the logarithmic average of three cells to ensure a uniform resolution over the entire y -range of a cell. The x -coordinate is instead calculated starting from the identification of the shower center in each cell, given by the imbalance of the left and right energy measurements in one cell. From these three x -positions the final position is calculated using weights proportional to the logarithm of each energy. The position resolution achieved by this algorithm is ~ 1 cm in both coordinates.

The low Q^2 region corresponding to $\theta_e > 162^\circ$ is covered by the SRTD detector whose fine segmentation allows a resolution almost three times more precise than the one of the calorimeter. The reconstruction of the impact

position proceeds in three steps [55]. Signals above threshold of consecutive scintillator strips are grouped into clusters in each plane. The algorithm then pairs clusters of horizontal and vertical strips into hits and calculates the hit position with a center of gravity of the three central strips in the shower maximum. About 70% of the events selected in this analysis are reconstructed using this procedure.

In the region at higher Q^2 values ($\theta_e < 157^\circ$) the reconstruction is improved by requiring an association of the calorimeter cluster with a good CTD track. The track must traverse at least three superlayers of the CTD, have a distance of closest approach to the calorimeter cluster of less than 10 cm and momentum greater than 5 GeV. In the angular region $157^\circ < \theta_e < 162^\circ$ the calorimeter position is used.

3.3 Reconstruction of the hadronic system

After the identification and reconstruction of the scattered electron in the calorimeter, the hadronic final state can be reconstructed. The energy resolution of a sampling calorimeter is mainly determined by sampling fluctuation in the shower development. Since shower phenomena are driven by statistical processes the fractional resolution improves with increasing energies scaling inversely as the square root of the incident energy E :

$$(\sigma/E) \propto 1/\sqrt{E} \quad (3.22)$$

Additional limitation at low energy may be introduced by instrumental effects whose relative contribution also decreases with E . In case of multiwire tracking chambers the precision of the momentum measurement depends on the curvature radius R of the particle trajectory in the magnetic field. It is straightforward to show that the error on the radius is of the form $\sigma(R) \sim \sigma_{hit}R^2$ and, since the transverse momentum p_T of the track is proportional to R , the form $\sigma(p_T) \sim p_T^2$ follows immediately. The fractional resolution is thus:

$$(\sigma/p_T) \propto p_T \quad (3.23)$$

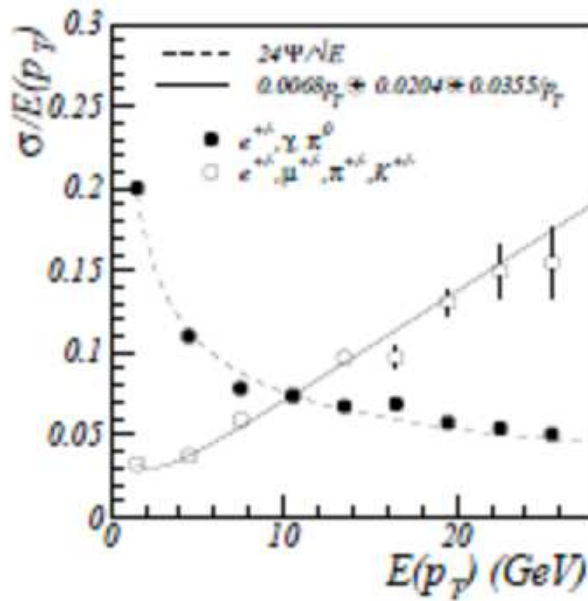


Figure 3.11: CTD and CAL electro-magnetic resolution [56]

The fractional resolutions measured in the ZEUS EMC calorimeter and the central tracker are drawn in Figure 3.11. From the picture it is easy to conclude that a sensible reconstruction of all particles belonging to the hadronic final state can be achieved combining the CTD measurement in the low energy region and the CAL measurement in the region starting from 10 – 15 GeV . In the next paragraphs we will discuss in detail how the particle reconstruction is achieved in the calorimeter and in the tracking system. In addition, we will explain why additional corrections are needed.

3.3.1 Reconstruction of the hadronic system using Energy Flow Objects(ZUFOS)

In Figure 3.12 a schematic representation of calorimeter and tracking information is shown. As a first step, after removing the calorimeter cells assigned to the scattered electron, the calorimeter energy deposits are clustered using a two stage algorithm. The reason for introducing a two stage algorithm

is dictated by the structure of the ZEUS calorimeter. As mentioned in Section 2.6 it is divided into three, spatially separated main sections. This spatial separation implies several complications for a local clustering algorithm in handling the energy deposits of a single particle which is not confined to one calorimeter section, since the energy will be split into two or more clusters. Therefore, the first stage of the clustering procedure is performed in each calorimeter layer separately. Each cell with sufficient energy is considered a candidate to be connected with one of its neighbours. The connection is made with the nearest neighbour with the highest energy or with the highest energy cell next to the neighbour. This procedure is repeated for each cell and produces a unique assignment of a cell to a so called *cell island*.

The second stage of the clustering procedure collects the cell islands belonging to a shower of a single particle or a jet of particles into the so called *cone islands*. The matching of cell islands starts from the outermost hadronic layer of the calorimeter and proceeds inwards. The angular separation between cell islands of different layers is calculated in the space and translated to a probability according to a distribution determined from a single pion MC [57]. Links with highest probability are accepted provided that the probability is larger than a threshold. Once the linking procedure has been completed, the cone islands are generated by combining all calorimeter cells which point to the same cone island in the electromagnetic layer. Tracks are reconstructed independently using the ZEUS reconstruction software described in Ref. [58]. Each track is first extrapolated to the calorimeter surface and then further into the calorimeter, assuming a linear trajectory given by the track momentum unit vector at the end of the helix swim. The distance of closest approach is then calculated, defined as the shortest distance between the track trajectory and the calorimeter island. The track–island association is dictated by the properties of the hadronic final state being analyzed. In an inclusive sample of DIS events the average multiplicity of particles is approximately proportional to $\ln(W^2)$. In these events some calorimeter islands are due to energy deposits of single particles whereas others are due

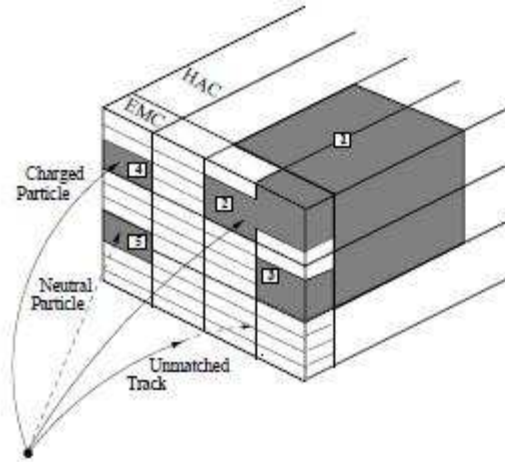


Figure 3.12: Schematic representation of a ZUFO.

to energy deposits of several particles. A sensible quantity to perform the track-island association is, therefore, the lateral extension of the calorimeter island. Thus, a track and a cone island with a distance of closest approach d are associated if the following condition is satisfied:

$$d \leq \max(r_{min}, r_{island}) \quad (3.24)$$

where r_{island} is the radius of the cone island and $r_{min} = 20$ cm is a parameter extracted from a MC simulation by maximizing the track–island matching efficiency for single particle calorimeter clusters [57]. The set of associated track–islands, known as ZUFOs, are processed according to the following criteria:

- Charged tracks without any associated calorimeter object are considered as pions. The energy is calculated from the CTD measurement and the pion mass.
- Calorimeter islands without any associated track are considered as neutral particles.

- Calorimeter islands associated to more than three tracks are considered as one jet of particles.

In case of a one-to-one correspondence the use of the track momentum instead of the calorimeter island is based on two conditions.

As a first check, the energy E_{CAL} of the calorimeter island and the momentum p of the associated track must satisfy the condition:

$$E_{CAL}/p < 1 + 1.2 \cdot \delta(E_{CAL}/p) \quad (3.25)$$

where $\delta(E_{CAL}/p)$ is the error on the energy/momentum ratio.

In addition, the resolution of the momentum measurement must be smaller than the resolution on the respective energy measurement,

$$\delta p/p < \delta(E_{CAL}/E_{CAL}). \quad (3.26)$$

The track momentum is also preferred if the object satisfies the following requirements: $E_{CAL} < 5 \text{ GeV}$, $E_{CAL}/p < 0.25$, $p < 30 \text{ GeV}$. These conditions are typically fulfilled by muons, which normally traverse the calorimeter thickness generating an energy deposit of few GeV . As we will discuss in Section 3.3.3, further corrections are applied whenever one ZUFO is associated to a muon candidate.

3.3.2 Energy correction to ZUFOs

Detailed studies on data and Monte Carlo simulation have highlighted the need to apply the following corrections on the islands reconstructed in the calorimeter [59]:

- *Energy loss in the inactive material between the interaction point and the calorimeter.* The contribution of the beam pipe, tracking detectors and the solenoid to the energy loss varies with the polar angle between 1 and 3 radiation lengths X_0 (see Figure 3.13). Energy losses are more significant for low energy particles and are generally difficult to include

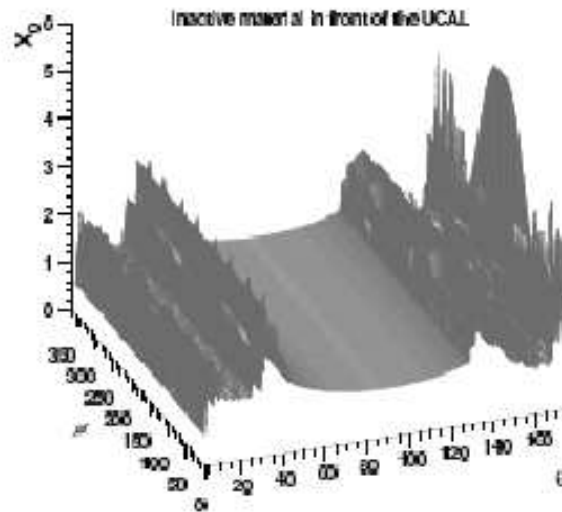


Figure 3.13: Distribution of inactive material between the interaction point and the ZEUS calorimeter as function of the polar and azimuthal angles of a particle produced at the nominal interaction point.

in the detector simulation. Additional correction factors are therefore parameterized as function of the polar angle and of the island energy and applied to the calorimetric ZUFOS.

- *Energy overestimation of low momentum hadrons.* Protons and pions with momentum under 1 GeV lose their energy mainly through ionization without hadronic interactions. For those particles the calorimeter is not compensating, i.e. $e/h \sim 0.6$. This effect implies an overestimation of low energy islands.

3.3.3 ZUFOS associated to muons

As discussed in the introduction to this Chapter the final state of the events selected by this analysis contains most of the times muons inside the hadron jet. Since the energy release of a muon traversing the calorimeter

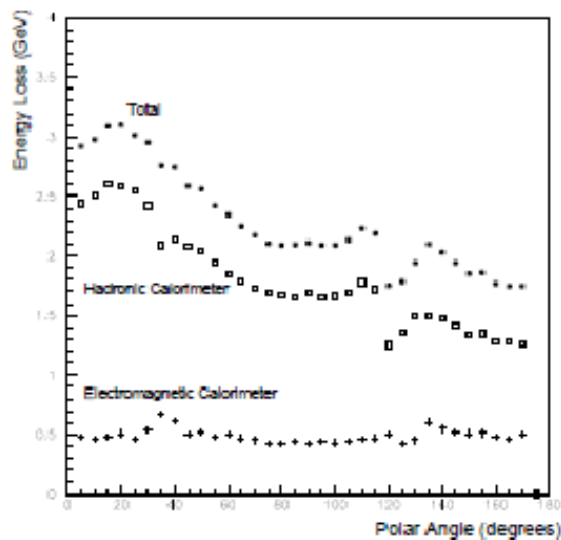


Figure 3.14: Muon energy loss in the ZEUS calorimeter as a function of the polar angle (full circles). The energy fractions released in the electromagnetic calorimeter (crosses) and in the hadronic calorimeter (open squares) is shown [59].

is dominated by ionization, the measured energy is not proportional to the momentum of the incoming particle. They traverse the calorimeter, leaving only the minimal ionizing particle (Mip) energy. The inclusion of the calorimetric measurement of the muon four-momentum in the particle jet would generally lead to an underestimation of the jet energy. In this context the use of ZUFOs instead of the bare calorimeter cells helps to correctly evaluate the particle momentum using the tracking information. Nevertheless when the muon ZUFO is a calorimetric island some additional corrections are required.

As a first step, the energy release of the muon in the calorimeter has been parameterized as a function of its polar angle. The dependence, obtained from a sample of isolated muons, is plotted in Figure 3.14. The average energy loss of the muon is of about 1.5-3 GeV, a value which is consistent with the difference between the momentum measurement of the CTD and of the muon chambers. For each muon candidate identified in the tracking and

muon chambers the corresponding ZUFO is searched applying the correction according to the following scheme [59]:

- *The corresponding ZUFO is a track.* No action is needed.
- *The corresponding ZUFO is a calorimeter island whose energy is compatible with a muon.* If the island energy is between 50% and 150% of the energy release expected from Figure 3.14 the ZUFO is substituted with the tracking measurement.
- *The corresponding ZUFO is a calorimeter island whose energy is bigger than the one expected from a muon.* This is case in which the muon is included in a jet. The muon ZUFO is then splitted in two ZUFOs: the first is set to the muon momentum measured with the tracking while the second is obtained by the difference of the original island and the energy loss expected by our parameterization. In this way the muon contribution to the jet is correctly reconstructed;
- *Other cases.* If the muon points to an island whose energy is much lower than what expected from the energy parameterization or no island is found the tracking measurement is substituted to the reconstructed ZUFO.

3.4 Tracks and vertices reconstruction

VCTRACK [47] is the package used in ZEUS for the reconstruction of tracks and primary and secondary vertices inside the detector. Its development, begun in 1990, is still undergoing because of the different configurations of the ZEUS tracking system. All reconstructed tracks use mostly hits from the CTD although information coming from other tracking devices (MVD, STT) are taken into account.

For this thesis information coming from the MVD is essential to study the

decays of particles containing heavy quarks. The decay length in the transverse plane of a generic particle of mass m , mean lifetime $c\tau$, and transverse momentum P_T is approximately given by:

$$\lambda_{xy} = P_T \frac{c\tau}{m} .$$

Therefore decays of hadrons with a momentum of a few GeV could be discriminated from the primary vertex if $c\tau$ is large enough (of the order of $10^2 \mu m$). For this analysis the measurement of the impact parameter of tracks originating from c or b decays requires a precise reconstruction of the tracks and of the primary vertex of the event. The reconstruction of the tracks and vertices by VCTRAK can be summarised in three basic steps:

- pattern recognition
- track fit
- vertex finding

which will not be discussed in detail in this thesis.

3.4.1 MVD information

At the end of 2002 a new version of VCTRAK including the MVD information became available; the improvements with respect to the old version which used only CTD information are the following:

- track finding efficiency: using the MVD already in the pattern recognition stage, an efficiency improvement of $\sim 3\%$ can be obtained (from 93.5 % using only CTD information to $\sim 97\%$ including also the MVD information)
- trajectory precision: the precision in the trajectory determination is significantly improved

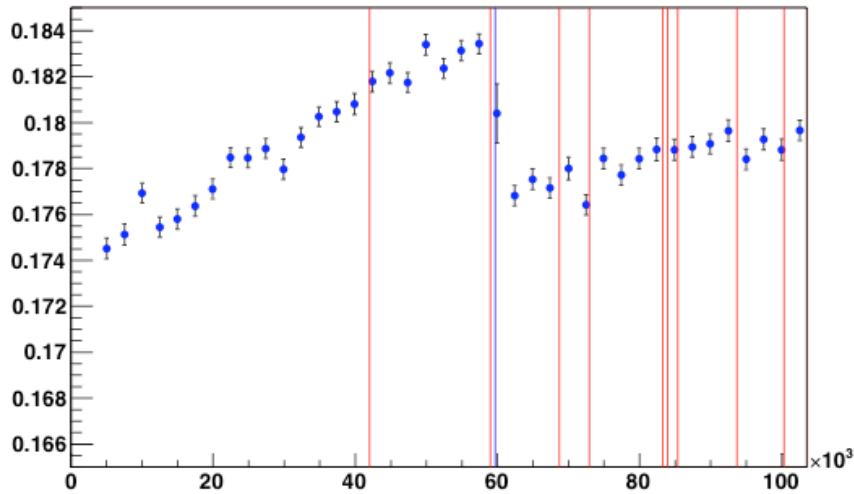


Figure 3.15: Beam spot Y position mean (cm) as a function on the event number recalculated every 2000 events. The vertical red lines represent a change of an HERA fill.

- vertex finding: the primary vertex resolution is improved as well as the efficiency in the identification of secondary vertices.

In this analysis a new tracking package, Rigorous Track Fit (RTFIT) has been used to have the best results.

3.4.2 Beam spot and MVD alignment

Beam Spot

For this thesis, the precision on the reconstruction of the primary vertex plays an important role, affecting the measurement of the impact parameter of the considered tracks. In order to achieve the best resolution for the x and y coordinates, an average vertex position, the *Beam Spot* (B.S.), was determined using a considerable number of events. It was re-calculated averaging the primary vertex positions every 2000 'good' events, after applying some quality cuts on the tracks participating in the fit and background reduction cuts. All runs within a fill are considered contiguously (see fig. 3.15). The

vertex distributions in x, y and z were then plotted and fitted using a Gaussian. The beam-tilt, that describes the non-uniform distribution along z of the beams, has been also calculated. This was obtained by a straight line fit through x/z and y/z plots.

The reasons we decided to use B.S. instead of primary vertex as reference for the measure of the impact parameter are:

- it is practically *uncorrelated* with the tracks in the actual event, furthermore gives an *unbiased reference* for decay lengths, while the primary vertex may be biased by other long-lived particles;
- its simulation is easier than the primary vertex one;
- its resolution is much better than the primary vertex one.

Impact Parameter resolution

Visible Impact Parameter (I.P.) resolution is governed by 2 effects:

- intrinsic I.P. resolution of track
- effect from interaction point spread

$$(\sigma_{I.P.}^{vis})^2 = (\sigma_{I.P.}^{track})^2 + (\sigma_{I.P.}^{BS})^2 \quad (3.27)$$

- where

$$(\sigma_{I.P.}^{BS})^2 = (\sigma_x^{BS})^2 \sin^2 \phi + (\sigma_y^{BS})^2 \cos^2 \phi \quad (3.28)$$

We can estimate intrinsic track I.P. resolution by

$$(\sigma_{I.P.}^{red})^2 = (\sigma_{I.P.}^{vis})^2 - (\sigma_{I.P.}^{BS})^2 \quad (3.29)$$

Beam spot modulation is removed in subtraction; the plot in Fig. 3.16 point out the importance of this factor, nevertheless the reduced resolution plot shows the extrapolation distance dependence. By design, in HERA-II the

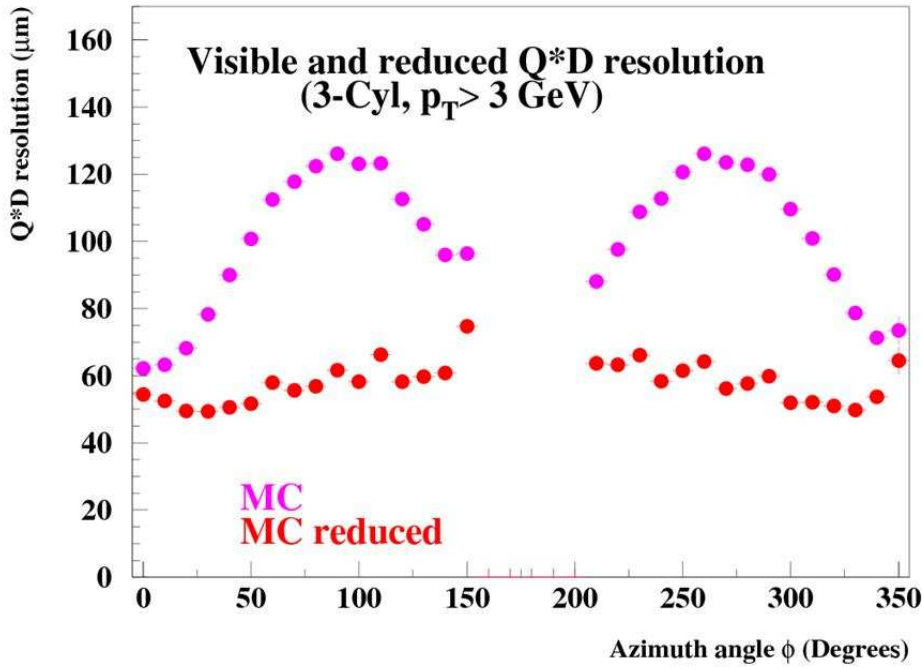


Figure 3.16: Visible I.P. resolution (violet dots) for a MC sample that consists of tracks passing 3 MVD Barrel Cylinders (3-Cyl) with a minimum p_T of 3 GeV. Is also shown the reduced I.P. resolution (red dots) still for the same MC sample. The beam spot modulation is clearly visible on upper violet dots as soon as an extrapolation distance dependence can be notice on lower red dots.

beams have Gaussian widths of $\sim 110\mu m$ horizontally and $\sim 30\mu m$ vertically. The measured values are:

$$\sigma_X^{BS} = 83\mu m \quad \sigma_Y^{BS} = 20\mu m. \quad (3.30)$$

and for the Monte Carlo we have

$$\sigma_X^{BS} = 110\mu m \quad \sigma_Y^{BS} = 30\mu m. \quad (3.31)$$

After all the track resolution shows that there is still a difference between Data and MC (see Fig. 3.17). Resolution in Data is somewhat wider than MC. The possible reasons of that are related to alignment uncertainty.

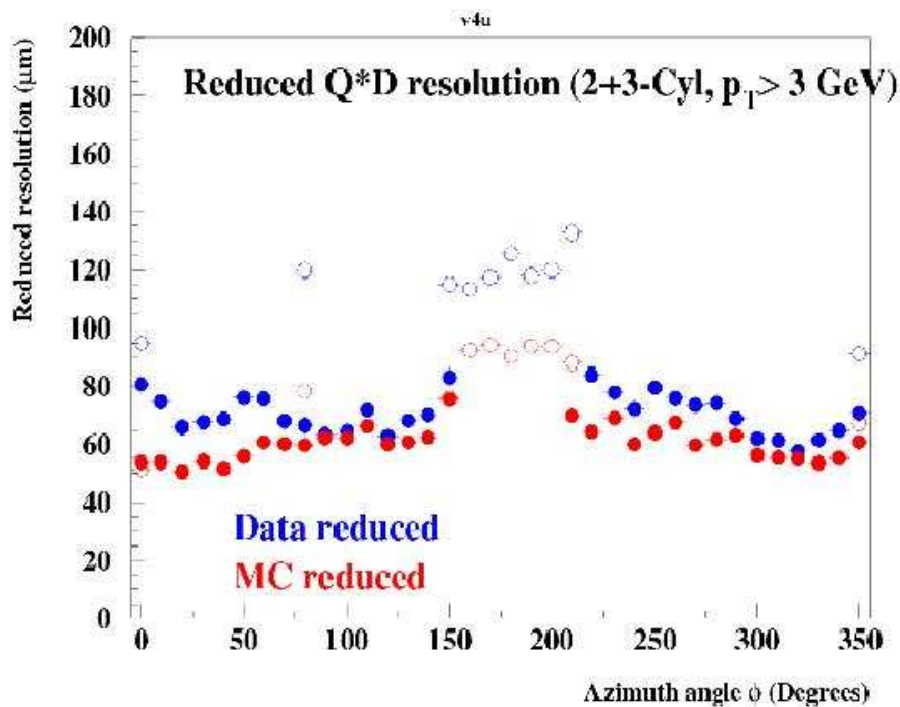


Figure 3.17: Impact parameter reduced resolution in data (blue circles) and MC (red circles). The filled circles represent tracks of $p_T > 3$ GeV with hits in 3 MVD Barrel Cylinders (3-Cyl); the empty circles represent tracks of $p_T > 3$ GeV with hits in 2 Barrel MVD Cylinders (2-Cyl).

Barrel MVD Alignment

MicroVertexDetector alignment is a very important issue to take into account if we want to have a realistic description of the detector. We know that the hit resolution of MVD is $\sim 20 \mu m$; this requires accurate knowledge of real sensor and ladder positions ($< 20 \mu m$). During 2002-04, cosmic runs were the basis of a first track-level alignment. Low multiplicity high momentum tracks crossing the detector were reconstructed. That allowed for a precise determination of the detector position parameters. A χ^2 fit on the hit residuals of cosmic tracks is performed for each ladder individually. In total there are 180 parameters for the barrel MVD: 30 ladders with 3 translations and 3 rotations each. Anyway, this kind of alignment suffers of some

limitations:

- long processing time due to the iteration of fits;
- is only possible for Barrel MVD;
- due to the geometry of cosmic tracks it was less successful in the side regions of barrel; a non-uniform angular coverage leads to poorer resolution in this regions.

The accuracy achieved with this kind of alignment is $\sim 50\mu m$

A second alignment was based on tracks from ep events. These tracks provide coverage in all regions of the MVD and hence can be used to improve the alignment in all areas of the MVD. The best alignment accuracy to date has been reached with this method (see Fig. 3.18). It essentially allows a simultaneous least squares fit of all alignment and track parameters (no iteration required). There is one set of global (alignment) parameters and many sets of local (track) parameters. This enables the problem to be reduced to a solvable size without making any approximations. The resulting accuracy of alignment parameters is of $\sim 25\mu m$, closer to the design one.

The final resolution after global(MVD/CTD) alignment with cosmics and local alignment with ep interaction is $\sim 65\mu m$ for 3-Cyl tracks and $\sim 120\mu m$ for 2-Cyl tracks

3.5 Jet reconstruction

The jet algorithm should provide an approximated reconstruction of the outgoing quarks in the hard scattering and distinguish between the remnant of the proton and the jets from the hard process. To be suited for comparisons with pQCD calculations, the jet algorithm has to fulfill the following requirements:

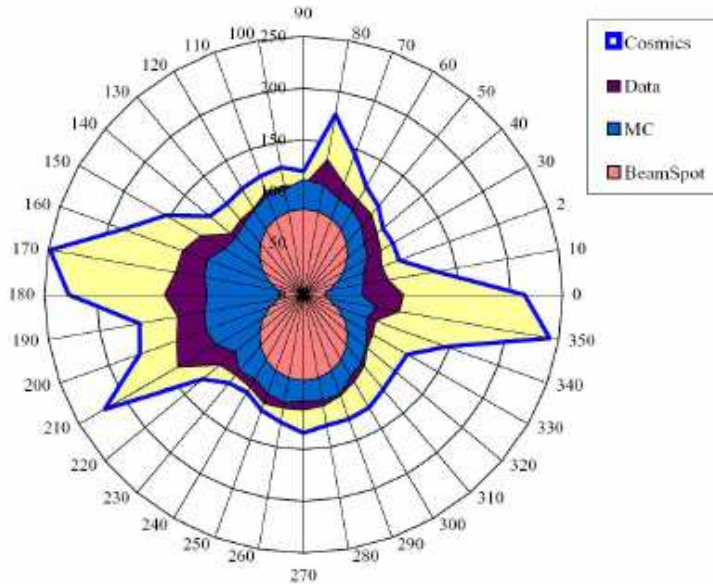


Figure 3.18: Radial plot of the impact parameter resolution as a function of the track azimuthal angle. Cosmic alignment, ep alignment (labelled as Data) are compared to MC. The contribution due to B.S. modulation is also shown. The ep alignment improvements are clearly visible

- *collinear safety*: the resulting jets have to be independent of one parton splitting into two partons moving collinearly. Translated to the experimental point of view, the jet algorithm has to be independent of one particle releasing energy in two adjacent Cal cells.
- *infrared safety*: the resulting jets have to be independent of the emission of very low energy particles. Experimentally, this is also related to the noise in the detector.
- correct treatment of beam remnants especially of the proton and eventually of the photon.
- Lorentz invariance: independence from longitudinal Lorentz boosts.

The separation between the soft and the hard processes is achieved by a cut on the transverse energy in a frame where all the E_T has to be produced by the hard scattering. In deep inelastic scattering one has to deal with the proton remnant and isolate the latter from jets with high transverse momentum. In this section we will describe the jet clustering algorithm that has been used.

3.5.1 The longitudinally invariant k_T clustering algorithm

The so called k_T algorithm has been originally introduced by Catani, Dokshitzer and Webber for e^+e^- collisions [61] and later modified by Ellis and Soper to the $p\bar{p}$ case [62]. The algorithm consists of an iterative clustering procedure [60]. Starting with the initial list of objects (the ZUFOS of previous section in our case) belonging to the hadronic final state, each one characterized by a transverse momentum $E_{T,i}$, azimuthal angle ϕ_i and pseudorapidity η_i , the algorithm proceeds as follows:

1. *Pre-clustering*: for each object i in the final state one computes two "distance" variables, $d_{i,beam}$ e $d_{i,j}$, where j loops over the whole final state objects for $i \neq j$. They consist in

$$d_{i,beam} = E_{T,i}^2 \quad (3.32)$$

$$d_{ij} = \min(E_{T,i}^2, E_{T,j}^2) [(\eta_i - \eta_j)^2 + (\phi_i - \phi_j)^2] \quad (3.33)$$

2. If N is the total number of objects in the final state, we have to find the smallest value of all the $d_{i,beam}|_{i=1,N}$ and $d_{i,j}|_{i=1,N;j=1,N;i \neq j}$ and label it d_{min} .
3. If d_{min} is one of the $d_{i,j}$ merge the objects i and j into a new *cluster* k following the proper recombination scheme (see next par.), whereas if d_{min} is one of the $d_{i,beam}$, the i -th object is not anymore recombined with the j -th object.

4. This procedure will be repeated for every object or cluster till the final object has $d_{i, beam} < d_{i,j}$ and there are no more combinations available.
5. The *jets* are defined as objects with $d_{i, beam} > D_{cut}$ whereas the objects with $d_{i, beam} < D_{cut}$ are associated to the *beam* where $D_{cut} = E_{T,min}^2$

In this analysis the jets are first preselected with a loose E_T cut of $2.5 GeV$. A slightly harder E_T cut of $3 GeV$ is applied in the final event selection. In addition, the polar and azimuthal angles are required for each jet in order to restrict the measurement in a region of the detector which is well understood.

3.5.2 Recombination schemes

Recombination schemes used by jet finders can influence the jet property during reconstruction, and in particular the corrections to hadronizations level. The most important are:

- *Massless(p_T)*: the kinematic variables for the pseudo-particles are obtained by

$$E_T^{jet} = \sum_i E_{T,i}, \quad \eta^{jet} = \frac{1}{E_T^{jet}} \sum_i E_{T,i} \eta^i, \quad \phi^{jet} = \frac{1}{E_T^{jet}} \sum_i E_{T,i} \phi^i$$

- *Massive(E)*: this scheme reconstructs the jets as massive particles; this pseudo-particle is considered as a real particle with momentum $\vec{p} = \sum_i \vec{p}_i$ and energy $E = \sum_i E_i$. This is used for heavy flavour jet

In this analysis we used the Massive scheme

3.6 Muon reconstruction

The semi-leptonic muons are reconstructed combining the informations of the tracking detector and of the muon chambers. The muon trajectory is reconstructed in the inner tracking detectors (MVD,CTD) and then traverses the uranium calorimeter before reaching the inner muon chambers. Since the

magnetic field inside the calorimeter is very low compared to the one inside the solenoid, the displacement of the trajectory from a straight line is mainly due to multiple scattering. Under these conditions, an efficient and precise reconstruction can be achieved if tracks upstream and downstream the calorimeter are joined using an accurate simulation of the particle trajectory and taking into account the full error matrices of the single reconstruction steps. For this purpose the muon chambers must be exploited not only as a muon tagger but as a real tracking device. Specific algorithms (BREMAT, MPMATCH, GLOMU, MUFO..) have been designed to associate inner detector tracks to the segments reconstructed in the muon chambers and provide the resulting matching χ^2 . We briefly describe the structure of used packages in the following sections.

3.6.1 The BREMAT package

The Barrel and Rear Extrapolation MATching package, BREMAT [63], is used to match segments reconstructed in the barrel and rear muon detectors to tracks measured in the inner tracking detectors, mainly the central drift chamber (see CTD Section 2.4), after they have been extrapolated to the inner muon chambers. Only muons with a momentum of at least $1 - 1.5 GeV$ traverse the CAL to reach the inner muon chambers. The limited streamer tubes, and the associated strips, used in the BRMUON detector have a resolution of the order of ~ 1 mm on both the coordinates they measure, x and y (see Section 2.7.2). The resolution of the momentum, measurable only using inner and outer chambers contemporaneously, is dominated for most of the muons by multiple scattering in the iron yoke placed between the inner and the outer chambers. Anyway, in this analysis, we used only inner or outer chamber separately (see section 4.5) therefore no momentum measure from these components is used. The most powerful way to reconstruct muons in this context requires that measurement errors, multiple scattering and energy losses are correctly taken into account. This is the technique used by the BREMAT code.

The main input to the algorithm is the MBXYSG table, containing the information on the reconstructed segments in the BRMUON chambers, and the VCTRHL table, containing the parameters of the tracks reconstructed by the inner detectors. When an entry in MBXYSG is found, i.e. a segment in the muon chambers, BREMAT looks for candidates to be associated to it in the VCTRHL table, i.e. between all the tracks reconstructed by the inner drift chamber. A loose preselection is done on VCTRHL tracks to be associated to MBXYSG segments:

- track momentum $p > 1$ GeV;
- track polar angle $\theta > 20^\circ$;
- track starting from the first CTD superlayer or from MVD and reaching at least the third superlayer;
- distance-of-closest-approach to the $x,y=0$ $|D_H| < 10$ cm
- z position of the distance-of-closest-approach to the reference point $|z_H| < 75$ cm;
- χ^2 per number of degrees of freedom (n.d.f.) of the track fit $\chi^2/n.d.f. < 5$;
- distance between a central point on a barrel/rear muon segment and the crossing point of a straight line obtained by continuing the track to the muon chambers $\Delta \leq 150$ cm.

The track requirement ensures an appropriate acceptance of the CTD. The cut on Δ has been safely set after a study of inclusive muon data samples to accept most of the low energy muons [65]. Selected tracks are extrapolated using the GeanE package [64] at the reference surface where the match with the muon segments is performed.

A muon segment can either consist of hits in the inner muon chambers or, if the muon reaches the outer muon chambers, of outer hits. In the last case, we could combine inner and outer chamber hits to get a reconstructed momentum.

The output of this algorithm is to find out a candidate muons and provide the resulting matching. We can get two kind of matching depending of we measure or not muon nmomentum.

In the first case (INNER and OUTER) we have a 5 d.o.f. matching probability; in the second case (INNER or OUTER), we have 4 d.o.f. matching probability. These probabilities give us an idea of the quality of our matching, and will be used during our selection cuts to remove bad reconstructed muon candidates.

3.6.2 MPMATCH

For forward muons, the algorithm equivalent to Bremat is called Mpmatch [66]. It matches tracks in the forward muon chambers with tracks from the CTD in the overlap region of the CTD and the forward muon chambers. Tracks reconstructed by the FMUON reconstruction package MFRECON are stored in the ADAMO table MFRTZ that gives the track state vector at the z of most internal hit associated to the track (see Fig. 3.19). Only tracks with at least three radial and three azimuthal coordinate measurements are saved in the table. The algorithm matches the MFRTZ tracks with CTD tracks and gives the best estimate of the muon parameters at the vertex. This is done by extrapolating the MFRTZ state vector to the FCAL face using the GEANE package [67], combining it with the CTD track state vector extrapolated to the FCAL face as in the table VCPARCAL and back-extrapolating the new state vector to the vertex Z . Figure 3.20 shows the efficiency of the FMUON-only tracks (MFRTZ), and matched MPMATCH tracks as a function of p_μ and θ_μ as determined from a single- μ MC. Below $\theta = 0.2$ rad the CTD efficiency drops to zero. In the range $0.2 < \theta < 0.4$ muons are in the CTD

acceptance and in the region of full acceptance of the FMUON spectrometer that provides also an independent measurement of the muon momentum. In the range $0.4 < \theta < 0.55$ muons are in the gap region covered by the two "LT-Wall" planes, which provides a less redundant measurement and a low precision momentum estimate based on the Yoke magnetic field.

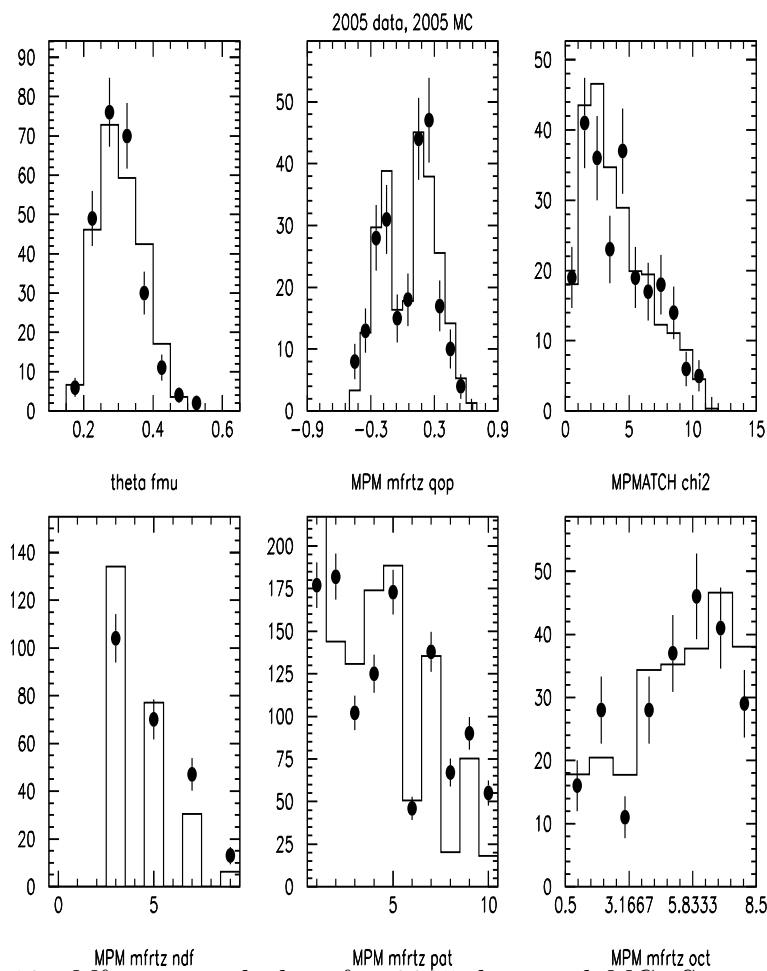


Figure 3.19: *Mfrtz control plots for 2005 data and MC. Starting from top left angle we show θ_{μ} , q/p , χ^2 of MPMATCH; below, from left to right, the number of d.o.f, the pattern describing the hit planes, the ϕ distribution. The plots refers to a J/Ψ elastic sample.*

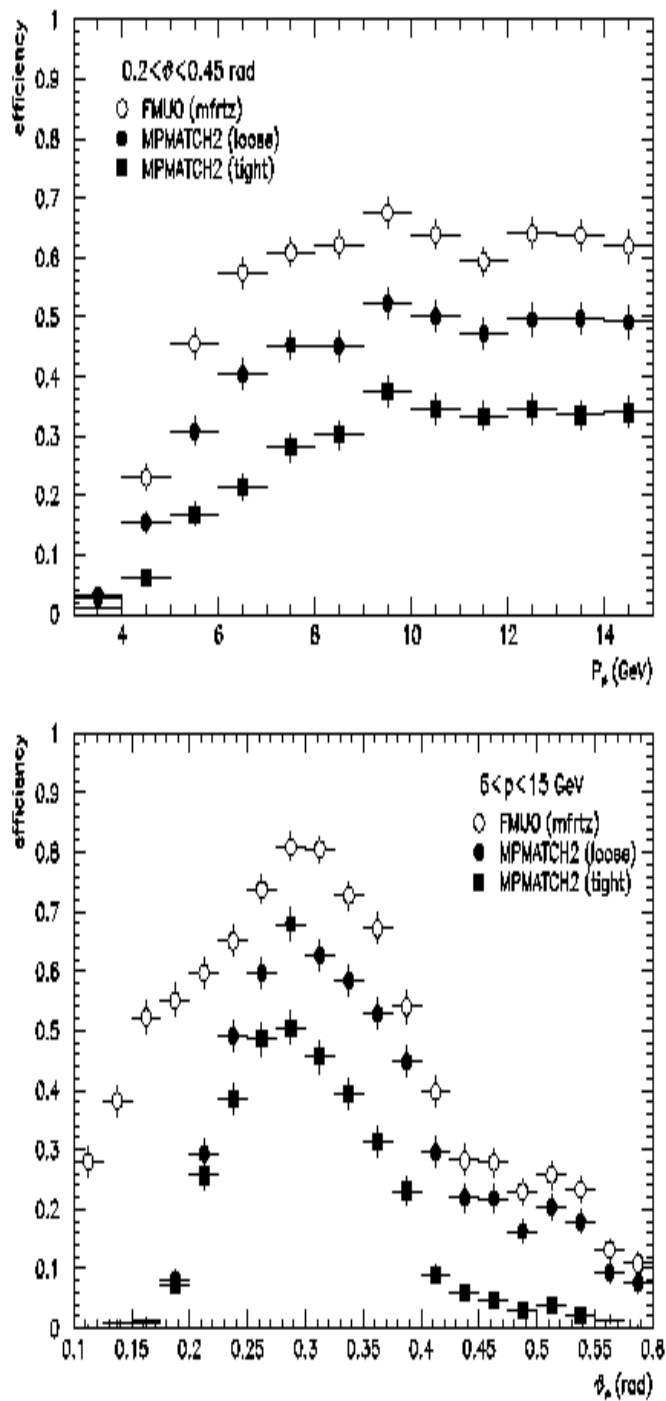


Figure 3.20: FMUON efficiency as a function of p_μ (up) and θ_μ (down) for the MFRTZ tracks (empty circles), for MPMATCH2 with default cuts (filled circles) and for MPMATCH2 with the cuts used in this analysis (filled squares). The efficiency are obtained from a MC sample of single muons with a flat distribution in θ and p .

Chapter 4

Event selection

To select candidates for heavy flavour production in DIS the first step is the restriction to DIS events using the EM electron finder, CAL properties and the tracking system. The semi-leptonic decay into a muon and a jet is selected by the requirement of at least one muon with some quality cuts and a jet containing this muon. These steps and additional cuts to improve efficiency and purity are explained in detail in this chapter.

4.1 Data and MC samples

4.1.1 DATA

In this work we analyse the data collected by ZEUS detector in the year 2005 with electron proton scattering. This final sample was depurated by all those runs which did not fulfill the standard ZEUS (EVTAKE) data quality requirements. Good data quality conditions have been requested as well for BRMUON (BMUTAKE [71]), FMUON (FMUTAKE) and MVD (MVD-TAKE) detector. The "TAKE-variables" are produced every year from ZEUS experts to describe the status of data taking for each run. EVTAKE represents the general status of ZEUS; it returns *FALSE* if the detector or essential part of it (CAL, CTD) are not working properly, or if the background is too high (Trigger rates). BMUTAKE, FMUTAKE and MVDTAKE give us

infos on the status of the respective components(BMUON,FMUON,MVD), run by run. We selected events with the following logic:

$$(EVTAKE.eq.TRUE).and. \quad (4.1)$$

$$((BMUTAKE.or.FMUTAKE).eq.TRUE).and. \quad (4.2)$$

$$(MVDTAKE.eq.TRUE) \quad (4.3)$$

The integrated luminosity corresponding to this sample amounts to **125.055** pb^{-1} for BMUON and **120.449** pb^{-1} for FMUON candidates.

4.1.2 Monte Carlo

This analysis concentrates on the selection of muons to gain a clean sample of heavy flavour events. The Monte Carlo program used in this analysis to generate ep-scattering events in the DIS regime is the RAPGAP [13] event generator. It is used to generate charm and beauty events as signal. The background of the muon selection comes from different processes (see section 4.4.3).

To account for processes with only light quarks (u,d and s) involved an inclusive DIS MC has been produced and used after exclusion of events containing charm or beauty quarks to avoid double counting. The background from light flavor events is simulated using Djangoh [76], an interface between Heracles [77, 78] and Ariadne [79].

The Heracles program, used by RAPGAP and DJANGO, simulates the ep-scattering in DIS, including first order electroweak radiative corrections. The hard scattering between the parton and the photon is simulated according to the Standard Model cross sections and the proton Pdfs. The parameterization of the Pdf is chosen according to the CTEQ5D [80] set of proton PDFs.

RAPGAP is used for QCD corrections in order to simulate the complete ep-scattering process. The first order BGF processe is simulated using the exact matrix elements. For higher order effects, QCD parton showers, based

Process	MC generator	Cuts	Cross section	Luminosity
Inclusive DIS	Ariadne	$Q^2 > 15 \text{ GeV}^2$	83330 pb	554.968 pb^{-1}
$\text{ep} \rightarrow \text{ccX}$	RAPGAP	$Q^2 > 16 \text{ GeV}^2$	21360 pb	699.968 pb^{-1}
$\text{ep} \rightarrow \text{bbX}$	RAPGAP	$Q^2 > 1 \text{ GeV}^2$	908 pb	1101.49 pb^{-1}

Table 4.1: *Configuration of Monte Carlo samples.*

on the leading log DGLAP [81, 83, 84, 82] splitting functions are used. They can occur before and after the hard subprocess. For the fragmentation, RAPGAP uses the Lund-string model, as it is implemented in JETSET/ Pythia [85].

ARIADNE uses the color dipole model (CDM). In this model, gluon emissions from a $q\bar{q}$ pair are treated as radiation from the color dipole between the quark and the antiquark. This model incorporates BGF as an extra process, while QCDC is included in the color dipole radiation. Like Rapgap, also Ariadne uses the Lund-string model for hadronization.

The RAPGAP MC predictions are not expected to describe the absolute number of events in the data. The normalization is usually taken from the comparison to the data. The MC sample is expected to describe the differential distributions in different variables in agreement with the data.

An overview of MC used in this analysis is given in Table 4.1. Due to the high cross section of the inclusive DIS sample, the signal generated sample are relatively small.

4.2 Pre-selection

The raw ZEUS data has been processed using Orange(overlying routine for analysis ntuple generation), a software library which executes a user-selected subset of a broad core set of analysis routines, in order to produce a reduced dataset of pre-selected data. The cuts require at least one electron candidate with a $Q_{DA}^2 > 17 \text{ GeV}^2$ and at least one muon from BREMAT or MPMATCH (see Sec. 3.6).

For the Monte Carlo sample, events are retained if they satisfy the same cuts on reconstructed quantities or if there is at least one true muon from semi-leptonic decays. The true muon is necessary for the cross section calculation (see Sec 5).

4.3 DIS selection

In the next section we will describe the cuts applied to select the inclusive sample of neutral current DIS events.

4.3.1 Data selection at trigger level

A standard NC DIS selection using trigger TLT slots has been applied. The global trigger logic on the basis of which the event is kept or rejected is an "or" of the following five bits:

SPP01 → $30 \text{ GeV} < E - p_z < 100 \text{ GeV}$ $E_{el} > 4 \text{ GeV}$ *Radiuscut* 30 cm

SPP02 → $30 \text{ GeV} < E - p_z < 100 \text{ GeV}$ $E_{el} > 4 \text{ GeV}$ *Boxcut* $12 \times 12 \text{ cm}$

DIS03 → *medium* Q^2 , *Boxcut*

DIS04 → *high* Q^2

EX07 → *high* Q^2 *NC*

4.3.2 Kinematics cuts

- As a first step we require a primary vertex that must be reconstructed using CTD tracks. Such a vertex must be close to the nominal interaction point, i.e. the z coordinate $|z_{vtx}| < 30 \text{ cm}$;
- another essential issue is to reject background events, the most important being the requirement of longitudinal event containment. By energy-momentum conservation, the final state of any ep reaction has $E - p_z = 2 \cdot E_e = 55 \text{ GeV}$. The measured quantity (see Sec. 3.3) is

affected by experimental resolution and by particles which escape detection. In particular the requirement of a minimum measured value, allows to reject events with significant energy flow into the rear beam hole and thus to remove most of photoproduction background (where the electron is scattered at large values of θ_e and it escapes the detector through the rear beam pipe), events with undetected high-energy QED Initial-State Radiation or with proton beam gas. At the level of the offline selection a more precise estimation of δ is obtained using the ZUFOS and the electron candidate:

$$E - p_z = \delta_{had} + \delta_{el} \quad (4.4)$$

$$= \sum_{i \in ZUFOS}^N E_i(1 - \cos \theta_i) + E'_e(1 - \cos \theta_e) \quad (4.5)$$

In Eq. 4.5 the sum runs over the N reconstructed ZUFOS. To select DIS NC events δ is required to be

$$40 \text{ GeV} < E - p_z < 80 \text{ GeV}. \quad (4.6)$$

The upper cut is introduced to remove residual cosmic ray background, and also to remove events with an overlap between beam-gas events and physics ep scatterings.

- To select a sample with a reliable measurement of the kinematic variables, an EM electron has to be found, meeting the following requirements to ensure high purity and to reject background:
 - EM probability > 0.001 ;
 - the electron should be isolated such that the energy in an $\eta - \phi$ cone of radius 0.8 centered on the electron, but not associated with it, is less than 5 GeV.

$$E_e'^{CONE} < 5 \text{ GeV} \quad (4.7)$$

- $E'_e > 10 \text{ GeV}$
- if $\theta_e < 2.5 \text{ rad}$, we need further cuts for strongly deflected electron:
 - within good CTD acceptance, $\theta > 0.6$, we require an associated track with $DCA < 10 \text{ cm}$, $NSL \geq 4$, $p_{track} > 5 \text{ GeV}$
 - for $\theta < 0.6$, we select events with $P_T^e > 25 \text{ GeV}$
- we apply a cut on Q_Σ^2 higher than the cut applied on MC at generation ($Q_{DA}^2 > 15 \text{ GeV}^2$):

$$Q_\Sigma^2 > 20 \text{ GeV}^2; \quad (4.8)$$

- to remove respectively the remaining photoproduction events with fake, low-energy forward electron candidates and events where the hadronic system is not well reconstructed in the forward region:

$$y_{el} < 0.95 \text{ and } y_{JB} > 0.02; \quad (4.9)$$

- to remove charged current events, cosmic-ray events and beam related background events

$$P_{T,miss}/E_T < 0.7. \quad (4.10)$$

In the Fig. 4.1 we show some control plots after the DIS selection.

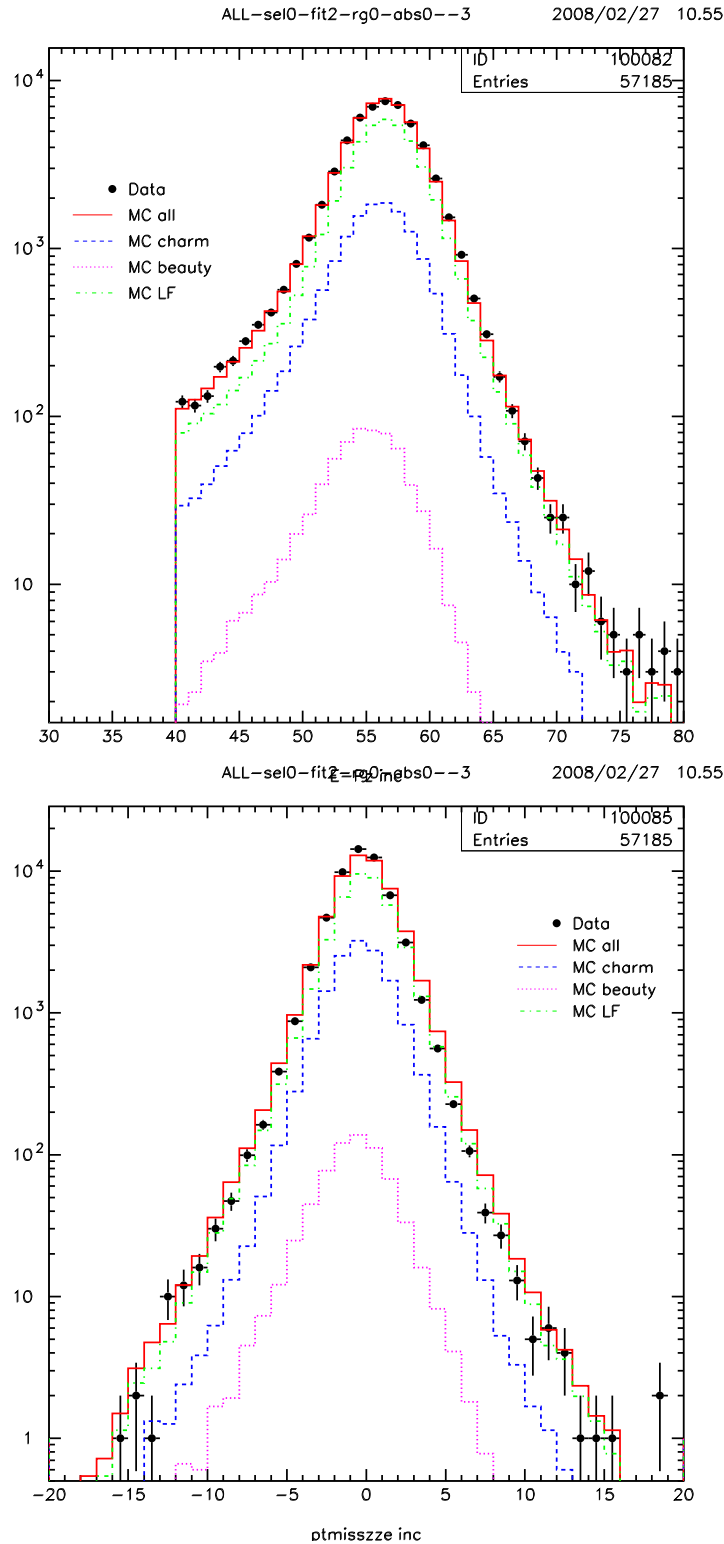


Figure 4.1: Distribution of $E - P_z$ and $(P_T^{miss} \cdot P_T^c) / |P_T^c|$ of the inclusive sample after DIS selection. The black dots represent 2005 data; the green dashed line the Ariadne MC from light flavours; the blue and pink lines represent respectively charm and beauty Rapgap MC samples. The histograms are normalized to data luminosity.

4.4 Background sources

4.4.1 Heavy Vector Meson Decays

Muon pair production from the decay of heavy vector mesons, in particular the process $J/\Psi \rightarrow \mu^+\mu^-$, has to be considered as a background source. In contrast to semi-muonic hadron decays, however, all hadronic activity is due to the underlying event and is not directly connected to the decay itself. The anti-isolation cut we have done (see section 4.5.1) removes elastic J/Ψ . There is still part of the inelastic J/Ψ background, that could pass our anti-isolation cut. A study for this kind of decays has been done selecting events with two "good" muons in the final sample after the full selection (see Sez. 4.7). We calculated the invariant mass of the two muons and we found a peak for an invariant mass $\simeq m(J/\Psi)$ (see fig 4.2). This peak was used to normalize the Cascade Monte Carlo [74] that describes very well the inelastic J/Ψ in DIS [75]. From Cascade we realized that the contamination of muons from J/Ψ in the final inclusive sample was $\sim 0.1\%$ and could be neglected. Anyway, in case of two muons satisfying our requirements, we look at the invariance mass of the two tracks associated to the muons, rejecting the J/Ψ peak.

4.4.2 Cosmic Muons

High-energy muons from cosmic-rays (cosmic muons) penetrate the outer detector shielding at a rate of about 1 kHz. If a cosmic muon crosses the central detector region close to the nominal interaction point then it can be mis-interpreted as an ep event with one or two identified muons in the final state. There is, however, no timing correlation with the colliding HERA beams. Cosmic muons are thus in general isolated with little additional detector activity and, therefore, do not fulfill the requirement of the anti-isolation cut (see section 4.5.1). Only in rare cases where a cosmic muon is recorded at the same time as an ep event (overlay event) might the final state topology be similar to a semi-muonic heavy flavour decay. The background from this source was found to be negligible.

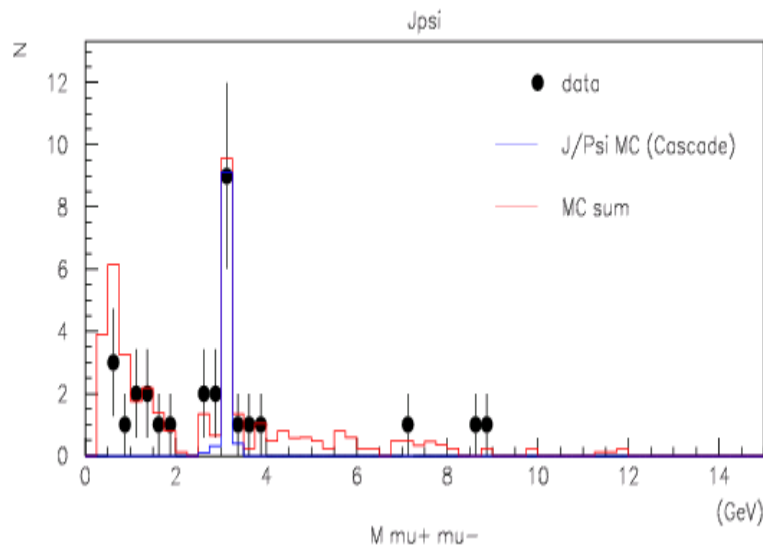


Figure 4.2: Invariant mass of a two muon sample passing our selection. Adding the inelastic J/Ψ Cascade MC (blue line) to our inclusive Ariadne MC, we get a total MC (red line) that agrees perfectly with data. The histogramms are normalized to data luminosity.

4.4.3 Background from mis-identified hadrons

In this analysis, muon identification is based on a signal in the muon chambers, beyond the calorimeter. All other detectable particles are expected to be stopped within the calorimeter. Hadrons coming from the interaction region, however, also produce in rare cases a signal in the muon system. In this way any process producing one or more jets and including, high P_T hadrons might contribute to the signal sample. A dedicated study ([73]) showed that such hadrons, mainly kaons and pions, have a probability of 1% to reach the internal muon chambers and to be reconstructed as a muon. The probability goes down to 0.1% if we require a hit in the external chambers as well. Nevertheless, since they are produced in large numbers in ZEUS events, some of them can actually give a wrong signal in the muon chambers (*fake muons* or *mistag*). It should be noted that, while a muonic background can be associated to a specific physics process which can be studied separately using dedicated Monte Carlo event samples, this in general is not the case for fake muons. The fake muons could be classified as :

- *punch-through*: hadrons passing through the calorimeter can interact and produce secondary particles that hit the muon detectors; this source of background is reduced by requiring a good position (and momentum) matching between the segment in the muon detector and the CTD/MVD track;
- *sail-through*: in some cases, hadrons can pass through the whole detector without being stopped, and then reach the muon chambers being mistagged as muons;
- *decay in flight*: muons can come from particle decays, like $\pi^\pm \rightarrow \mu^\pm \nu$, or $k^\pm \rightarrow \mu^\pm \nu$. Such muons typically have low momenta and therefore the request for a hard muon reduces this kind of background. This background is the most relevant for muons that reach the external chambers.

The procedure used in this analysis to quantify the fraction of light quark events in the final data sample will be explained in detail in Chapter 5.

4.5 Muon selection

For this analysis a smart muon selection is essential to gain a high selection efficiency. The detector is divided into three regions of pseudo-rapidity $\eta = -\log(\tan \frac{\theta}{2})$:

$$\begin{aligned}
 \textit{Rear} & \quad (-1.6 \leq \eta < -0.9) \\
 \textit{Barrel} & \quad (-0.9 \leq \eta < 1.3) \\
 \textit{Forward} & \quad (1.48 \leq \eta < 2.3)
 \end{aligned}$$

We require at least one muon candidate found by BREMAT in the rear/barrel region or one candidate found by MPMATCH in the forward part.

BREMAT

In Bremat matching package (see section 3.6.1) tracks are labeled as "muons" when they are matched to a reconstructed segment in the inner muon chambers. This program performs an outward extrapolation of inner tracks taking into account the detailed distribution of materials and the magnetic field in ZEUS. The matching is based on the comparison between the position and orientation of the extrapolated track and those of the reconstructed segment (*4 d.o.f. matching*) in the inner or outer muon chambers (see section 3.6.1). When an outer segment is also reconstructed it is possible to include in the matching probability parameter the momentum as it is measured by the inner tracking devices and the muon chambers (*5 d.o.f. matching*). In this analysis the 4 d.o.f. selection will be used; this kind of selection allow us to have much more statistics and at the same time there is no significant reduction of the ratio signal/background with respect to the 5 d.o.f. selection. We selected a region where the muon detector efficiency is known with a relatively small uncertainty and the data/MC ratio is flat [89]:

- match probability, $P_{4d.o.f.}^{BREMAT} > 0.01$;
- muon transverse momentum, $p_T^\mu > 1.5 \text{ GeV}$;
- muon pseudorapidity, $-1.6 < \eta_\mu < 1.3$.

The cut in the probability of the matching at 0.01 was chosen since matchings with lower probabilities are dominated by fake muon (see section 4.4.3).

The cut on transverse momentum is motivated by the fact that prompt muons, especially from heavy quarks, have a harder p_T spectrum. Furthermore it is clearly seen from dimuon samples that at lower values of p_T , due to the CAL material absorption, the efficiency is rather low.

The angular cut almost coincides with the geometrical coverage of the BRMUI detector. The requirements on matched tracks are those imposed by the BREMAT algorithm in Section 3.6. In addition, in order to suppress

the occurrence of matches from secondary muons, we required the candidate tracks to be associated to the primary vertex (VCTPAR ADAMO table).

MPMATCH

In the forward region, muons are required to reach the outer FMUON chambers, and the momentum to be reconstructed by both the CTD and the muon detector. The muon momentum is included in the fitting parameters when the CTD track is matched to the FMUON track. The forward muon track (from the table MFRTZ) is required to satisfy the following requests:

- χ^2 probability from the Kalman fit $P_{mfrtz} > 0.05$;
- number of degrees of freedom in the Kalman fit $NDOF(mfrtz) > 1$, which is equivalent to require hits in at least 3 FMUON planes;
- the track starts in the inner FMUON planes, that means $Z_{mfrtz} < 500$ cm

In this way, background due to spurious hits originating from lepton *bremsstrahlung* or secondary particles from the proton or noise are strongly reduced. Moreover, the quality of the fit is significantly increased by requiring the first hit in the internal FMUON planes which are closest to the CTD.

- MFRTZ tracks are back extrapolated with the GEANE package to the FCAL face. A χ^2 match in 5 variables, $x, y, dx/dz, dy/dz, q/p$ is performed between FMUON and CTD tracks extrapolated to the same reference plane.
- An additional cut has been imposed on the matching probability of the MPMATCH fit in order to reject background from fake muons:

$$P_{match}^{MPMATCH} > 0.05 \quad (4.11)$$

- The FMUON performances have been studied in detail [72] using an independent sample of dimuon events. The detector efficiency has been evaluated on the data and on the Monte Carlo simulation and the ratio between the two used as a correction factor for the cross section. From the studies in [72], a region where the FMUON efficiency is known with sufficient precision and the data/MC ratio is flat is defined as:

$$p^\mu > 4 \text{ GeV} \quad , \quad p_T^\mu > 1 \text{ GeV} \quad (4.12)$$

$$1.48 < \eta^\mu < 2.3. \quad (4.13)$$

4.5.1 Anti-isolation cut

The *anti-isolation* cut selects muons with a minimum energy in an $\eta - \phi$ cone of radius 1. around the muon flight direction, excluding the energy coming from the muon itself. This energy (E_μ^{iso}) has to be greater than 0.5 GeV.

This cut removes most of the background coming from processes that produce isolated muons: elastic J/Ψ , elastic and quasi-elastic Bethe-Heitler ($\gamma\gamma \rightarrow \mu^+\mu^-$) QED events and cosmic rays crossing the detector.

In figure 4.3 the distribution of (E_μ^{iso}) is shown for DATA and MC. The peak around 0 GeV is greater in Data with respect to MC sample, where processes with isolated muons were not included. Anyway, after the cut, the inclusive MC sample seems to describe well this variable.

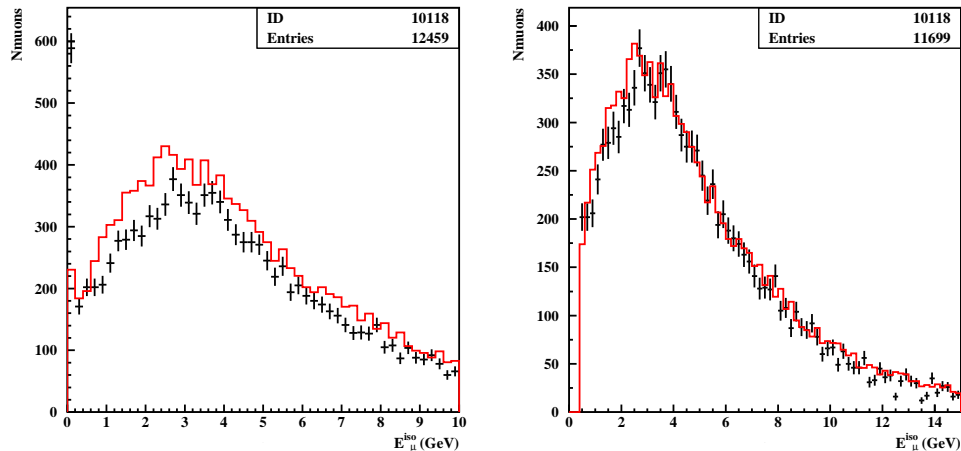


Figure 4.3: Distribution of E_{μ}^{iso} , the energy in an $\eta - \phi$ cone of radius 1. around the muon direction before (left) and after (right) the cut at 0.5 GeV. The MC inclusive sample (red histogram) and the data points (black dots) are area normalized.

4.6 Jet Selection

We required very loose cuts on the jet variables because we don't want to measure a jet-related cross section. We just want to have a jet associated to the muon, that can be used as reference direction of the struck quark, to calculate the variables p_T^{rel} , the momentum of the muon transverse to the axis of the associated jet and δ , the signed impact parameter of the track associated to the muon. The jet selection requires as first step at least one jet in the laboratory frame with the massive scheme (see sect. 3.5). In addition a jet has to be associated to the muon we have selected: the ZUFO associated to the muon has to be included into the jet reconstruction by the k_T algorithm. A check of this association has been done looking if the associated jets lay close to the muon, within a cone of radius 1 in $\eta - \phi$ phase space (see figure 4.4).

Moreover we required the transverse momentum of the jet, p_T^{jet} , to be greater than 3 GeV and the pseudo-rapidity in the range of $-3 < \eta^{jet} < 3$.

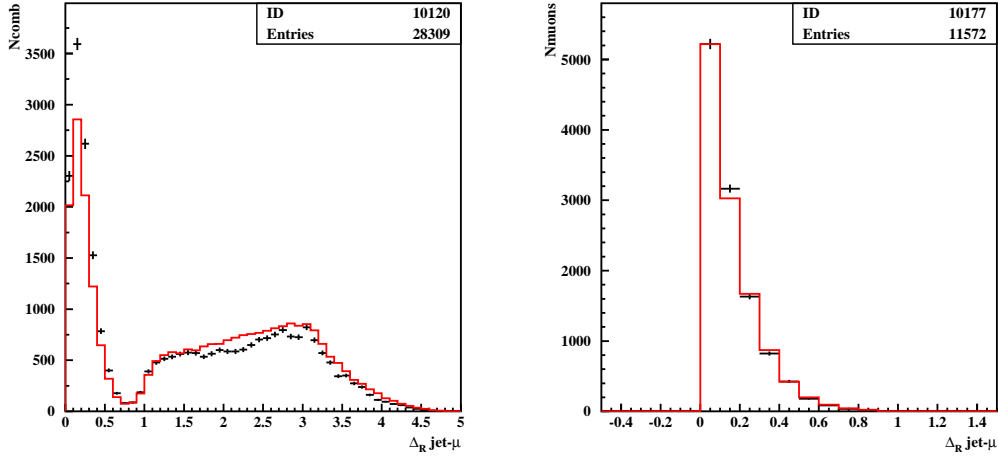


Figure 4.4: Histograms of the distance Δ_R in the $\eta - \phi$ phase space between a selected muon and jets before (left) and after (right) requiring the muon-jet association via ZUFOS k_T algorithm. The second plot is referred to a sample with more statistics, but we are interested to see the change of the shape of the distribution. The MC inclusive sample (red histogram) and the data points (black dots) are area normalized.

4.7 Final selection and control plots.

Summarizing the complete selection, events from the data and MC samples are required to fulfil the following cuts:

4.7.1 DIS selection

- SPP01.or.SPP02.or.DIS03.or.DIS04.or.EX07;
- $40 \text{ GeV} < E - P_z < 80 \text{ GeV}$;
- $|Zvtx| < 30 \text{ cm}$;
- $EM_{prob} > 0.001$;
- $E_e^{'CONE} < 5 \text{ GeV}$;
- $E_e' > 10 \text{ GeV}$;
- if $\theta_e < 2.5 \text{ rad}$,

- within CTD acceptance we require an associated track with $DCA < 10$ cm, $NSL \geq 4$, $p > 5$ GeV
- out of CTD acceptance, $\theta < 0.6$, we require $P_T^e > 25$ GeV
- $Q_\Sigma^2 > 20 \text{ GeV}^2$;
- $y_{el} < 0.95$ and $y_{JB} > 0.02$;
- $P_{T,miss}/E_T < 0.7$.

4.7.2 Muon selection

At least 1 muon, coming from primary vertex, with the following characteristics:

REAR/BARREL muon

- $P_{4d.o.f.}^{BREMAT} > 0.01$
- $p_T^\mu > 1.5$ GeV
- $-1.6 < \eta_\mu < 1.3$

FORWARD muon

- $P_{5d.o.f.}^{MPMATCH2} > 0.05$
- $P^\mu > 4$ GeV and $P_T^\mu > 1$ GeV
- $1.48 < \eta^\mu < 2.3$

Anti-isolation cut

- $E_{iso}^\mu > 0.5$ GeV

4.7.3 Jet-Muon association

A jet with the following characteristics has to be associated to the muon via ZUFOS k_T algorithm:

- $P_T^{jet} > 3 \text{ GeV}$
- $-3 < \eta^{jet} < 3$

4.7.4 Additional cuts

- *Inv. Mass.:* in order to reject events with many segments from R/BMUON that reconstruct more than one muon almost in the same direction and with the same momentum.
- *Track quality:* in order to reconstruct a track with good quality we required at least 4 hits on Barrel MVD. This cut has been applied only to tracks associated to muons in R/Bmuon detectors. For the forward zone there are no MVD requirements on the track because the alignment in the forward MVD (wheels) was not yet ready.

4.7.5 Control plots

A table of the cut incidences, considering as starting sample the basic DIS plus Muon selection is shown in Tab 4.2. The importance of the cuts is comparable between DATA and MC, but:

the anti-isolation cut, where the reduction factor is bigger for DATA than for MC as expected because of the different background contamination of the initial samples;

the track quality cut, due to the inefficiency of the tracking system that is not simulated in the MC. Some of these cuts will be treated in detail in Chapter 5 and differentiated as systematics check.

The final DATA sample has **1505** muons in REAR zone, **9597** in BARREL zone and **245** in FORWARD region. In the last case, we applied a very

Selection	N_{events}	Cut incidence (% diff)			
		DATA	MC		
			Light Fl.	Charm	Beauty
DIS.and. μ Selection	14666				
$E_{\mu}^{iso} > 0.5$ GeV	13564	-7.5	-4.6	-2.7	-3.7
μ from prim. vtx	12444	-8.3	-9.1	-5.2	-5.4
Association Jet- μ	12440	-0.03	-0.02	-0.006	-0.007
$P_T^{Jet} > 3$ GeV	11693	-6.00	-6.6	-6.5	-7.5
InvMass(di-mu)>1 GeV	11347	-2.9	-2.7	-2.9	-2.6
# MVD hits > 4	10042	-11.5	-6.9	-6.6	-6.8

Table 4.2: Cut incidence for DATA and for different kinds of Monte Carlo.

tight cut on the number of planes of FMUON to reduce the backgrounds. The total number of events available to extract the signal is **11347**. In case we want to use the impact parameter, a further cut is applied and the sample restricts to **10042** events.

Concerning MC, after the selection, we remain with 67422 Light flavour events, 30120 of Charm and 36692 from Beauty. Obviously, they correspond to different luminosities but what is important, is the overall number of events from MC we are going to use to fit our DATA sample.

Control distributions of the kinematic, muon, jet and tracking variables after the selection are shown in Fig.4.5-4.10. In all cases, the charm (blue line), beauty (pink line) and light flavour (green line) Monte Carlo samples are scaled to data luminosity using their nominal cross sections and than added to be compared to the data sample.

In fig. 4.5 the z-coordinate of the vertex is shown, where is clearly visible the cut at 30 cm. Below we see the $E - P_z$ distribution, very well reproduced, in which we don't detect any photoproduction background.

The electron variables are presented, θ_e and E'_e , in fig. 4.6. The first one is quite well reproduced; in the electron energy distribution there is slight difference in the shape but the agreement is still acceptable.

In fig. 4.7 we find the kinematic variables used to classify our event, X_Σ , Y_Σ and Q_Σ^2 . Even in this case the distributions are quite well reproduced, except the Y variable that differs in some bin but is acceptable.

In fig. 4.8 the muon-variables are shown; the matching probability $Prob_\mu$ of the BREMAT package for BMUON has a peak at 0, that in part has already been reduced by the cut at 0.01. The spectra of P_T^μ in REAR and BARREL are also shown and are very well reproduced; in the logarithmic scales we see that the tails of the distribution agree as well.

A very interesting variable is η_μ , that is presented in fig. 4.9 for REAR, BARREL and FORWARD regions. In this case we don't have a perfect agreement; it could be due to the inability of the mixed Ariadne(lf) and Rapgap (c and b) MC to reproduce the angle of quarks getting out of the hard scattering.

The jet-related variables (η^{jet} and p_T^{jet}) and the energy around the muons (E_μ^{iso}) are shown in fig. 4.10 and they agree very well with our MC mix. In particular, looking at the distribution of (E_μ^{iso}), we see that the muons are "more isolated" in the REAR than in the BARREL.

In general, a reasonable agreement between data and Monte Carlo simulation is observed.

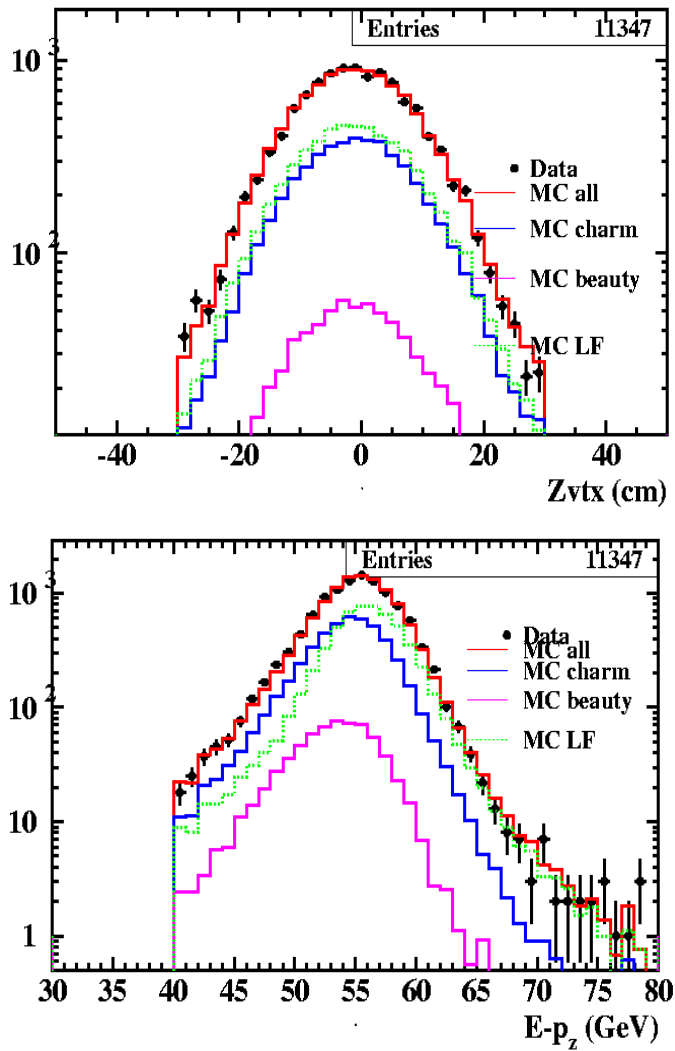


Figure 4.5: Control plots for $Zvtx$ and $E - p_z$. In all the plots the data (dots) are compared to the inclusive MC distribution (red line) obtained by summing the beauty (pink line), charm (blue line) and light flavour (green line) contributions according to the MC cross sections. The MC sum was normalized to the DATA. The Rapgap MC for charm and beauty, Ariadne MC for light flavours have been used.

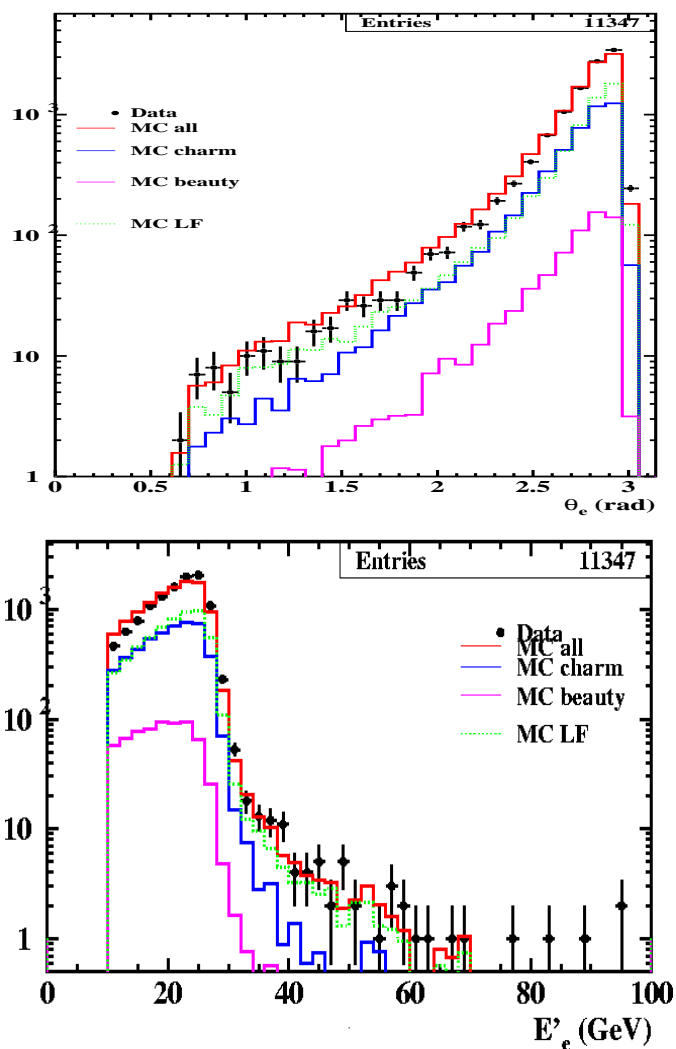


Figure 4.6: Control plots of θ_e , E_e . In all the plots the data (dots) are compared to the inclusive MC distribution (red line) obtained by summing the beauty (pink line), charm (blue line) and light flavour (green line) contributions according to the MC cross sections. The MC sum was normalized to the DATA. The Rapgap MC for charm and beauty, Ariadne MC for light flavours have been used.

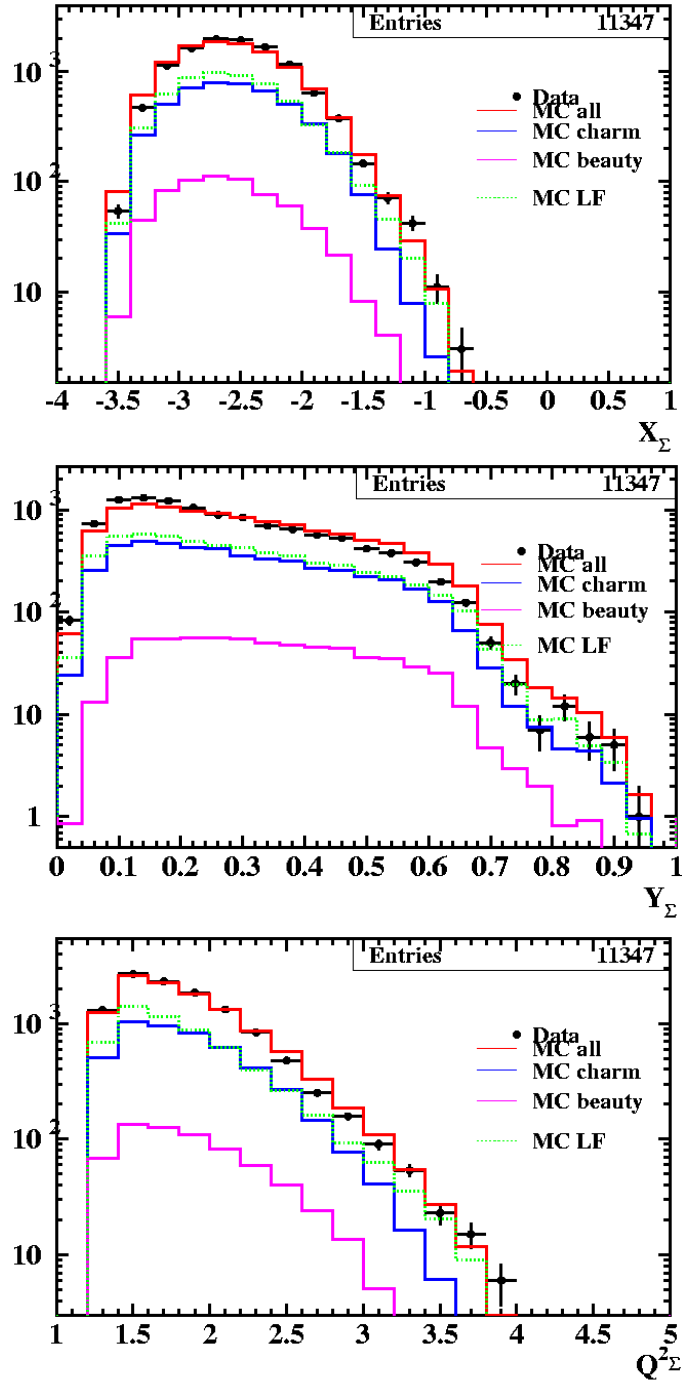


Figure 4.7: Control plots for Q^2_Σ , X_Σ , Y_Σ of the events. In all the plots the data (dots) are compared to the inclusive MC distribution (red line) obtained by summing the beauty (pink line), charm (blue line) and light flavour (green line) contributions according to the MC cross sections. The MC sum was normalized to the DATA. The Rapgap MC for charm and beauty, Ariadne MC for light flavours have been used.

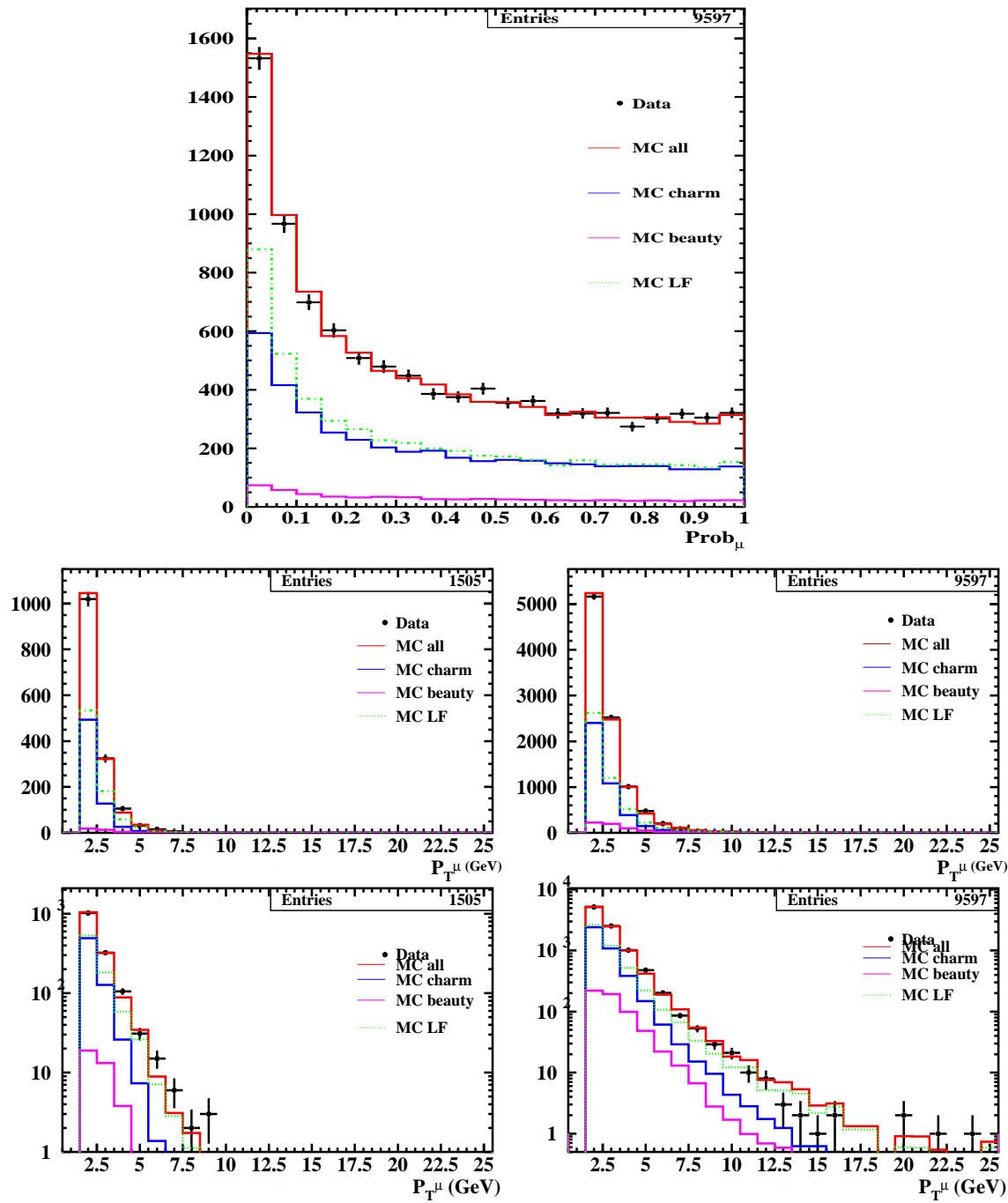


Figure 4.8: BREMAT Matching $Prob_\mu$ (above) and P_T^μ spectra (below) of the muon after the selection. On the left side relative to the Rear muon; on the right side to the Barrel muon. The spectra are shown in linear (top) and in logarithmic (bottom) scales. In all the plots the data (dots) are compared to the inclusive MC distribution (red line) obtained by summing the beauty (pink line), charm (blue line) and light flavour (green line) contributions according to the MC cross sections. The MC sum was normalized to the DATA. The Rapgap MC for charm and beauty, Ariadne MC for light flavours have been used.

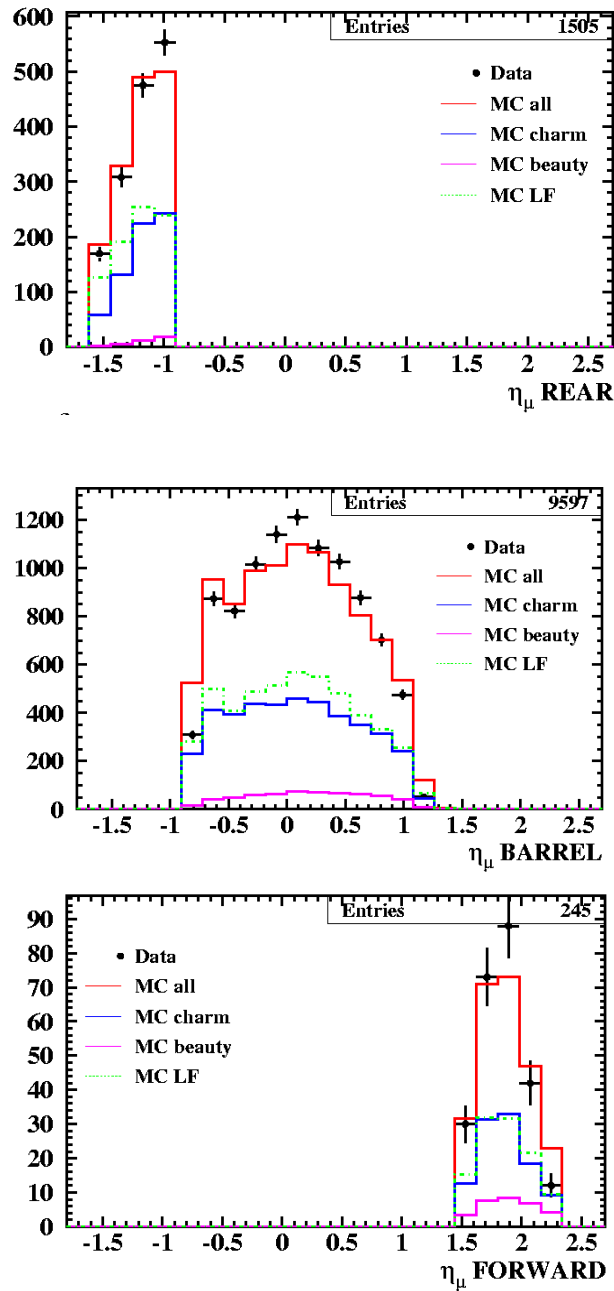


Figure 4.9: η^μ distribution of the muon after the selection. On the top relative to the Rear muon; on the center to the Barrel and on the bottom to the Forward muon. In all the plots the data (dots) are compared to the inclusive MC distribution (red line) obtained by summing the beauty (pink line), charm (blue line) and light flavour (green line) contributions according to the MC cross sections. The MC sum was normalized to the DATA. The Rapgap MC for charm and beauty, Ariadne MC for light flavours have been used.

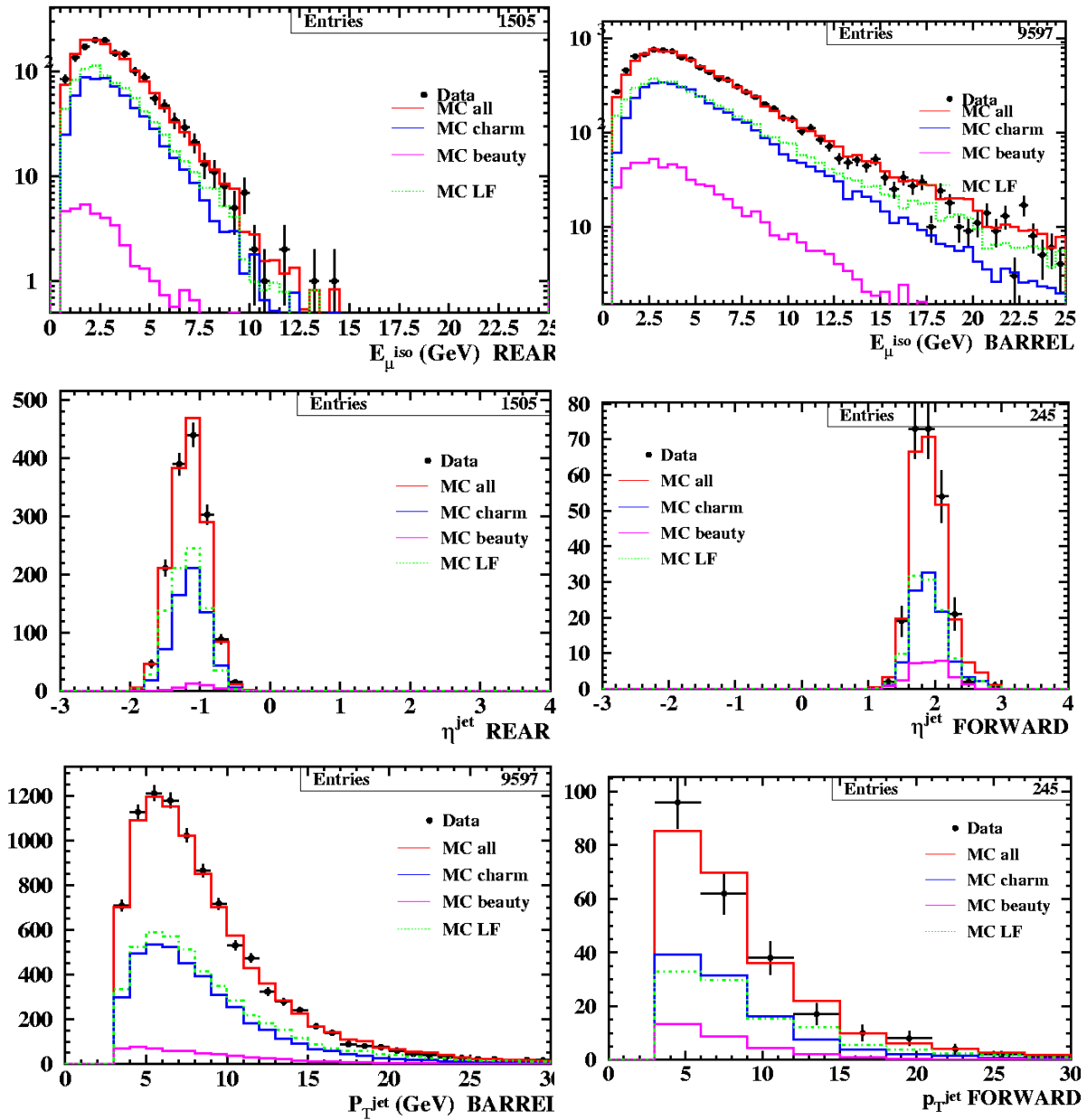


Figure 4.10: E_{μ}^{iso} , η^{jet} and P_T^{jet} . In all the plots the data (dots) are compared to the inclusive MC distribution (red line) obtained by summing the beauty (pink line), charm (blue line) and light flavour (green line) contributions according to the MC cross sections. The MC sum was normalized to the DATA. The Rapgap MC for charm and beauty, Ariadne MC for light flavours have been used.

4.8 Discriminating observables

To separate charm, beauty and light flavours discriminating variables can be used.

4.8.1 P_T^{rel}

While the muon momentum component parallel to the flight direction of the parent hadron also depends on the hadron production kinematics, the transverse momentum of the decay muon relative to the hadron direction,

$$P_{T,true}^{rel} = |\vec{P}_{T,true}^{rel}| = \left| \frac{\vec{P}_{T,true} \times \vec{P}_{hadron}}{\vec{P}_{hadron}} \right|, \quad (4.14)$$

reflects the hadron mass in a direct way. In fact the P_T^{rel} true distribution is closely related to the muon momentum spectrum in the rest frame of the decay hadron, the kinematic end point being the same for both quantities (see fig. 4.11). This results in clearly different spectra for beauty and charm or light flavour decays (Fig. 4.12). The beauty distribution differs from charm and light flavours, that have a similar shape (Fig. 4.13 and 4.14). Approximating the hadron direction by a suitably defined jet-based reference axis, the corresponding experimental observable is defined as:

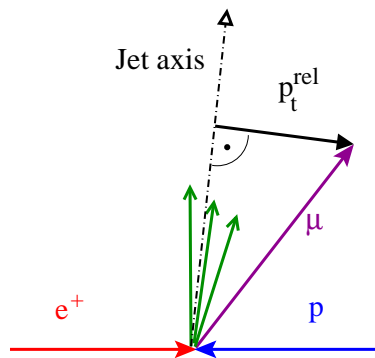


Figure 4.11: *The transverse muon momentum P_T^{rel} relative to an associated jet.*

$$P_T^{rel} = \frac{|\vec{P}_T^\mu \times \vec{P}_T^{jet}|}{|\vec{P}_T^{jet}|} \quad (4.15)$$

There is an alternative definition, used in other analysis, for this quantity where the muon transverse momentum is subtracted from the jet and the transverse momentum of the muon relative to the new jet axis, $P_T^{rel,jet-\mu}$, is calculated

$$P_T^{rel,jet-\mu} = \frac{|\vec{P}_T^\mu \times (\vec{P}_T^{jet} - \vec{P}_T^\mu)|}{|(\vec{P}_T^{jet} - \vec{P}_T^\mu)|} \quad (4.16)$$

. By subtracting the muon transverse momentum from the jet to form the new reference axis, the calculated $P_T^{rel,jet-\mu}$ spectrum is shifted to larger values. The characteristics of the $P_T^{rel,jet-\mu}$ shape with respect to the originating quark flavour remains the same as for the first definition.

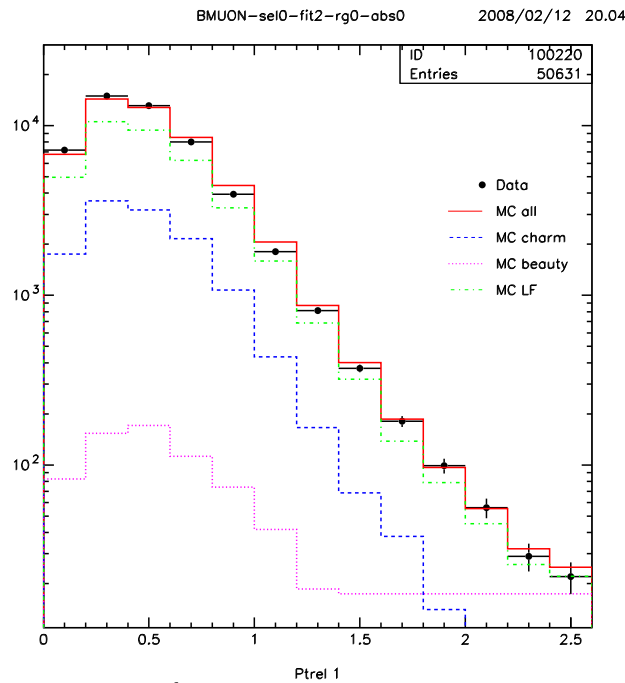


Figure 4.12: Distribution of p_T^{rel} of the inclusive track sample after the DIS selection. The black dots represent 2005 data; the green line the Ariadne MC from light flavours; the blu and pink lines represent respectively charm and beauty Rapgap MC samples. The histograms are area normalized.

p_T^{rel} corrections

As the p_T^{rel} distribution of the background is essential to calculate the heavy flavour fractions, investigations of the correct simulation of p_T^{rel} distributions have been conducted. We compared the p_T^{rel} distribution of any track passing the same track selection used for muons in an inclusive data sample with an inclusive MC from Ariadne. This inclusive track sample is dominated by light flavour. The p_T^{rel} distribution of light flavor events is slightly softer in MC than in data and a correction of the MC p_T^{rel} shape has to be applied. A detailed description of this correction will be given in Chap 5.

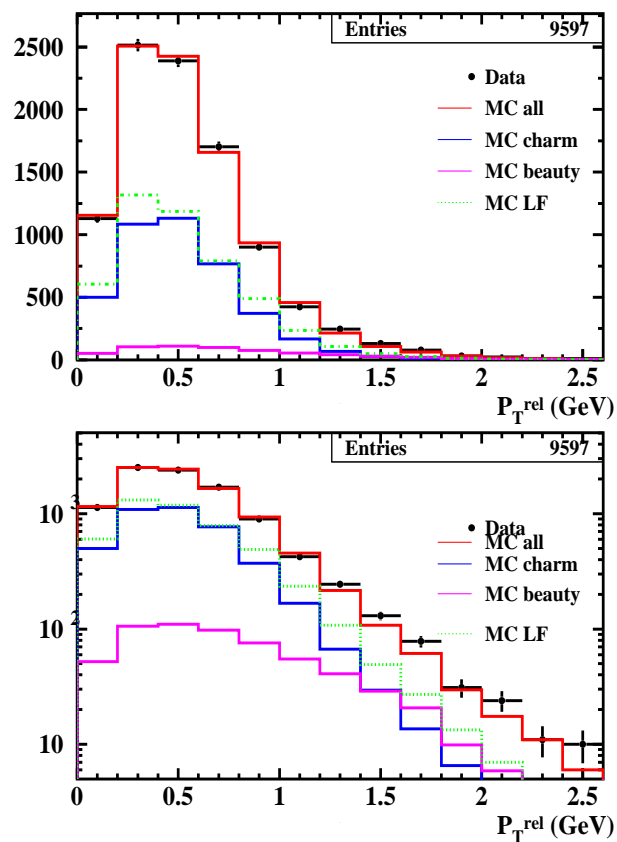


Figure 4.13: Barrel P_T^{rel} distributions in linear (upper) and in logarithmic (lower) scale after the correction. In all the plots the data (dots) are compared to the inclusive MC distribution (red line) obtained by summing the beauty (pink line), charm (blue line) and light flavour (green line) contributions according to the MC cross sections. The MC sum was normalized to the DATA. The Rapgap MC for charm and beauty, Ariadne MC for light flavours have been used.

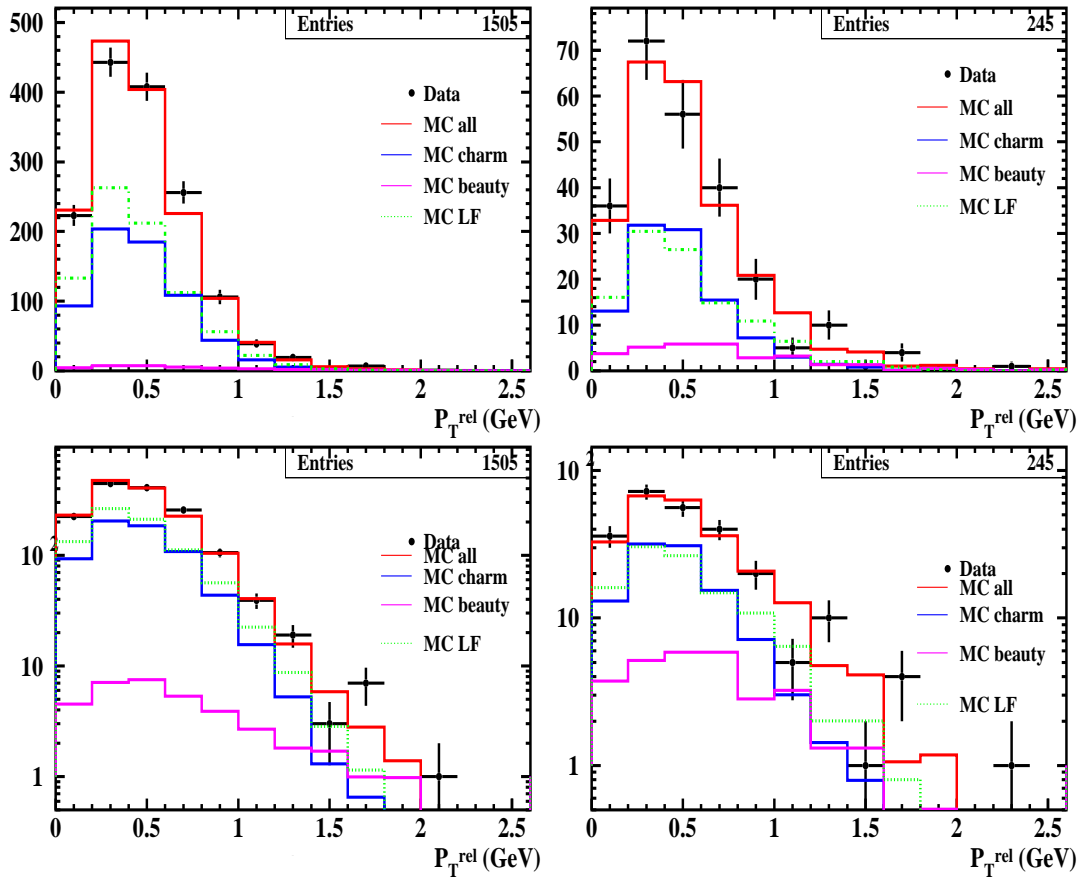


Figure 4.14: Rear (left) and Forward (right) P_T^{rel} distributions in linear (upper) and in logarithmic (lower) scale after the correction. In all the plots the data (dots) are compared to the inclusive MC distribution (red line) obtained by summing the beauty (pink line), charm (blue line) and light flavour (green line) contributions according to the MC cross sections. The MC sum was normalized to the DATA. The Rapgap MC for charm and beauty, Ariadne MC for light flavours have been used

4.8.2 Impact parameter

The large decay length of heavy flavour hadrons arising from their long lifetime can also be used to define sensitive observables. The decay length is strictly related to the lifetime in the rest frame of the decaying hadron; in the laboratory frame the decay length l , which is experimentally accessible, also depends on the hadron boost, $\beta\gamma = |p|/m$, via

$$l = c\tau\beta\gamma \quad (4.17)$$

The probability that an individual hadron of characteristic decay length l traverses at least a laboratory distance L between its production and decay is given by

$$P(L) = \exp(-L/l) \quad (4.18)$$

For experimental reasons, in this analysis, the lifetime information is extracted only in a plane perpendicular to the beam axis. Therefore, only the $r\phi$ -projection

$$L_t = L \sin \theta \quad (4.19)$$

where θ denotes the polar angle of the decaying hadron, is relevant here. The *impact parameter* of a particle coming from the hadron decay is the closest distance in the xy plane, between the decay particle's trajectory and the production point of the decaying hadron and is given by

$$I.P._{true} = L_t \sin \alpha \quad (4.20)$$

Here α is the angle in the xy plane between the hadron direction and the direction of the decay particle. The factor $\sin \alpha$ approximately compensates the boost dependence of L_t .

The lifetime difference between charm and beauty flavoured hadrons leads to significantly different decay muon $I.P._{true}$ spectra, the large $I.P._{true}$ region is dominated by beauty events. In order to reconstruct an experimental observable corresponding to $I.P._{true}$, the hadron production vertex is taken

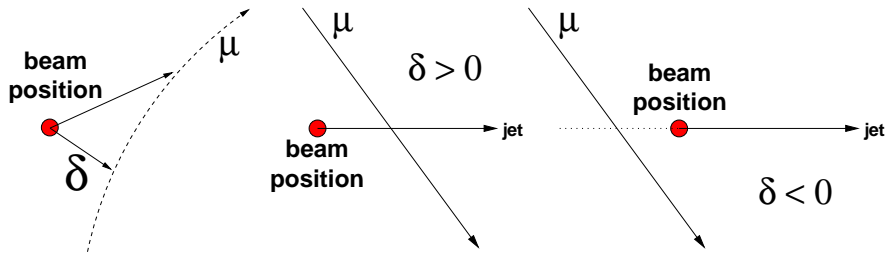


Figure 4.15: Sketch of the impact parameter, δ , of a muon track. If the muon track intercepts the jet axis downstream the primary vertex (beam position, see Chapter 3) the impact parameter has positive sign, otherwise it is negative.

to be the interaction point in beam spot (see Chapter 3) and the flight direction of the decaying hadron is approximated by a jet-based reference axis as already discussed for the p_T^{rel} in the previous subsection. While $I.P_{true}$ is by definition a positive quantity, it turns out to be useful to define a sign for the corresponding experimental observable. The resulting *signed muon impact parameter*, δ , is defined as follows:

- The magnitude of the impact parameter is given by the $r\phi$ distance of closest approach of the reconstructed muon track to the reconstructed beam spot, $|DCA|$ (see Fig. 4.15).
- In order to give a sign to the DCA quantity the muon track is associated to the nearest jet; the sign is positive if the intercept of the muon track with the jet in the $r\phi$ projection is downstream of the primary vertex, and negative otherwise (see Fig. 4.15).

For muons originating from the primary vertex the δ spectrum will be symmetric around zero, the width of the distribution reflecting the finite track and vertex reconstruction resolutions. Decays of long-lived particles are characterised by an excess at positive δ values. The region at large positive impact parameters is expected to be dominated by muons from heavy flavour decays.

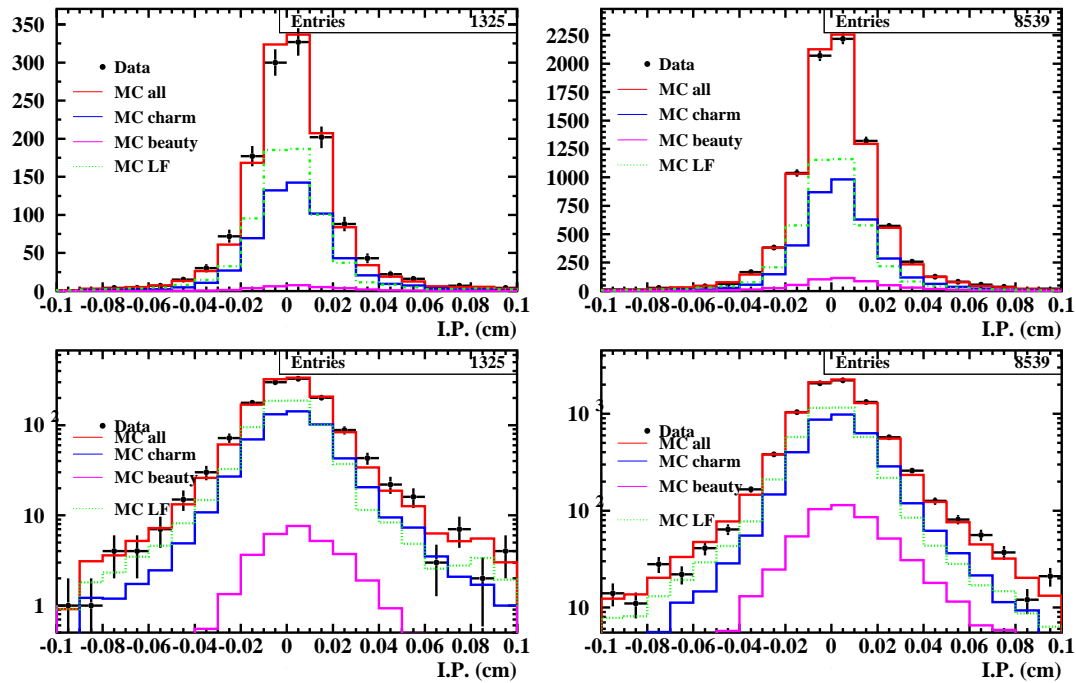


Figure 4.16: δ distributions after the smearing (see sect. 4.8.2). The black dots represent data; the green line the light flavour Ariadne MC; the blue and pink lines represent respectively charm and beauty Rapgap MC samples. The plots are normalised using luminosity from MC samples.

The impact parameter method is based on the reconstruction of the muon track and the event primary vertex which is assumed to be the production vertex of the heavy hadron. In contrast to an explicit decay length analysis, no knowledge of the hadron decay vertex is required and, therefore, a reconstruction of secondary event vertices is not necessary. Moreover the impact parameter depends only weakly on the boost of the decaying hadron.

As already mentioned in section 3.4.2 the δ resolution is wider in DATA than in MC. Even if very important improvements has been made on tracking system we needed to apply a *smearing* of our MC distribution. This technique will be describe in the following section, and has been already tested in other ZEUS analyses [].

I.P. smearing

A 2005 inclusive sample of dijet events was selected with standard photo-production analysis cuts, but omitting muon requirements (and muon triggers). PHP events are selected with 2 high Pt jets in the final state, and all tracks in the sample have to fulfil the following quality cuts:

- Number of CTD SL crossed ≥ 3 .
- Number of MVD clusters used in the track reconstruction ≥ 4 .
- $P_T > 0.5$ GeV.

The tracks are associated with the closest jet cutting on the variable "delta R". The resolution of the tracking system can be expressed as a function of the P_T of the track therefore it is useful to analyse the impact parameter spectrum in different P_T bins. In fig. 4.17 the distribution of the MC impact parameter is compared with all of the 2005 data sample in different P_T bins, from 0.5 to 5.0 GeV. In every bin the data δ distribution is significantly wider than in the MC. In order to determine the correct smearing to apply to the MC, different functional forms (e.g. Gaussian, double Gaussian, Breit-Wigner, convolution of Gaussian with exponential) were fitted to the negative side of the data distribution (the total distribution is slightly asymmetric towards positive values due to physics processes like K decays). The best fit to the data is found to be a double convolution of MC with a Gaussian and a Breit-Wigner:

$$F^2(x) = \int dy \int dz F(z) \mathbf{B}(y - z) \mathbf{G}(x - y) \quad (4.21)$$

where B indicates the Breit-Wigner function and G is the Gaussian function. In order to determine the precise values for the widths of the two distributions, different combinations of the σ of the Gaussian and the Γ of the Breit-Wigner distributions were tested in order to find the minima of χ^2 fits. The minima were determined considering 2-dim. distributions; the

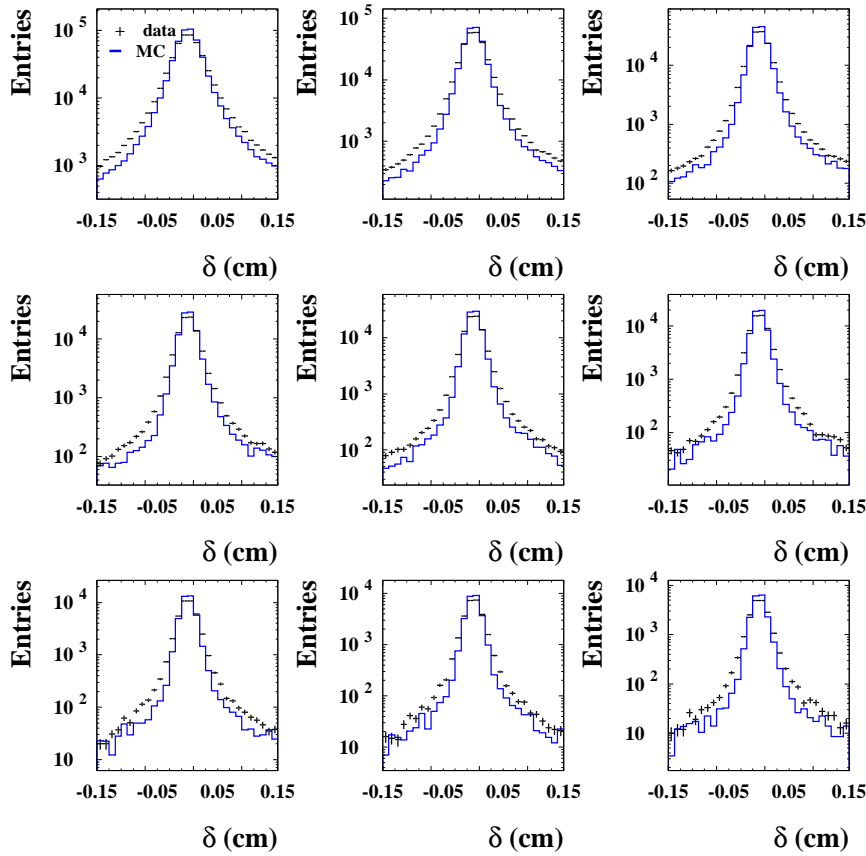


Figure 4.17: The MC impact parameter distributions compared with 2005 data (black crosses), in different P_T bins (the P_T range considered is $0.5 < P_T < 5$ GeV, the P_T bin size is 0.5 GeV) before smearing

χ^2 of the fit was plotted as a function of the Gaussian width keeping the gamma of the Breit-Wigner constant at its minimum. The Gaussian width was determined by fitting the local minimum area with a parabolic fit (same procedure for the other function). The distributions of the above parameters as a function of p_T , have been fitted using a combination of an exponential and constant function in the case of Breit-Wigner and a combination of a linear and constant function for the Gaussian; the results of the fit is:

$$\Gamma_{BW}(P_T) = \exp(a + b \cdot P_T) + c \quad (4.22)$$

$$\sigma_{GAUSS}(P_T) = d + e \cdot P_T \quad (4.23)$$

where the Breit-Wigner parameters are $a = 1.9791$, $b = -0.83335$ and $c = 2.3414$ cm, whilst the Gaussian fit parameter are $d = 0.0037817$ cm and $e = 0.00039859$ cm/GeV⁻¹. Here Γ and σ are expressed in cm and P_T in GeV. These values are used to correct the impact parameter measurements as follows

$$\delta_{smeared} = \delta_{original} + sme_{BW} + sme_{GAUSS} \quad (4.24)$$

where:

$$sme_{BW} = R_{RAN}^{BW} \times (\exp(a + b \cdot P_T) + c) \times const. : \quad (4.25)$$

and

$$sme_{GAUSS} = R_{RAN}^{GAUSS} \times (d + e \cdot P_T) \quad (4.26)$$

In Eq. 4.25 R_{RAN}^{BW} is a random number generated according to a BW distribution with $\Gamma = 1$ and $const.$ is equal to 0.001. In Eq. 4.26, R_{RAN}^{GAUSS} is a random number generated according to a Gaussian distribution with $\sigma = 1$. The same smearing parameters were applied to the muon Monte Carlo samples used for the analysis. In figures 4.17 and 4.18 we can see the different agreement without and with smearing respectively.

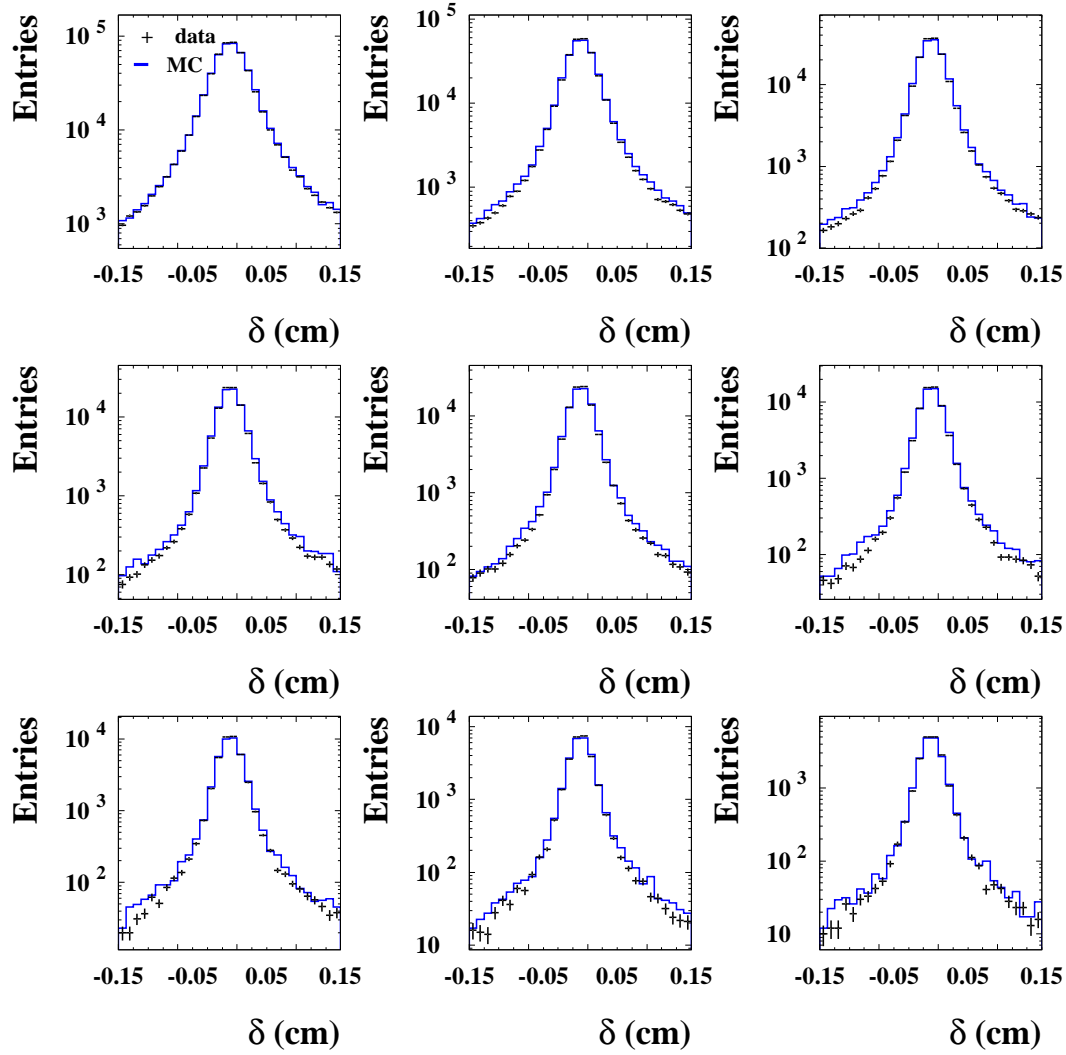


Figure 4.18: The MC impact parameter distributions compared with 2004 data (black crosses), in different P_T bins (the P_T range considered is $0.5 < P_T < 5$ GeV, the P_T bin size is 0.5 GeV) after having applied the δ smearing

4.8.3 The " $p_T^{\nu\|\mu}$ " method

When the heavy quarks decay semi-leptonically into muons, there is always a neutrino within the decay products. We expect that the neutrino goes approximately in the same direction of the muon; we can look at the component of the missing P_T parallel to the direction of the muon in the transverse plane defined as:

$$P_T^{\nu\|\mu} = \frac{\vec{P}_T^{miss} \cdot \vec{p}_T^\mu}{|\vec{p}_T^\mu|}. \quad (4.27)$$

This variable, except for the resolution effect, shows clearly (Fig. 4.19 and 4.20) an excess at positive values for the heavy flavour components.

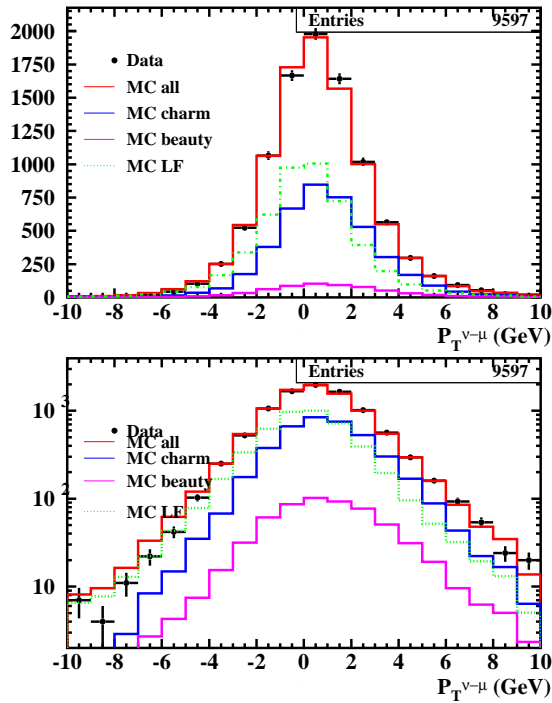


Figure 4.19: $P_T^{\nu\|\mu}$ distribution for Barrel muon detector. In all the plots the data (dots) are compared to the inclusive MC distribution (red line) obtained by summing the beauty (pink line), charm (blue line) and light flavour (green line) contributions according to the MC cross sections. The MC sum was normalized to the DATA. The Rapgap MC for charm and beauty, Ariadne MC for light flavours have been used.

This variable can give as an useful contribution to better estimate the heavy flavour fractions but we need a very good descriptions of the energy scales. The uncertainty of these scales, and the correction we applied to get a good simulation, will be explained in chapter 5. Nevertheless there are no special tracking requirements for this variable, and this is very usefull especially in forward zone where the impact parameter, as already mentioned, cannot be used because the tracking system is not yet fully understood.

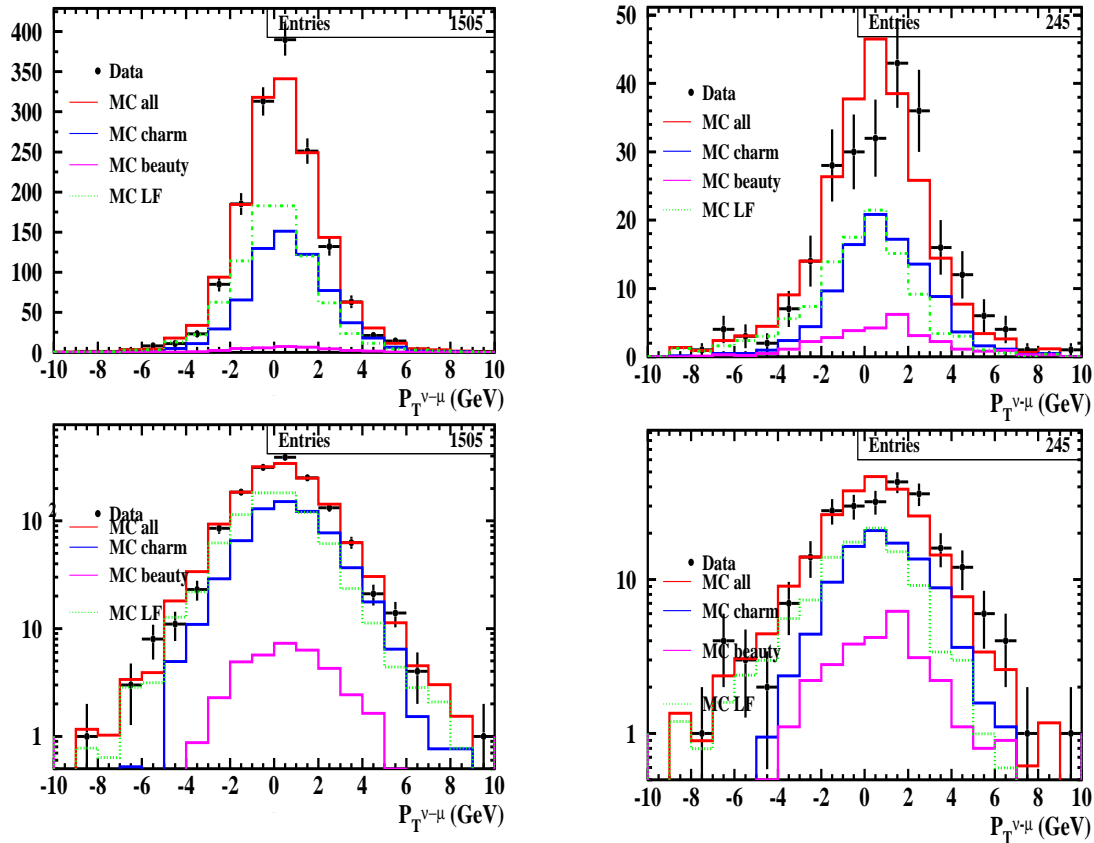


Figure 4.20: $P_T^{\nu\mu}$ distribution for Rear (left) and Forward (right) muon detectors. In all the plots the data (dots) are compared to the inclusive MC distribution (red line) obtained by summing the beauty (pink line), charm (blue line) and light flavour (green line) contributions according to the MC cross sections. The MC sum was normalized to the DATA. The Rapgap MC for charm and beauty, Ariadne MC for light flavours have been used.

Chapter 5

Extraction of charm and beauty fractions

In this Chapter the methods used to extract a charm and beauty fraction from the selected data sample are outlined. The P_T^{rel} , δ and $P_T^{\nu||\mu}$ fits are separately presented and their 2-D combined fits are then shown. Moreover, a 3-dimensional fit using at the same time all these variables is presented. The resulting fractions for different fitting techniques will be shown and, in case of 3-D fit, used to calculate the differential cross sections as described in Chapter 5.

5.1 1-dimensional fit

The first steps of the fraction determination are the 1-dimensional fits of the observables we have introduced in section 4.8. We'll explain the technique in P_T^{rel} fit section. For the other observables, the procedure is similar.

5.1.1 P_T^{rel} fit

The determination of the charm and beauty fractions in the data relies on the difference between the shapes of the P_T^{rel} distributions of the charm (c), beauty (b) and light quark (lf) components. The P_T^{rel} shape of the data results from the sum of various contributions, simulated by the different

Monte Carlo components. A fit on the P_T^{rel} variable can distinguish between these contributions. A fit to the data was then performed, using the following function:

$$N_i^{fit} = \frac{N^{data}}{N^c} \cdot f_c N_i^c + \frac{N^{data}}{N^b} \cdot f_b N_i^b + \frac{N^{data}}{N^{lf}} \cdot f_{lf} N_i^{lf} \quad (5.1)$$

where N_i^c , N_i^b , N_i^{lf} and N_i^{fit} are the contents of the i -th bin in the charm, beauty, light flavour and summed P_T^{rel} distributions. N^{data} , N^c , N^b , N^{lf} are the total number of events selected for Data and MC samples respectively, necessary for the normalization factors. The free parameters of the fit, f_c , f_b and f_{lf} , can be interpreted as the relative fractions of charm, beauty and light flavour events in the data, providing they sum up to 1. A χ^2 function

$$\chi^2 = \sum_i \frac{(N_i^{data} - N_i^{fit})^2}{\sigma_i^2} \quad (5.2)$$

was constructed and minimised, using FORTRAN program, based on minuit, to perform the fit. In eq. ?? N_i^{data} is the i -th bin content of the P_T^{rel} distribution of the data and σ_i^2 is the square of the error on the i -th bin content: $\sigma_i^2 = N_i^{data} + N_{data} \sum_{j=c,b,lf} f_j / (N^j)^2$. This χ^2 assumes that the distribution for N_i^{data} is Gaussian; it is of course Poisson, but the Gaussian is a good approximation to the Poisson for large numbers. The total number of events after the selection cuts is **11347**; we splitted this sample in three subsamples: REAR, BARREL and FORWARD, that correspond to **1505**, **9597** and **245** events respectively.

As first step we splitted the P_T^{rel} distribution in 13 equal bins, from 0 to 2.6 GeV. Then the histograms from MC were fitted to the data (see fig.??). The fractions extracted in the Barrel zone are:

$$f_c = 0,674 \pm 0,135 \quad (5.3)$$

$$f_b = 0,116 \pm 0,024 \quad (5.4)$$

and the fit gives a $\chi^2 = 14.56/10$. The charm and light flavour fractions are not meaningful since their errors are highly anticorrelated, the two samples

Entries

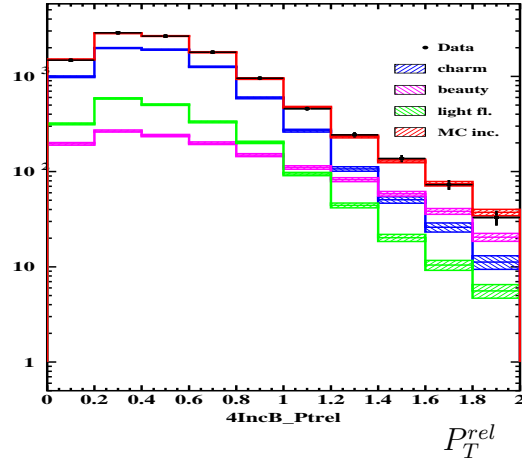


Figure 5.1: Fit of the P_T^{rel} distribution of the data (black dots) with the MC mixture (red line) of charm, beauty and light flavours. The different MC components are also shown independently. The blue line indicates the charm, the pink line is beauty, the green line is the light flavours and the red line is the sum of the MC contributions. The plot refers to Barrel.

having similar P_T^{rel} shapes. Regarding the beauty fraction, since his P_T^{rel} distribution is quite different from the rest, we have a reliable estimate.

Looking at the output of MINUIT program we notice the good precision of the beauty fraction, that is almost orthogonal (independent) to the charm fraction that unfortunately cannot be determinate very well because of the strong anticorrelation with light flavour fraction.

5.1.2 Impact Parameter fit

A similar fit was used to extract the charm and beauty fractions exploiting the different impact parameter shapes of the samples. For each muon candidate the impact parameter δ (see Chapter 3) was calculated using MVD improved tracks and beam spot information. This has been possible just in Barrel MVD acceptance region, where the cut on the quality of the tracks ($N_{(MVDhits)} \geq 4$) was meaningful. As already mentioned, in the forward zone

```

Y-AXIS: PARAMETER 2: f2
0.1490 44 333 * 22222 222
0.1459 4 33 222 22
0.1429 33 222 2
0.1398 33 22 * 2
0.1368 33 22 *
0.1338 33 22 * 1111 2
0.1307 33 22 111 11 2
0.1277 3 22 111 1 2
0.1247 22 11 * 1 22
0.1216 22 11 * 1 2
0.1186 22 11 00 11 22
0.1156 **2****1***000***1****2**
0.1125 22 11 00 11 22
0.1095 2 1 * 11 22
0.1065 22 1 * 11 22 3
0.1034 2 1 111 22 33
0.1004 2 11 111 22 33
0.9736E-01 2 1111 * 22 33
0.9432E-01 * 222 33
0.9129E-01 2 *22 33 4
0.8825E-01 2 222 33 44
0.8522E-01 22 222* 333 44
0.8218E-01 222222222 * 33 44
I I I
0.4348 0.8266
0.674

```

we don't use δ to extract the fraction because of the alignment problems. The sample decreased to **10042** events: **1325** in the Rear and **8539** in the Barrel.

The reference axis, which is needed to define the sign of δ , is taken to be the direction of the muon jet P_T vector provided by the jet algorithm. The distribution in the unphysical region of negative δ reflects the finite resolution of the impact parameter reconstruction. As shown in Figure ??, the data distribution (black dots) is not symmetric around $\delta = 0$ cm; the excess at positive values indicating a relevant contribution from long-lived particle decays.

To exploit this asymmetry to produce a quantitative measurement, we applied the fit procedure as described in section ?? for P_T^{rel} to the impact parameter distribution using as input the δ spectra obtained from MC and data samples. We divided the two subsample in 20 equal bins from -0.1 cm to 0.1 cm. The fractions extracted for the Barrel subsample are:

$$f_c = 0.379 \pm 0.103 \quad (5.5)$$

$$f_b = 0.155 \pm 0.044 \quad (5.6)$$

```

Y-AXIS: PARAMETER 2: f2
0.2262 22 2222 333 44 555
0.2198 2 22 *33 44 55
0.2133 222 * 33 44 55
0.2068 2 222 33 444 5
0.2004 2 22 33 44
0.1939 2 1111 *22 33 44
0.1875 22 1 111* 22 333 44
0.1810 22 1 11 22 33 4
0.1745 2 1 11 22 3
0.1681 22 11 *11 22 33
0.1616 3 22 11 00 11 22 33
0.1551 33**22**11*000*11**22**33
0.1487 33 22 11 00 11 22 3
0.1422 33 22 11* 11 22
0.1357 4 33 22 11 1 2
0.1293 44 33 22 11 1 22
0.1228 44 33 22 *1111 1 22
0.1164 44 33 22* 111 2
0.1099 5 44 33 222 2
0.1034 55 44 33 *22 2
0.9696E-01 55 44 333* 222 2
0.9050E-01 55 444 33 222 2
0.8404E-01 66 555 44 333 2222222
I I I
0.2319 0.3792 0.5688
X-AXIS: PARAMETER 1: f1

```

and the fit (see fig. ??) gives a $\chi^2 = 15.8/17$. At this stage, the impact parameter distribution alone can be used to extract a meaningful beauty+charm fraction, since the shapes of the heavy flavours Monte Carlo distribution are different from fake muons contribution but not sufficiently different between themselves. From MINUIT we see their (b and c) strong anticorrelation.

5.1.3 $P_T^{\nu\|\mu}$ fit

The last observable we used to get the fractions from data fit is $P_T^{\nu\|\mu}$. In this case, as for the P_T^{rel} , the fit has been achieved regardless of the quality of the tracks. We come back to the extended sample of **11347** events. We divided the subsamples in 20 equal bins, from -10 GeV to +10 GeV. The fractions obtained from the Barrel sample are:

$$f_c = 0.469 \pm 0.033 \quad (5.7)$$

$$f_b = 0.006 \pm 0.046 \quad (5.8)$$

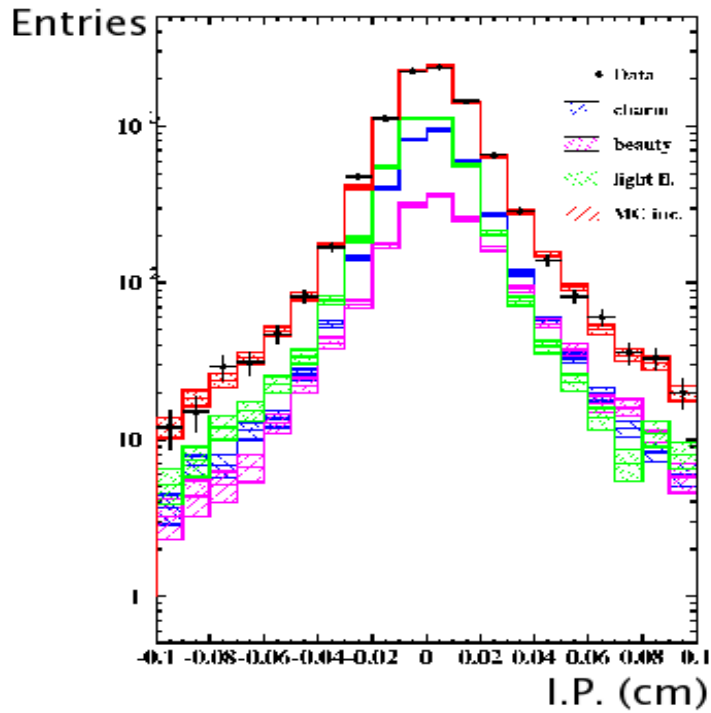


Figure 5.2: Fit of the δ distribution of the data (black dots) with the MC mixture (red line) of charm, beauty and light flavours. The different MC components are also shown independently. The blue line indicates the charm contribution, the pink line is beauty, the green line is the light flavours and the red line is the sum of the MC contributions. The plot refers to Barrel subsample.

giving a $\chi^2 = 12/17$. This fit allows us to separate the light flavour contamination from the rest. The beauty fraction here is compatible with zero and is strongly anticorrelated with charm fraction.

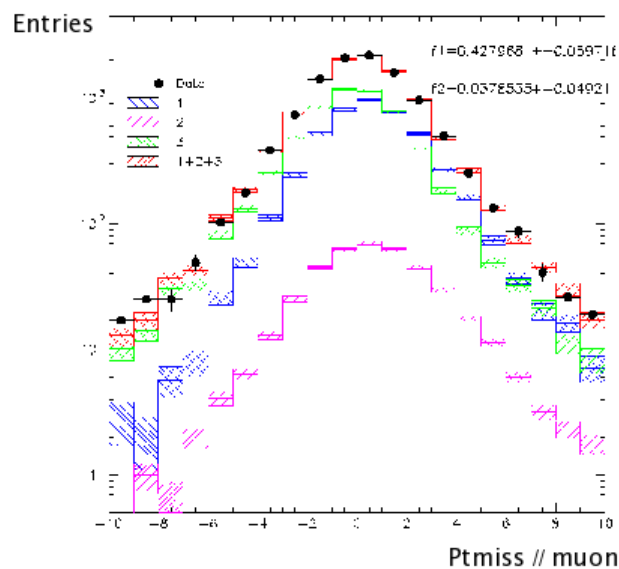


Figure 5.3: Fit of the $P_T^{\nu\mu}$ distribution of the data (black dots) with the MC mixture (red line) of charm, beauty and light flavours. The different MC components are also shown independently. The blue line indicates the charm contribution, the pink line is beauty, the green line is the light flavours and the red line is the sum of the MC contributions. The plot refers to Barrel subsample.

Chapter 6

Charm and beauty cross sections

In this chapter we define the differential cross sections we want to measure. We show the fractions and then the acceptances in different bins of several variables. Finally we'll give the measured cross sections and the comparisons with MC and theoretical predictions. In the the last section we will talk about the systematics studies.

6.1 Definition of cross section

The cross section definition (adopted from [88]) regards the process:

$$ep \rightarrow c(\bar{c})X \rightarrow \mu^\pm X \quad (6.1)$$

and has been calculated in the visible kinematic range

$$0.02 < y < 0.95, \quad \text{and} \quad Q^2 > 20 \text{ GeV}^2. \quad (6.2)$$

This is an "inclusive" cross section, i.e. one entry per muon that comes from a charm semileptonic decay and satisfies the muon requirements

$$p_T^\mu > 1.5 \text{ GeV} \quad \text{and} \quad -1.6 < \eta^\mu < 1.3 \text{ or } 1.48 < \eta^\mu < 2.3. \quad (6.3)$$

6.2 Measured cross section

The measured cross section has been calculated with the following formula:

$$\sigma(ep \rightarrow c(\bar{c})X \rightarrow \mu^\pm X) = \frac{N_\mu(\text{rec.}) \cdot f_c}{A_c \cdot L}. \quad (6.4)$$

Here, $N_\mu(\text{rec.})$ is the number of muon candidates selected from the ZEUS data for an integrated luminosity L . f_c is the fraction of muons estimated to be due to charm semileptonic decay. A_c is calculated with MC of signal and denotes the acceptance for the events with a muon from c sample in the visible kinematic range. For cross sections, differential in one variable, e.g. Q^2 , p_T^μ ,... the fit procedure has to be repeated separately for each histogram distribution containing only events of one bin of the designated variable. Obviously, all we have mentioned is also valid for beauty fractions and acceptances.

6.3 Fraction determination

For each bin of the variables of which we want measure the differential cross section, we determined the relative fractions of charm and beauty. In the previous chapter we have shown the structure of the histograms we were going to fit. In the table 6.1 are indicated the extremis of each bin for each variable.

We divided the Q^2 kinematic range in 5 bins from 20 GeV^2 to 10000 GeV^2 and X range in 5 bins from $3 \cdot 10^{-4}$ to 0.1. The muon variables have been divided in 4 and 6 bins of p_T^μ and η^μ respectively.

We were also interested to measure a double differential cross section, as a function of Y and Q^2 . For this reason, we considered 2 different Q^2 regions:

$$20 \text{ GeV}^2 < Q^2 < 90 \text{ GeV}^2 \quad \text{and} \quad 90 \text{ GeV}^2 < Q^2 < 10000 \text{ GeV}^2,$$

with 2 different binning for Y : in the first case, for lower Q^2 , we define $Y^{L.Q.}$ varying from 0.02 to 0.7; in the second case, for higher Q^2 , we define $Y^{H.Q.}$ varying from 0.02 to 0.95. To extract the fractions of signal in the bins we have mentioned, numerous fits have been made and in figure 6.1 we give an example of how much these histograms vary for the bins of p_T^μ .

$Q_{\Sigma}^2 (GeV^2)$	5 bins	20	40	80	200	500	10000	-
X_{Σ}	5 bins	0.0003	0.001	0.002	0.004	0.01	0.1	-
$y_{\Sigma}^{l,Q}$	4 bins	0.02	0.14	0.24	0.4	0.1	-	-
$y_{\Sigma}^{h,Q}$	3 bins	0.02	0.24	0.4	0.95	-	-	-
$p_T^{\mu} (GeV)$	4 bins	1.5	2.5	4.	6.	10.	-	-
η^{μ}	6 bins	-1.6	-0.9	-0.4	0.	0.5	1.4	2.3

Table 6.1: Table of the binning of the variables about which we calculated differential cross section. Here are reported the extremes of each bin.

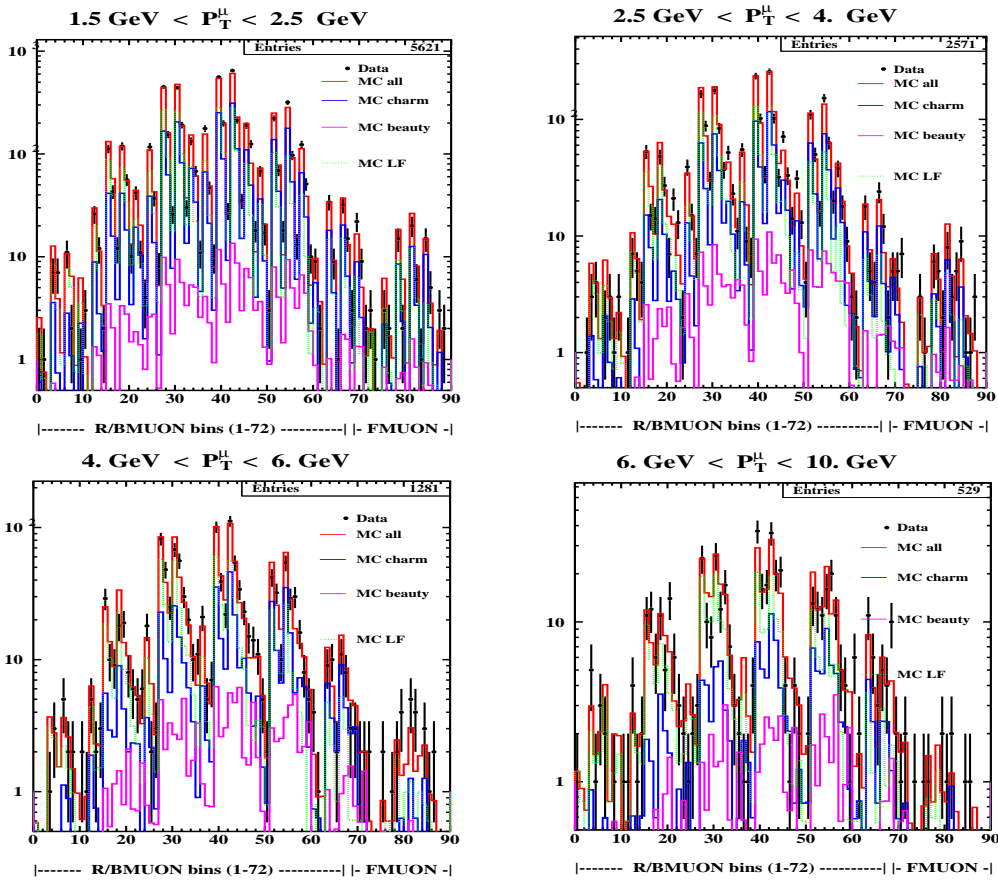


Figure 6.1: Histogram used to extract the fractions of signal in the data sample for different bins of p_T^{μ} . The different components are also shown. The blue line indicates the charm, the pink line is beauty, the green line is the light flavours and the red line is the sum of the contributions we fitted to the data.

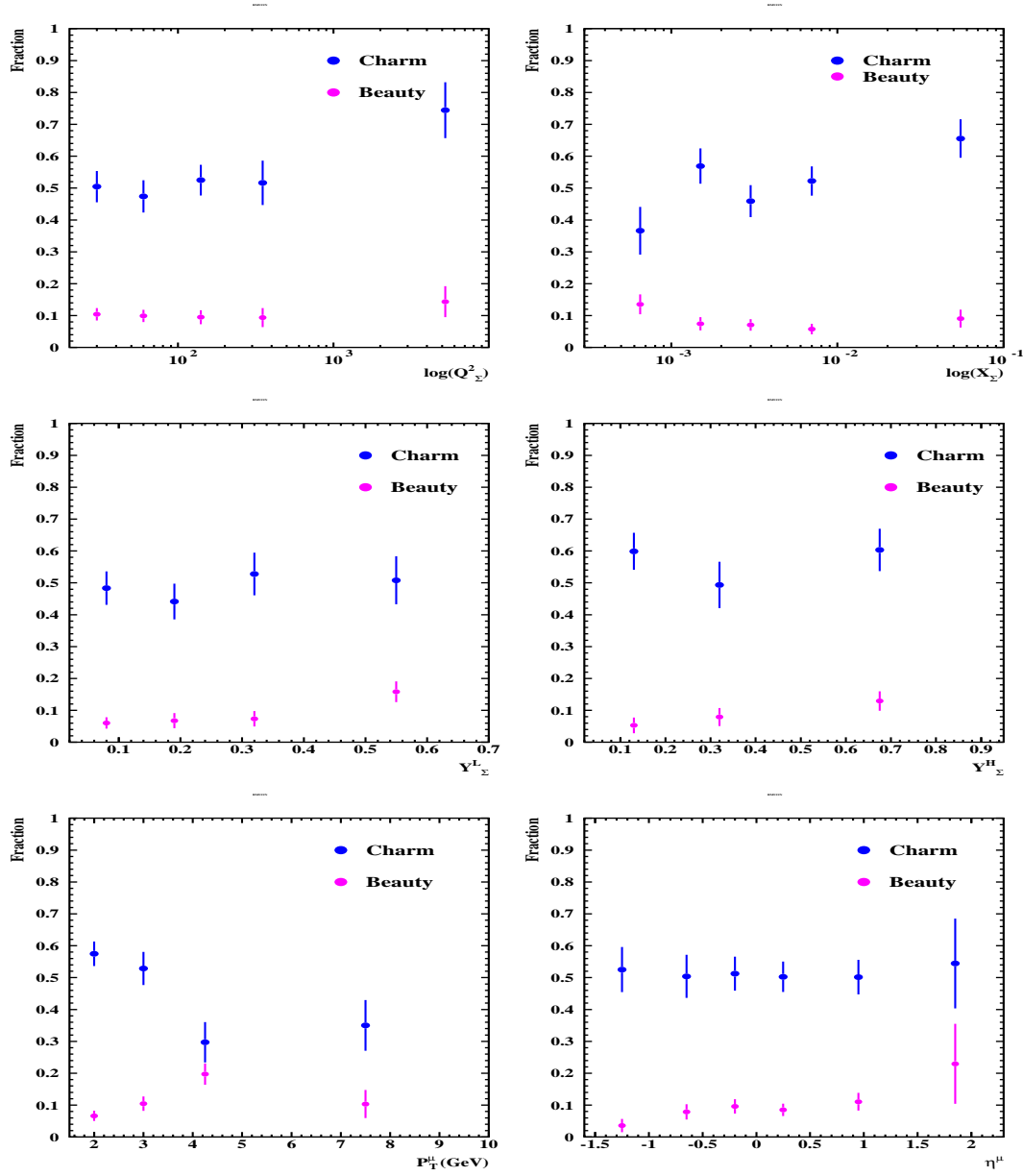


Figure 6.2: Fraction distributions for bins of Q^2 , x , $Y^{L,q}$, $Y^{H,q}$, p_T^μ , η^μ for charm (blue dots) and beauty (pink dots) signals.

In fig. 6.2 we show the obtained fractions. We have flat distributions in bins of Q^2 , X , $Y^{L,Q}$, $Y^{H,Q}$ and η^μ . About p_T^μ , we see that charm fraction decreases and beauty fraction increases for high p_T^μ values. The global fractions we obtained are $\sim 50\%$ for charm and $\sim 10\%$ for beauty.

6.4 Acceptances

The acceptance is defined as the fraction of muons generated in the visual kinematic region (see Eq. 6.2 and 6.3) that fulfill the selection:

$$A_c = \frac{N_c^\mu(rec.)}{N_c^\mu(gen.)}. \quad (6.5)$$

We used the charm and beauty MC samples from RAPGAP to calculate the acceptances. The numerator $N_c^\mu(rec.)$ is defined as the number of muons that satisfy the analysis (see Sec. 4.7) selection in the kinematic region given by the corresponding reconstructed variables.

We define the denominator $N_c^\mu(gen.)$ as the number of muons from charm semileptonic decay generated in the visible kinematic region (see Eq.6.2) that satisfy the cuts on muon characteristics (see Eq.6.3) at the generator level. In figure 6.3 we see the acceptances distribution on bins of Q^2 , X , $Y^{L.Q.}$, $Y^{H.Q.}$ and η^μ .

6.5 Fake muon contribution

Part of the muons considered in the numerator $N_c^\mu(rec.)$ of the acceptance formula (eq. 6.5), do not directly come from a semileptonic charm decay even if the event contain a charm quark. We call this kind of muons "fake" as the ones coming from light flavours. We saw from the MC that the fraction of this class of events is almost 30%. Anyway they will be included in the definition of cross section but the variation of this percentage will be treated as a further systematics check. From a comparison of the light flavour fraction and the results from the fit we found that the fake muon background is well reproduced.

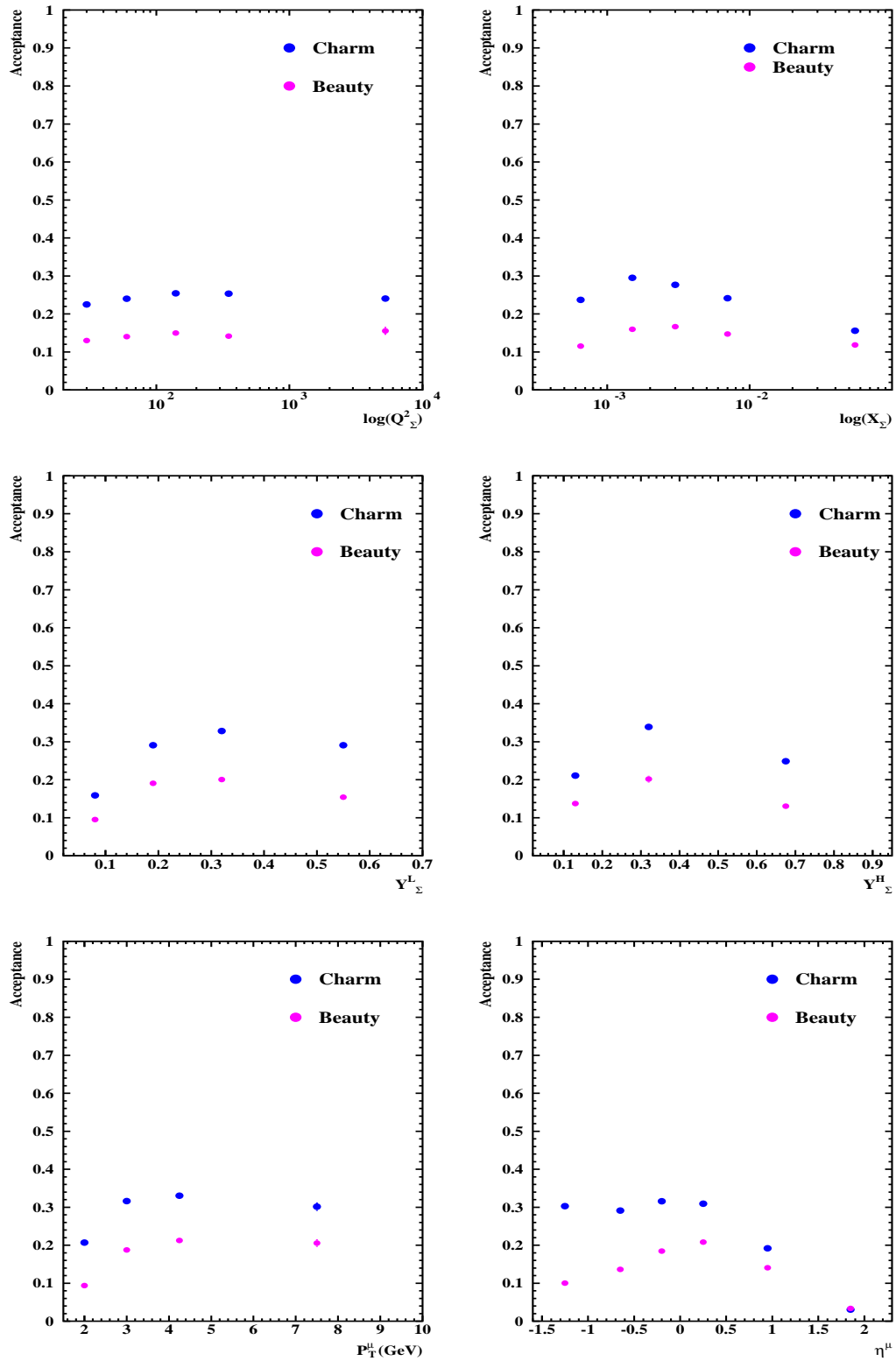


Figure 6.3: Acceptance distributions as a function of Q^2 , x , $Y^{L.Q.}$, $Y^{H.Q.}$, p_T^μ , η^μ for charm (blue dots) and beauty (pink dots) signals. The statistical error bars are not visible here because they are very small.

6.6 Cross section corrections

Several corrections need to be applied to the MC histograms at reconstructed-level, used to determine the fractions and the acceptances. Some factors modify the shape of the distributions used in the fits affecting the resulting fractions; other corrections give a factor that modify the acceptances. The reasons of these corrections are multiple and we'll give now a short description of each of this correction.

6.6.1 Muon efficiency corrections

All the MC reconstructed histograms have to be corrected for the muon chamber efficiencies. For the cross section measurements of this analysis, the muon detection efficiency is indeed essential and the efficiency in the MC has to be corrected to correspond to the efficiency in data.

To obtain the correction factors, a study [89] has been performed investigating the $J/\Psi \rightarrow \mu^+\mu^-$ decay and Bethe-Heitler (BH) processes. They are chosen as the source of muons due to their simple and easily selectable topology of two isolated muons. The correction is done giving a weight to the each muon in the MC. The weight is calculated as the ratio of data to MC efficiency:

$$w = \epsilon_{data}/\epsilon_{MC}. \quad (6.6)$$

For the rear-barrel detector, it depends on the muon transverse momentum p_T^μ and its pseudo-rapidity η_μ . For the forward muon [90], a constant factor has been obtained equal to **0.75** (see Fig.6.4). The error on these corrections is included in the systematical error (see Sec. 6.8).

6.6.2 Tracking efficiency corrections

Another important correction is needed because of the non-perfect simulation of the tracking system in the MVD. This factor has been evaluated by looking at the number of MVD hits before the cut in data and MC (see fig. 6.5). The global factor obtained is **0.96**.

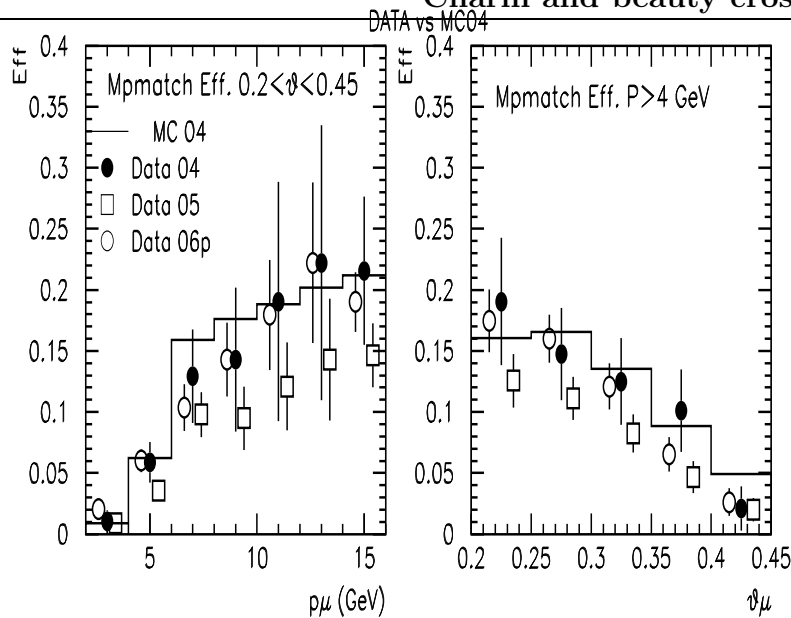


Figure 6.4: MPMATCH efficiency for different data samples, as a function of p_μ (left) and θ_μ (right). The 2004 MC (black line) is here compared with 2004 data (filled circles), 2005 data (empty squares) and 2006 data (empty circles).

6.6.3 P_T^{rel} corrections

We have already talked about the necessity to introduce this kind of correction (see section 4.8.1). We applied this kind of correction only to the light flavour background we have simulated. A detailed correction in each bin of P_T^{rel} for each bin of the cross section variables has been computed. For every muon a weight was applied in the light flavour MC distribution used in the fit. This kind of correction modifies the shape of the fitted distribution but does not affect the global acceptances. A systematic check of this correction will be presented.

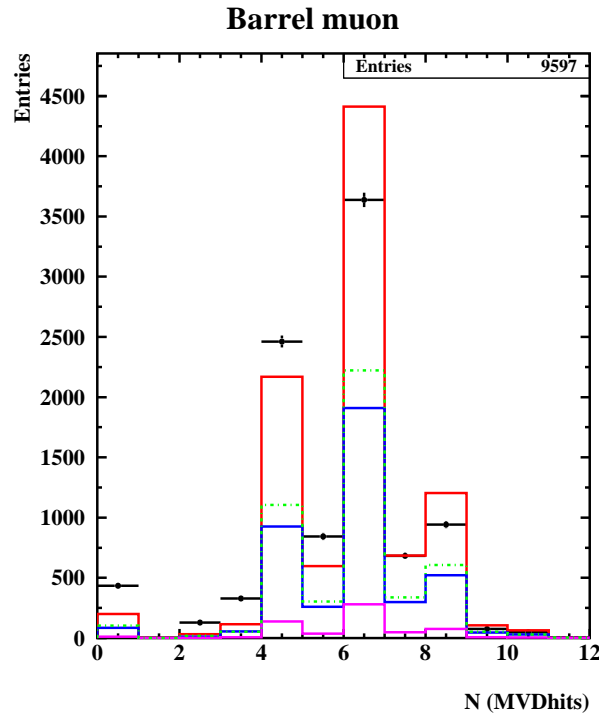


Figure 6.5: Control plot of the number of MVD hits before the cut on tracking quality ($N(MVDhits) \geq 4$) for the muon sample selected in the barrel region. The black dots represent the data sample, the red line histogram is the sum of the MC components: the blue one represents charm, the pink line is beauty and the green line is light flavour.

6.7 Charm and beauty differential cross sections

We present here the results for the 2005 data sample corresponding to a luminosity of 125.055 pb^{-1} . The differential cross sections for charm and beauty production are presented with the statistical error; in the same plots, cross sections from RAPGAP MC are also shown.

In figure 6.6 the differential cross sections as a function of Q^2 and x are presented and compared with RAPGAP MC. The MC describes the shape of the data for the charm contribution, except for the first bin in x , where the fit seems not able to distinguish between charm and beauty components. The

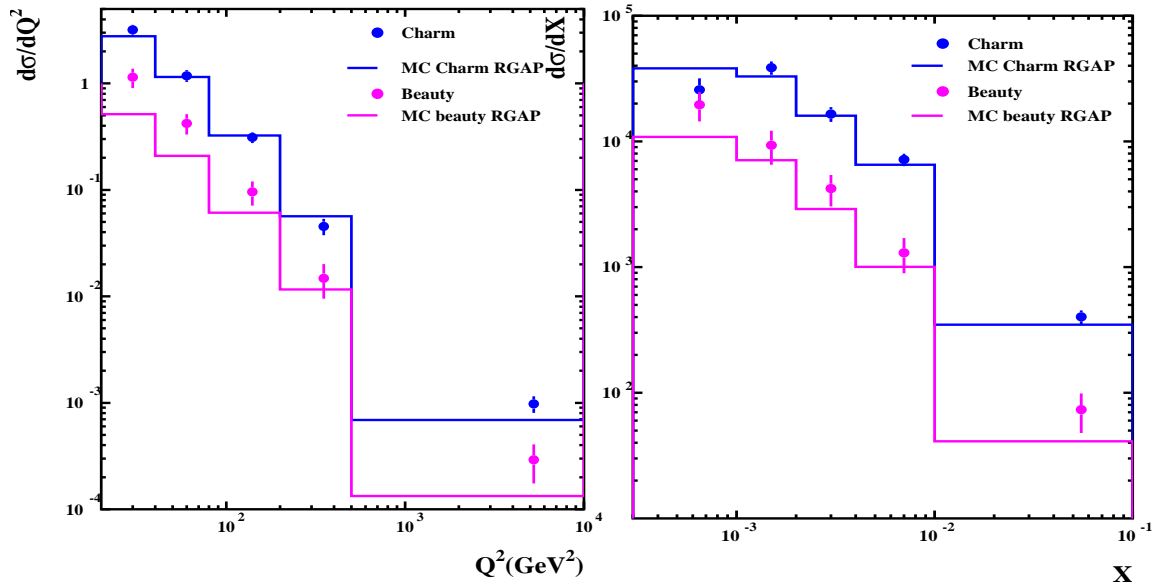


Figure 6.6: Differential cross sections $d\sigma/dQ^2$ and $d\sigma/dx$. The measurements are shown as blue dots for charm and pink dots for beauty. The error bars on the data points correspond to statistical uncertainties. The RAPGAP MC (blue and pink lines) is also shown.

MC is systematically below the data for beauty cross sections. This feature is known and has been already noticed by ZEUS [91]. In figure 6.7 we show Y differential cross sections for 2 different regions of Q^2 . Even in this case, we have good agreement between data and MC within error bars; for beauty we confirm what we have already said about previous cross sections.

In figure 6.8 we present the muon-cross sections as a function of p_T^μ and η^μ . Concerning charm cross sections, the RAPGAP MC describes the data very well except for the third bin of P_T^μ where the fit seems to be not very stable. The agreement in η^μ is acceptable. For the beauty cross sections the shapes are well reproduced but obviously the normalization is not correct; the data are a factor 2.5 higher than MC.

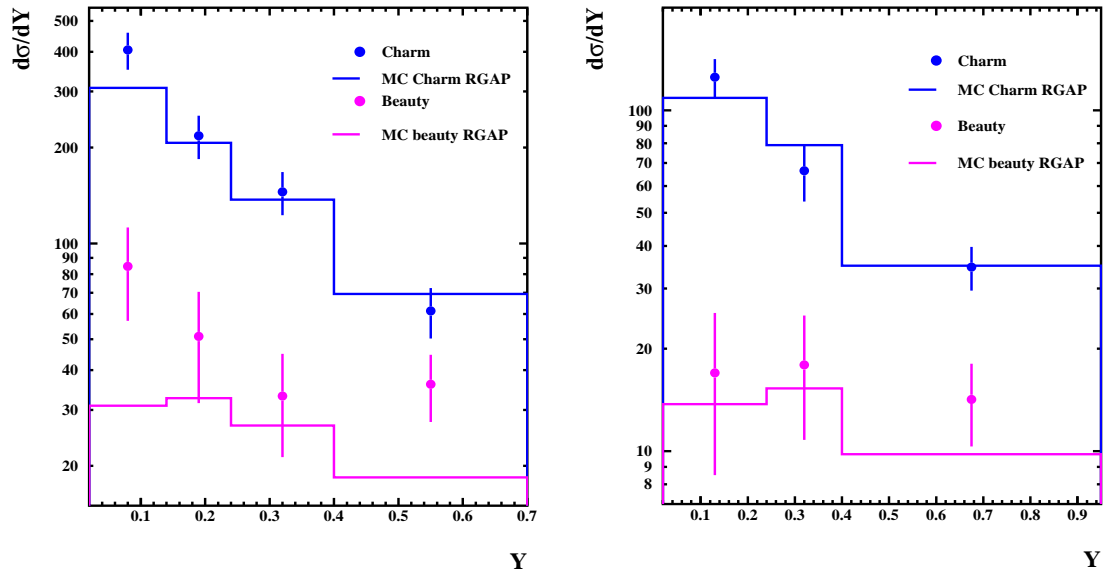


Figure 6.7: Differential cross sections $d\sigma/dY^{L.Q.}$ (left side) and $d\sigma/dY^{H.Q.}$ (right side). The measurements are shown as blue dots for charm and pink dots for beauty. The error bars on the data points correspond to statistical uncertainties. The RAPGAP MC (blue and pink lines) is also shown.

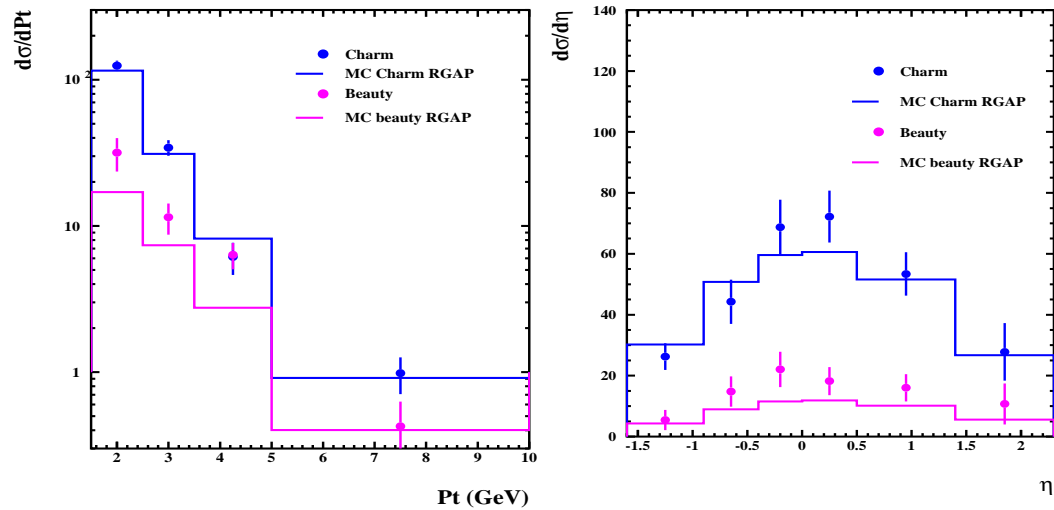


Figure 6.8: Differential cross sections $d\sigma/dp_T^\mu$ and $d\sigma/d\eta^\mu$. The measurements are shown as blue dots for charm and pink dots for beauty. The error bars on the data points correspond to statistical uncertainties. The RAPGAP MC (blue and pink lines) is also shown.

6.8 Systematic uncertainties

The systematic errors of the cross section measurements are determined by changing the selection cuts or the correction factors and repeating the extraction of the cross sections. For the differential distributions, the systematic uncertainties are calculated for each bin (see fig. 6.9) and are included in the following figures as the quadratic sum of statistical and systematic errors. Anyway, the statistical error turns out to be the largest uncertainty and varies from $\sim 10\%$ to $\sim 20\%$ in the bins with lower statistics.

The following systematic studies have been performed:

- **P_T^{rel} shape correction:** the correction for the difference in the shape of the light flavour MC samples and the data is applied for MC Ariadne sample (see Chapter 4). As a systematic check, the P_T^{rel} correction is applied to 100% and not at all. The effect on the cross-section is smaller than 5%.
- **Smearing function variation:** in chapter 4 the correction applied to the impact parameter shape of MC was described. The widths of the functions (Breit Wigner and Gaussian) used to fit the data distribution were varied by $\pm 20\%$ which translates into a variation of the total cross section of $\pm 3\%$.
- **Anti-isolation cut variation:** the cut $E_\mu^{iso} > 0.5$ GeV introduced in Chapter 4, has been varied from 0.25 GeV to 1 GeV. The differences of the cross sections are within $\pm 3\%$.
- **P_T^{jet} cut variation:** the cut $P_T^{jet} > 3$ GeV, introduced in chapter 4, has been varied from 2.5 GeV to 3.5 GeV. The differences of the cross sections are within $\pm 4\%$.
- **B/RMUON efficiency correction:** The resulting differences of the cross sections are within $\pm 5\%$. As expected, in the last bin of η^μ that represents the FORWARD muon, the cross section doesn't change varying these efficiencies.

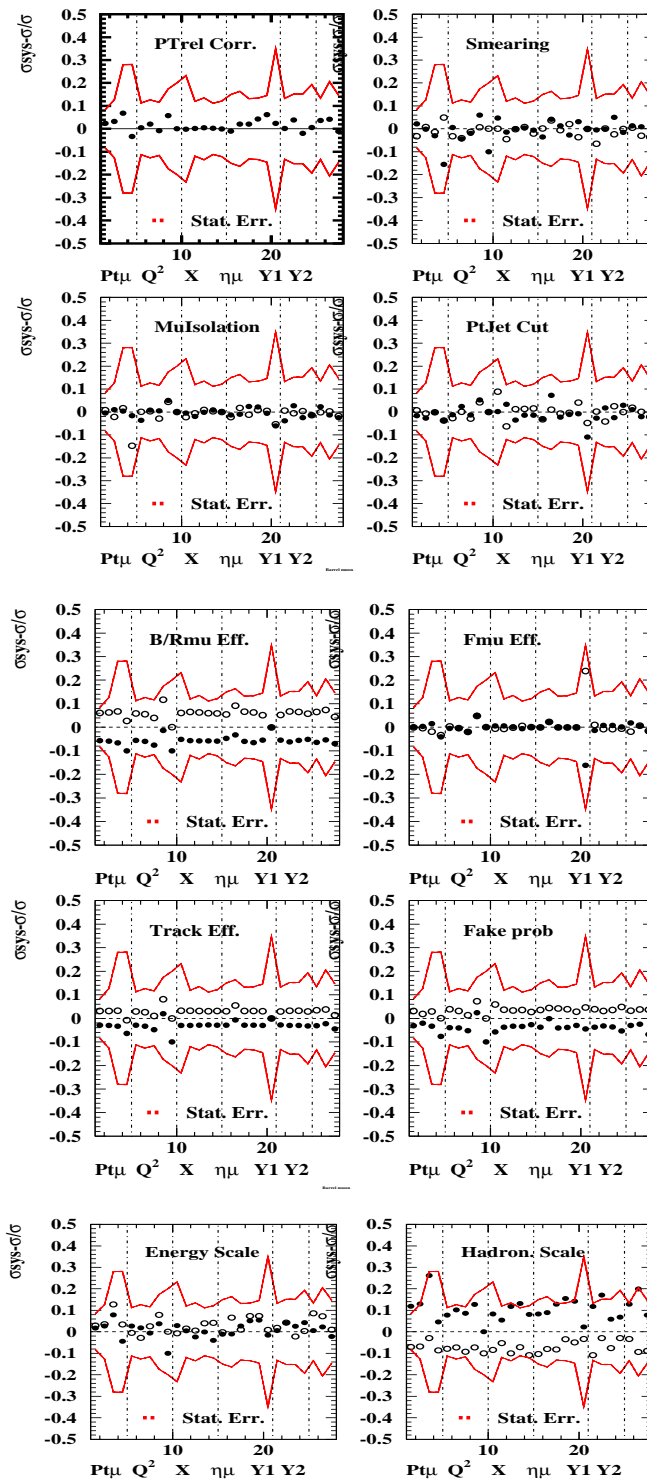


Figure 6.9: The relative systematic uncertainties are presented for each bin of the cross section variables. The filled circles represent the systematic uncertainties after a positive variation of the parameter; the empty circles come from a negative variation. The statistical uncertainties are also shown with the red line.

- **FMUON efficiency correction:** The resulting differences of the cross sections are within $\pm 2\%$. As expected, in the last bin of η^μ that represents the FORWARD muon, the cross section changes to $\pm 20\%$, that corresponds to the uncertainty of this correction.
- **Track efficiency correction:** the factor 0.96 that represents the tracking efficiency correction has been varied by $\pm 3\%$ and the effect on the cross sections is of the same order.
- **Fake muons contamination in the signal:** The uncertainties of the contribution from fake muons in c and b sample is estimated by changing the ratio of fake muons in the charm MC sample. The fake muons fraction in this sample has been estimated to be $\sim 30\%$; it is scaled by 1.2 and by 0.8. This leads to cross section differences of -4% and $+4\%$, respectively.
- **Energy scale uncertainty:** The energy of the jets, of the ZUFOs that represent the hadronic system and of the electron is scaled by $\pm 1\%$ in the MC. This systematic changes the shape of the $E - pz$ and of the P_T^ν . The differences of the cross sections are within $\pm 4\%$.
- **Hadronic scale uncertainty:** Only the energy of the ZUFOs is changed in this case. This affects the distribution of the P_T^ν and consequently the fractions obtained from the fits. This is the biggest systematic ($\pm 10\%$) of the measurement; it is anyway smaller than the statistical error.

The uncertainty of the luminosity measurement is 2.5% for the data period used. The luminosity error affects the overall normalization and is a correlated error in each data bin. This uncertainty is added in quadrature in the differential cross sections but is not shown in the distributions of the percentage systematic uncertainties.

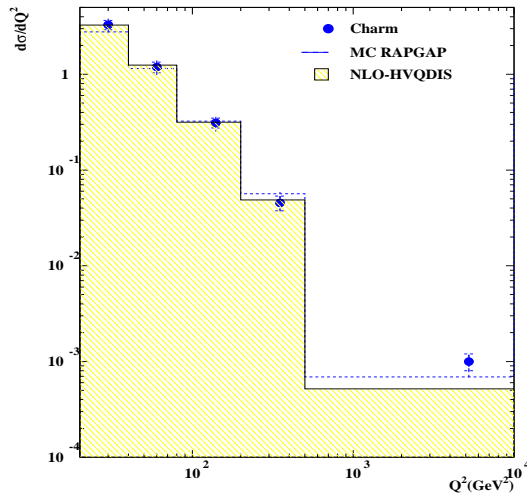


Figure 6.10: Differential cross sections $d\sigma/dQ^2$. The measurements are shown as blue dots for charm. The error bars on the data points correspond to the statistical uncertainty (inner error bars) and to the statistical and systematic uncertainties added in quadrature (outer error bars). The RAPGAP MC (blue dotted line) is also shown.

6.9 Discussion of results

In figures 6.10,6.11...6.13, we show the charm cross sections with the statistical and the systematic errors. These uncertainties are added in quadrature separately for the positive and negative variations to derive the total systematic error. The RAPGAP LO MC cross sections and the NLO QCD theoretical predictions from HVQDIS program (see Section 1.3.2) are also presented. In this case we show just the charm component because we don't have a NLO calculation for beauty cross section. Overall, for the charm contribution, we have a good agreement between our measurements, the RAPGAP LO MC and the NLO program HVQDIS predictions.

Concerning beauty component, the measured visible cross sections lie above the RAPGAP MC in every bin.

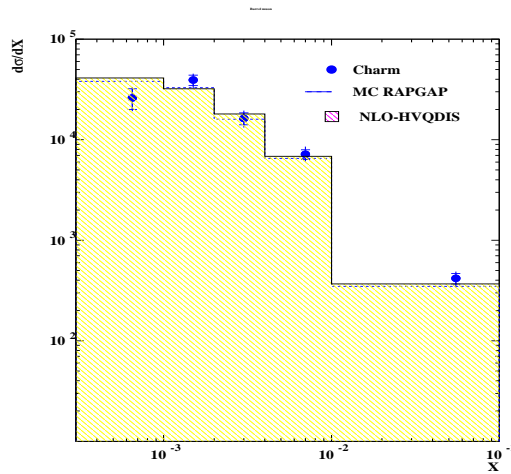


Figure 6.11: Differential cross sections $d\sigma/dx$. The measurements are shown as blue dots for charm. The error bars on the data points correspond to the statistical uncertainty (inner error bars) and to the statistical and systematic uncertainties added in quadrature (outer error bars). The RAPGAP MC (blue dotted line) is also shown.

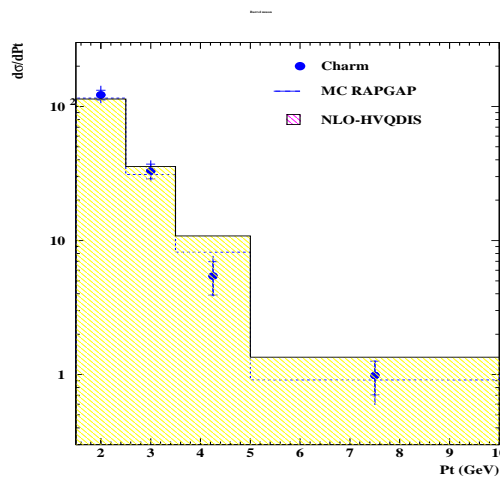


Figure 6.12: Differential cross sections $d\sigma/dY^{L.Q.}$ (left side) and $d\sigma/dY^{H.Q.}$ (right side). The measurements are shown as blue dots for charm. The error bars on the data points correspond to the statistical uncertainty (inner error bars) and to the statistical and systematic uncertainties added in quadrature (outer error bars). The RAPGAP MC (blue dotted line) is also shown.

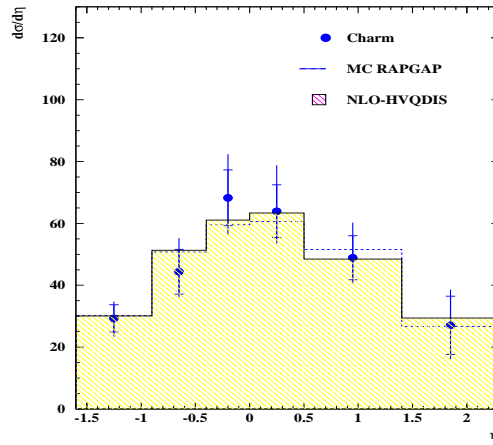


Figure 6.13: Differential cross sections $d\sigma/dY^{H.Q.}$ (right side). The measurements are shown as blue dots for charm. The error bars on the data points correspond to the statistical uncertainty (inner error bars) and to the statistical and systematic uncertainties added in quadrature (outer error bars). The RAPGAP MC (blue dotted line) is also shown.

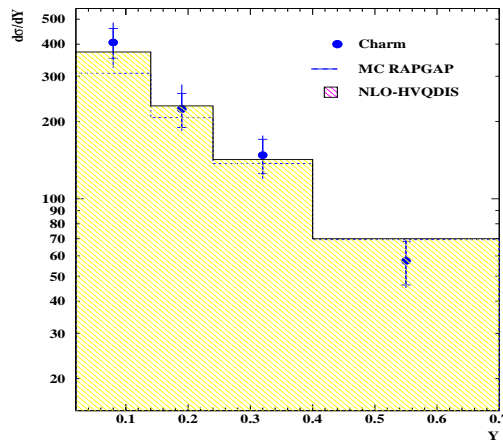


Figure 6.14: Differential cross sections $d\sigma/dp_T^\mu$. The measurements are shown as blue dots for charm. The error bars on the data points correspond to the statistical uncertainty (inner error bars) and to the statistical and systematic uncertainties added in quadrature (outer error bars). The RAPGAP MC (blue dotted line) is also shown.

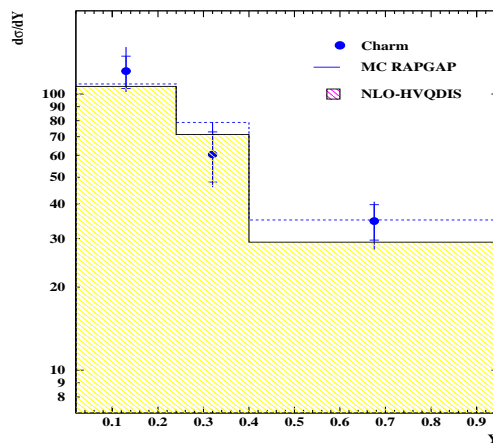


Figure 6.15: Differential cross sections $d\sigma/d\eta^\mu$. The measurements are shown as blue dots for charm. The error bars on the data points correspond to the statistical uncertainty (inner error bars) and to the statistical and systematic uncertainties added in quadrature (outer error bars). The RAPGAP MC (blue dotted line) is also shown.

Conclusions

The first measurement of c-quark production from semi-leptonic decays into muons for deep inelastic scattering at HERA has been presented. The corresponding reaction is

$$e p \rightarrow e c\bar{c}X$$

where at least one of the c-quarks decays semileptonically into a muon according to the following process:

$$c(\bar{c}) \rightarrow \mu^\pm \nu(\bar{\nu}) q \rightarrow \mu^\pm Jet. \quad (6.7)$$

The measurement is performed in a phase space region where the virtuality Q^2 of the photon exchanged is greater than 20 GeV^2 . The measurement is based on the data collected by ZEUS experiment during 2005, corresponding to an integrated luminosity of 125.055 pb^{-1} . Some discriminating variables have been used to distinguish the background due to the light flavours from the c and b quarks. Single differential cross sections for charm and beauty have been measured as a function of the main kinematic variables, of the transverse momentum and pseudorapidity of the muon.

The experimental cross sections for the charm contribution are in good agreement with the RAPGAP LO MC and the NLO program HVQDIS predictions. These results have a good precision and are comparable with the measurements from other charm analyses.

Concerning beauty component, the measured visible cross sections lie above the RAPGAP MC in every bin; this is the confirmation of what has been already seen from others ZEUS analysis.

Bibliography

- [1] M. Gell-Mann, *A schematic model of baryons and mesons.*, Phys. Lett. 8, 214 (1964)
- [2] R. P. Feynmann, *Very high-energy collisions of hadrons.*, Phys. Rev. Lett. 23, 1415 (1969)
- [3] J. D. Bjorken, *Asymptotic Sum Rules At Infinite Momentum*, Phys. Rev. 179, 1547 (1969)
- [4] G. Miller et al., *Inelastic Electron - Proton Scattering At Large Momentum Transfers*, Phys.Rev. D5, 528 (1972)
- [5] F. Halzen and A.Martin, *Quarks and Leptons: An Introduction Course in Modern Particle Physics* (John Wiley & Sons, 1984).
- [6] V.N. Gribov and L.N. Lipatov, *Yad. Fiz* 15, 1218 (1972).
- [7] G. Altarelli, G. Parisi, *Nucl. Phys.* B126,298 (1977).
- [8] Y.L.Dokshitzer, *Sov. Phys.,JEPT* 46,641 (1977).
- [9] L.M.Jones, H.W.Wyld, *A Measurement of Beauty Production in High-Energy Positron-Proton Scattering*, Phys. Rev. D17, 759 (1978)
- [10] E. Laenen, S.Riemersma, J.Smith,and W.L. van Naerven, *Nucl. Phys.*, B392,162 (1993)
- [11] E. Laenen, S. Riemersma, J. Smith,and W. L. van Naerven, *Nucl. Phys.*, B392,229 (1993)

- [12] B. W. Harris and J. Smith, Nucl. Phys. *B452*, 109 (1995), hep-ph/9503484
- [13] H. Jung, Comp. Phys. Commun. 86 147 (1995); H. Jung, *The RAPGAP Monte Carlo for Deep Inelastic Scattering, version 3.10*, Lund University, (2005) <http://www.quark.lu.se/hannes/rapgap/>
- [14] C. Peterson, D. Schlatter, I. Schmitt, P. M. Zerwas, *Scaling Violations Inclusive $E^+ E^-$ Annihilation Spectra*, Phys. Rev. D27, 105 (1983)
- [15] ZEUS Collaboration; S. Chekanov et al., Physical Review *D69* (2004)
- [16] ZEUS Collaboration; S. Chekanov et al.,
- [17] ZEUS Collaboration; S. Chekanov et al.,
- [18] ctau di alcune particelle
- [19] H1 Collab., A. Aktas et al., Eur. Phys. J. *C45* (2006) 23-33
- [20] H1 Collab., A. Aktas et al., Submitted to *23rd International Symposium on Lepton-Photon Interactions at High Energy, LP2007.*, H1prelim-07-171 (2007).
- [21] ZEUS Collab., *The ZEUS Detector, Status Report 1993*, U. Holm ed. (1993).
- [22] HERA - *A proposal for a large electron-proton colliding beam facility at DESY*, report DESY HERA 81/10, July 1981.
- [23] G. Ingelman, A. De Roeck, R. Klanner, *Proceeding of the Workshop Future Physics at HERA*, DESY (1995-1996).
- [24] U. Schneekloth, DESY-HERA-98-05.

- [25] D. Bailey et al., *Study of beam-induced backgrounds in the ZEUS detector from 2002 HERA running* (unpublished), 2002, available on <http://www-zeus.desy.de/kuze/zeusbg/> . ZEUS-Note 02-018. D. Bailey et al., *Study of beam-induced backgrounds in the ZEUS detector from 2002 HERA running (Addendum 1)* (unpublished), 2002, available on <http://www-zeus.desy.de/kuze/zeusbg/> . ZEUS-Note 02-020. D. Bailey et al., *Study of beam-induced backgrounds in the ZEUS detector from 2002 HERA running (Addendum 2)* (unpublished), 2003, available on <http://www-zeus.desy.de/kuze/zeusbg/> . ZEUS-Note 02-027.
- [26] DESY HERA 81-10 (81, REC. AUG.) 292p.
- [27] M. Seidel, DESY HERA-00-01.
- [28] B. Parker et al., *HERA Luminosity Upgrade Superconducting Magnet Production at BNL*, BNL-68284.
- [29] N. Harnew et al., Nucl. Instr. Meth. A279 290 (1989). B. Foster et al., Nucl. Phys. Proc. Suppl. B32 81 (1993). B. Foster et al., Nucl. Instr. Meth. A338 254 (1994).
- [30] E. Maddox, *Study of heavy quark production at HERA using the ZEUS microvertex detector*, PhD thesis (2004).
- [31] C. Coldewey, Nucl. Instr. and Meth. A447 44 (2000).
- [32] M. Derrick et al., Nucl. Instr. Meth. A309 77 (1991); A. Andersen et al., Nucl. Instr. Meth. A309 101 (1991); A. Caldwell et al., Nucl. Instr. Meth. A321 356 (1992);
- [33] A. Berstein et al., Nucl. Instr. Meth. A336 23 (1993).
- [34] A. Barbenger et al., Nucl. Instr. Meth. A382 419 (1996).
- [35] G. Battistoni et al., Nucl. Instr. Meth. 176 297 (1980).

- [36] A. Margotti, Diploma thesis, University of Bologna, (1990).
- [37] G. Abbiendi et al., Nucl. Instr. Meth. *A333* 342 (1993).
- [38] A. Garfagnini, *The ZEUS Micro Vertex Detector*, Nucl. Instr. and Meth. *A435* 34 (1999).
- [39] T. Jezynski et al., Proc. SPIE 5484 180 (2004). K. T. Pozniak et al., Proc. SPIE 5484 186 (2004).
- [40] H. Bethe and W. Heitler, Proc. Roy. Soc. Lond. *A146* 83 (1934).
- [41] S.M. Fisher, P. Palazzi, *ADAMO Reference Manual for Version 3.3. CERN ECP*, available on: [http :
://adamo.web.cern.ch/Adamo/refmanual/Document.html](http://adamo.web.cern.ch/Adamo/refmanual/Document.html).
- [42] M. Klein, in *Physics at HERA*, edited by W. Buchmüller and G. Ingelman Vol.1, p.71,Hamburg, 1991, DESY.
- [43] F. Jacquet, A. Blondel, *Proceedings of the Study of an ep facility for Europe*, Ed. U. Amaldi, DESY 79/48, 391.
- [44] S. Bentvelsen et al. *Reconstruction of (x, Q^2) and extraction of structure functions in neutral current scattering at HERA*, edited by W. Buchmüller and G. Ingelman Vol.1,p.23,Hamburg,1991,DESY.
- [45] U. Bassler and G. Bernardi, Nucl.Instrum.Meth. *A426*, 583(1999),hep-ex/9801017.
- [46] U. Bassler and G. Bernardi, Nucl.Instrum.Meth. *A361*, 197(1995),hep-ex/9412004.
- [47] G. Hartner, *VCTRAK: Online Output Information*, ZEUS-Note 97-064.
- [48] G. Hartner, *VCTRAK: ZEUS Track & Vertex Reconstruction*, 15.07.200.
- [49] G. Hartner, *VCTRAK Briefng: Program & Math*, ZEUS-Note 98-058.

- [50] H. Abramovicz, A. Caldwell, and R. Sinkus, Nucl.Instrum.Meth. A365, 508(1995), hep-ex/9505004.
- [51] R. Sinkus and T. Voss, Nucl.Instrum.Meth. A391, 360(1997).
- [52] A. Lopez-Duran Viani and S. Schlensted, Electron finder efficiencies and impurities, a comparison between SINISTRA95, EM and EMNET, ZEUS-NOTE 99-077
- [53] A. Kappes, *Verwendung von Neuronalen Netzen zur Identifikation des gestreuten Elektrons in ep-Ereignissen mit hohem Q^2 bei ZEUS.*, Diploma Thesis, Universitat Bonn, Germany, Report BONN-IB-97-28, 1997
- [54] T. Doeker, A. Frey, and M. Nakao, Electron position reconstruction. Update of the ELECPO routines, ZEUS-NOTE 94-123
- [55] J. Ng and W. Verkerke, An overview of SRTD analysis, ZEUS-Note 95-037
- [56] N. Tuning, ZUFOS: Hadronic final state reconstruction with calorimeter, tracking and backplash correction, ZEUS-Note 01-021
- [57] G. M. Briskin, *Diffraction dissociation in ep Deep Inelastic Scattering*, PhD Thesis, Tel Aviv University, School of Physics and Astronomy, 1998 DESY-THESIS 1998-036
- [58] G. Hartner et al., VCTRACK(3.06/20): Offline output information, ZEUS-Note 96-013
- [59] A. Longhin, Misura delle sezioni d'urto di fotoproduzione di Open Beauty ad HERA. (In Italian), Master Thesis, University of Padua, 2000.
- [60] S. Catani, Dokshitzer, L. Yuri, B.R. Webber, *The K-perpendicular clustering algorithm for jets in deep inelastic scattering and hadron collisions*, Phys.Lett. B285, 291-299 (1992);

- [61] S.Catani, Dokshitzer, L.Yuri, B.R.Webber, *Longitudinally invariant $K(t)$ clustering algorithms for hadron hadron collisions*, Nucl. Phys. B406 187-224 (1993)
- [62] S. D. Ellis and D. E. Soper, Phys. Rev. D48, 3160 (1993) [arXiv:hep-ph/9305266].
- [63] G.Abbiendi, *Global tracking of muons in the Barrel and Rear region*, ZEUSNote, 99-063 (1999)
- [64] R.Brun, et al., CERN-DD/EE/84-1 (1984)
- [65] V.Giannotti, University of Roma, thesis, unpublished (1999)
- [66] L.Bellagamba, MVMATCH: A package to match FMUON tracks with Central Detectors, ZEUS-Note 96-051 (1996)
- [67] V.Innocente, M.Maire and E.Nagy, *GEANE: average tracking and error propagation package*, proceeding of MC91: Detector and Event Simulation in High Energy Physics, Amsterdam,1991.
- [68] R.Brun, et al., CERN-DD/EE/84-1 (1984)
- [69] Kalman, Rudolph, Emil, Transactions of the ASME-Journal of Basic Engineering D82, 35 (1960)
- [70] A.Bertolin, R.Brugnera, M.Turcato, Study of the GLOMU and BREMAT muon-finders efficiencies, ZEUS-NOTE 05-022 (2005)
- [71] A.Bertolin, R.Brugnera, M.Turcato private communication. For a list,see: <http://www-zeus.desy.de/mturcato/ZEUSONLY/BMUON/mbtake.fpp> <http://www-zeus.desy.de/mturcato/ZEUSONLY/BMUON/mbtake9800.fpp>
- [72] M.Corradi, Efficiency corrections for the muon finders BREMAT and MPMATCH2, ZEUS-NOTE 04-006 (2004)

- [73] A. Longhin, Fake muon probabilities studies ZEUS NOTE 05-001 (2005)
- [74] H. Jung and G.P.Salam, *Eur. Phys. J. C* *19* (2001).
- [75] ZEUS Collaboration; S. Chekanov et al. *Eur. Phys. J. C* *44*, 13-25 (2005)
- [76] G.A.Schuler, H.Spiesberger, *Physics at HERA proceedings* *3*, 1419 (1991)
- [77] A.Kwiatkowski, H.Spiesberger, H.-J.Möhring, HERACLES 4.1 - An event generator for ep interactions at HERA including radiative processes, *Proc. of the Workshop on Physics at HERA, Vol. 3*, edited by W.Buchmüller, G.Ingelman (1991), p. 1294.
- [78] A.Kwiatkowski, H.Spiesberger, H.-J.Möhring, HERACLES - An event generator for ep interactions at HERA including radiative processes. version 4.6, (1996), <http://www.desy.de/hspiesb/heracles.html>
- [79] L.Lönnblad, ARIADNE version 4: A Program for simulation of QCD cascades implementing the color dipole model, *Comp. Phys. Commun.* *71*, 15 (1992)
- [80] S.Kuhlmann, *CTEQ5 parton distributions and ongoing studies*, *Nucl. Phys. Proc. Suppl.* *79* 108 (1999)
- [81] G.Altarelli, G.Parisi, Asymptotic Freedom In Parton Language, *Nucl. Phys. B* *126*, 298 (1977)
- [82] Y.Dokshitzer, Calculation Of The Structure Functions For Deep Inelastic Scattering And E+ E- Annihilation By Perturbation Theory In Quantum Chromodynamics. (In Russian), *Sov. Phys. JETP* *46*, 641 (1977)
- [83] V.Gribov, L.Lipatov, Deep Inelastic E P Scattering In Perturbation Theory, *Sov. J. Nucl. Phys.* *15*, 438 and 675 (1972)

-
- [84] L.Lipatov, The Parton Model And Perturbation Theory, Sov. J. Nucl. Phys. *20*, 94 (1975)
- [85] T.Sjostrand et al., High-energy-physics event generation with PYTHIA 6.1, Comput. Phys. Commun. *135*, 238 (2001)
- [86] ZEUS Coll., *First results on beauty production using HERA II data*, proceeding of: International Conference on High Energy Physics, Beijing, 2004.
- [87] F. James, *MINUIT - Minimization Package Reference Manual - v94.1*.
- [88] ZEUS Coll., S. Chekanov et al., Phys. Rev. D *70* 012008 (2004).
- [89] A. Bertolin, R. Brugnera, M. Turcato, Study of the GLOMU and BREMAT Muon-Finders Efficiencies ZEUS NOTE 05-022 (2005)
- [90] M. Corradi, Efficiency corrections for the muon finders BREMAT and MPMATCH2, ZEUS NOTE 04-006 (2004)
- [91] ZEUS Coll., S. Chekanov et al., Physics Letters B *599* (2004) 173-189